Nano-Optics and Nanophotonics

Motoichi Ohtsu
Takashi Yatsui *Editors*

Progress in Nanophotonics 4

Springer

Nano-Optics and Nanophotonics

The Springer Series in Nano-Optics and Nanophotonics provides an expanding selection of research monographs in the area of nano-optics and nanophotonics, science- and technology-based on optical interactions of matter in the nanoscale and related topics of contemporary interest. With this broad coverage of topics, the series is of use to all research scientists, engineers and graduate students who need up-to-date reference books. The editors encourage prospective authors to correspond with them in advance of submitting a manuscript. Submission of manuscripts should be made to the editor-in-chief, one of the editors or to Springer.

More information about this series at http://www.springer.com/series/8765

Motoichi Ohtsu · Takashi Yatsui
Editors

Progress in Nanophotonics 4

Springer

Editors
Motoichi Ohtsu
School of Engineering
The University of Tokyo
Tokyo
Japan

Takashi Yatsui
School of Engineering
The University of Tokyo
Bunkyo-ku, Tokyo
Japan

ISSN 2192-1970 ISSN 2192-1989 (electronic)
Nano-Optics and Nanophotonics
ISBN 978-3-319-49012-0 ISBN 978-3-319-49013-7 (eBook)
DOI 10.1007/978-3-319-49013-7

Library of Congress Control Number: 2016959177

Printed on acid-free paper

This Springer imprint is published by Springer Nature
The registered company is Springer International Publishing AG
The registered company address is: Gewerbestrasse 11, 6330 Cham, Switzerland

Preface to *Progress in Nanophotonics*

As the first example, recent advances in photonic systems demand drastic increases in the degree of integration of photonic devices for large-capacity, ultra-high-speed signal transmission and information processing. Device size has to be scaled down to nanometric dimensions to meet this requirement, which will become even more strict in the future. As the second example, photonic fabrication systems demand drastic decreases in the size of the fabricated patterns for assembling ultra-large-scale integrated circuits. These requirements cannot be met even if the sizes of the materials are decreased by advanced methods based on nanotechnology. It is essential to decrease the size of the electromagnetic field used as a carrier for signal transmission, processing, and fabrication. Such a decrease in the size of the electromagnetic field beyond the diffraction limit of the propagating field can be realized in optical near-fields. Nanophotonics, a novel optical technology that utilizes the optical near-field, was proposed by M. Ohtsu (the editor of this monograph series) in 1993 in order to meet these requirements. However, it should be noted that the true nature of nanophotonics involves not only its ability to meet the above requirements but also its ability to realize qualitative innovations in photonic devices, fabrication techniques, energy conversion, and information processing systems by utilizing novel functions and phenomena made possible by optical near-field interactions, which are otherwise impossible as long as conventional propagating light is used. Based on interdisciplinary studies on condensed matter physics, optical science, and quantum field theory, nanomaterials and optical energy transfer in the nanometric regime have been extensively studied in the last two decades. Through these studies, novel theories on optical near-fields have been developed, and a variety of novel phenomena have been found. The results of this basic research have been applied to develop nanometer-sized photonic devices, nanometer-resolution fabrication, highly efficient energy conversion, and novel information processing, resulting in qualitative innovations. Further advancement in these areas is expected to establish novel optical sciences in the nanometric space, which can be applied to further progress in nanophotonics in order to support the sustainable development of peoples living all over the world. This unique monograph series entitled “Progress in Nanophotonics in the Springer Series in

Nano-optics and Nanophotonics" is being introduced to review the results of advanced studies in the field of nanophotonics and covers the most recent topics of theoretical and experimental interest in relevant fields, such as classical and quantum optical sciences, nanometer-sized condensed matter physics, devices, fabrication techniques, energy conversion, information processing, architectures, and algorithms. Each chapter is written by leading scientists in the relevant field. Thus, this monograph series will provide high-quality scientific and technical information to scientists, engineers, and students who are and will be engaged in nanophotonics research. As compared with the previous monograph series entitled "Progress in Nano-Electro-Optics" (edited by M. Ohtsu, published in the Springer Series in Optical Science), this monograph series deals not only with optical science on the nanometer scale, but also with its applications to technology. I am grateful to Dr. C. Ascheron of Springer-Verlag for his guidance and suggestions throughout the preparation of this monograph series.

Tokyo, Japan Motoichi Ohtsu

Preface to Volume IV

This volume contains five review articles focusing on various but mutually related topics in nanophotonics written by the world's leading scientists.

The first article describes dressed photon technology. After a discussion of the concept of dressed photon based on the off-shell photon pictures, some applications are reviewed. Novel mathematical scientific models are also presented, as well as an outlook for the future.

The second article is devoted to describing nonequilibrium statistical mechanical models for photon breeding processes assisted by dressed-photon–phonons. Numerical results on the model systems qualitatively explain many basic properties of photon breeding.

The third article describes the near-field-assisted chemical reactions. The selective light-matter interaction has been achieved at the nano-scale. Using such a novel interaction, many applications are reviewed including the energy up-conversion for an artificial photosynthesis and smoothing the material surface.

The fourth article is devoted to review self-assembly for implementation of nanophotonic devices and systems. This article focuses on nanophotonic droplets and nanophotonics-based spatial light modulators as typical outcomes of the nanophotonics-based self-assembly.

The last article describes fabrication methods and performance characteristics of ultrathin, ultraflexible organic light-emitting diodes, organic solar cells, and organic transistors.

I hope that this volume will be a valuable resource forreaders and future specialists in nanophotonics.

The works reviewed in this book were partially supported by the JSPS Core-to-Core Program (A. Advanced Research Networks).

Tokyo, Japan

Motoichi Ohtsu
Takashi Yatsui

Contents

Contributors

Makoto Katori Faculty of Science and Engineering, Department of Physics, Chuo University, Tokyo, Japan

Hirotsugu Kobayashi Faculty of Business Administration, Department of IT Solutions, Business Breakthrough University, Tokyo, Japan

Katsuyuki Nobusada Department of Theoretical and Computational Molecular Science, Institute for Molecular Science, Okazaki, Aichi, Japan

Motoichi Ohtsu Institute of Engineering Innovation, School of Engineering, The University of Tokyo, Tokyo, Japan; Research Origin for Dressed Photon c/o Yokohama Technology Center, NICHIA Corporation, Kanagawa-ku, Yokohama, Kanagawa, Japan

Tsuyoshi Sekitani The Institute of Scientific and Industrial Research, Osaka University, Ibaraki, Osaka, Japan

Naoya Tate Faculty of Information Science and Electrical Engineering, Kyushu University, Nishi-ku, Fukuoka, Japan

Takashi Yatsui School of Engineering, University of Tokyo, Tokyo, Japan

Chapter 1
Progress in Dressed Photon Technology and the Future

Motoichi Ohtsu

Abstract This article reviews recent progress in dressed photon technology. After a discussion of the concepts of dressed photons based on the off-shell photon picture, some applications are reviewed, including novel optical functional devices, nanofabrication technologies, energy conversion technologies, and information processing systems. Novel mathematical scientific models are also presented, as well as an outlook for the future, hinting at the possibilities of dressed photon technology.

1.1 Introduction

First, as an introductory topic, the concept of elementary excitations is reviewed. Elementary excitations have been discussed for a long time in the field of solid state physics [1]. Excited states of a many-body system are regarded as a collection of certain fundamental excited states that has been called an elementary excitation, and also a quasi-particle. A phonon is a well-known example of a quasi-particle that represents the normal mode of crystal vibration in a solid. Another example is a plasmon, which corresponds to the collective motion of electron density variations in an interacting electron gas. An exciton, another well-known example, represents a quasi-particle related to an electron–hole pair in a solid. The interaction between a photon and an exciton forms a new steady-state that also represents a quasi-particle called an exciton–polariton. Its dispersion relation, which is the relation between the wave-number k and energy E of the exciton–polaritons in macroscopic space, is represented by curves A and B in Fig. 1.1. It should be noted that the quasi-particles described above also follow dispersion relations that are similar to these curves.

M. Ohtsu (✉)
Institute of Engineering Innovation, School of Engineering,
The University of Tokyo, 2-11-16 @Yayoi, Bunkyo-ku, Tokyo 113-8656, Japan
e-mail: ohtsu@nanophotonics.t.u-tokyo.ac.jp

M. Ohtsu
Research Origin for Dressed Photon c/o Yokohama Technology Center,
NICHIA Corporation, 3-13-19 Moriya-cho,
Kanagawa-ku, Yokohama, Kanagawa 221-0022, Japan

M. Ohtsu and T. Yatsui (eds.), *Progress in Nanophotonics 4*,
Nano-Optics and Nanophotonics, DOI 10.1007/978-3-319-49013-7_1

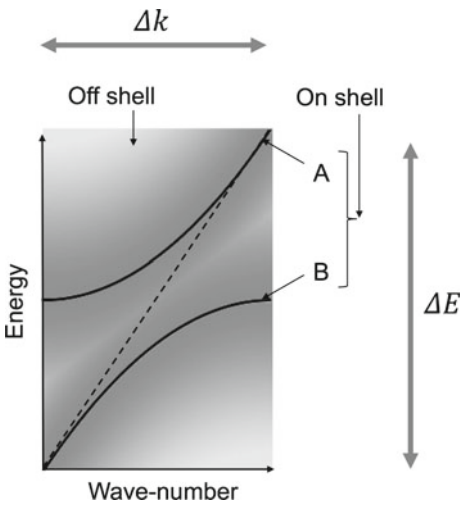

Fig. 1.1 Dispersion relation between the wave-number k and the energy E. The *curves* A and B represent the dispersion relation of the exciton–polariton. The broken line is that for light in free space. The *gray* shaded rectangle represents that for the dressed photon

Second, in preparation for starting the main topic of this section, it should be pointed out that there is a vast space around the curves A and B in this figure, which is represented by the gray shaded rectangle. A quasi-particle is also created in this space. By referring to the large size of this space, unique features of this quasi-particle are as follows:

(1) As represented by the horizontal double-pointed gray arrow, the wave-number, k, of this quasi-particle spans a wide range. This also means that its uncertainty, Δk, is large, which represents the non-conservation of the quasi-particle's momentum, $\hbar k$ (where $\hbar = h/2\pi$, and h is Planck's constant). This large uncertainty, Δk, also means that the quasi-particle is composed of a large number of normal modes. Furthermore, it means that the uncertainty, Δx, of the quasi-particle's position, x, is small, due to Heisenberg's uncertainty relation, $\Delta(\hbar k) \cdot \Delta x \geq \hbar$. This small uncertainty, Δx, means that the size of this quasi-particle is small.
(2) As is represented by the vertical double-pointed gray arrow, the energy E of this quasi-particle spans a wide range. This means that its uncertainty, ΔE, is large, which represents the non-conservation of the energy. The large uncertainty, ΔE, also means that the time uncertainty, Δt, is small, due to Heisenberg's uncertainty relation $\Delta E \cdot \Delta t \geq \hbar$. This means that this quasi-particle is created and subsequently annihilated within a short duration. In other words, the energy of this quasi-particle is temporally modulated, generating a large number of spectral sidebands.

The first feature, that is, the small size, means that the quasi-particle is created in a nanomaterial, and a part of the field of this quasi-particle penetrates through the surface of the nanomaterial to the outside. This penetrated field has been called the optical near field [2]. The second feature, the short duration, means that the quasi-particle is a virtual photon. A dressed photon (DP) provides a physical picture

that describes these two features consistently, including the large number of normal modes and the spectral sideband features of (1) and (2), respectively.

For comparison, the exciton–polariton, represented by the curves A and B in Fig. 1.1, is a quasi-particle in a macroscopic material where the size of this material is much larger than the wavelength of light. This quasi-particle propagates toward the far-field and has been called a real photon; its momentum and energy are conserved ($\Delta k = 0, \Delta E = 0$). The behavior and properties of this real photon have been studied in conventional optical science and technology for a long time.

The curves A and B in Fig. 1.1 correspond to a physical system, which has been called "on shell" in quantum field theory [3–5]. On the other hand, the shaded gray rectangle has been called "off shell". Whereas the real photon on shell conserves its momentum and energy, the virtual photon off shell does not. The probability of creating virtual photons diminishes depending on how far off shell they are. The value of this probability is represented by the gradation depth of the gray rectangle.

Near-field optics has been developed to study and use the optical near field, i.e., the off-shell photon. Science and technology, in general, have clearly demarcated classical and modern ages. In the case of near-field optics, it has been recognized that the classical age started with the proposal to use optical near fields for high-resolution optical microscopy [6]. The viability of this proposal was subsequently supported through experiments using microwaves [7]. Theoretical studies were undertaken to analyze the diffraction and radiation of electromagnetic waves through a small aperture [8, 9]. Afterward, a self-consistent theory was developed to solve many-body problems for analyzing the optical microscope image of a specimen [10]. Several institutes around the world embarked, almost simultaneously, on experimental studies on near-field optical microscopy [11], which provided a new methodology for measuring and analyzing the conformation and structure of sub-wavelength sized specimens. It should be noted that the studies in this classical age were carried out in the framework of wave optics.

In the case where the optical near field is applied to microscopy, however, an important problem is that non-demolition measurement is not guaranteed because the optical properties of the specimen are inevitably perturbed by optical near field energy transferred from the tip of the probe to the specimen. This difficulty in guaranteeing non-demolition has been pointed out in the many-body problems described above, which means that microscopy may not be the most appropriate application of the optical near field. In other words, there is a strong desire to advance from the classical age of near-field optics. In response to this, the modern age of near-field optics started and appropriate applications have been found.

Since sub-wavelength sized nanometric materials (nanomaterials) are placed in close proximity to each other and are involved in the interaction mediated by the off-shell photon, the study of this photon is nothing more than the study of a light–matter interaction in nanometric space. This investigation progressed in two directions in the modern age, depending on the species of nanomaterials used.

One uses molecules or semiconductor nanomaterials. The light–matter interactions involving these specimens were analyzed by considering the discrete energy levels of the electrons in the molecules or those of the electron–hole pairs in the semi-

conductor. A successful and appropriate example application of this in the modern age is novel quantum optical functional devices developed based on this approach [12].

The other uses metallic nanoparticles or metallic films. Since it is fairly easy to fabricate and use these specimens, a variety of studies have been carried out. The mainstream approach was to study phenomena that originate from the coupling between the lightwave and plasmons, by which the plasma oscillation of the free electrons in a metal was manifested [13]. Since the collective motion of electrons is involved in this coupling, optical energy is converted promptly to plasma oscillation energy. Furthermore, since the phase-relaxation time of the electrons is very short, the unique properties of light, such as its quantum optical properties, can be promptly lost in the metal. Therefore, to analyze these plasmonic phenomena, it was sufficient to use quantities from conventional wave optics, such as refractive index, wavenumber, guiding mode, and the dispersion relation (the curves A and B in Fig. 1.1). In other words, these analyses were still based on the wave-optics principles of the classical age, as with the case of optical microscopy described above.

The following sections review recent progress in dressed photon technology, i.e., modern near-field optics [14]. This includes theoretical studies that present an intuitive physical picture of the dressed photon for analyzing light–matter interactions in nanometric space, applications to novel optical functional devices, nano-fabrication, energy conversion, photon breeding devices, and information processing systems. A future outlook of dressed photon technology will be also given, hinting at the possibilities in this field.

1.2 The Dressed Photon as a Physical Picture of an Off-Shell Photon

Light–matter interactions in nanometric space can exhibit unique variations in the values of the physical quantities of nanomaterials, such as momentum and energy. There are unsolved problems and untouched subjects in analyzing these variations, including:

(1) Quantum field theory is required to describe the numbers of photons and electron-hole pairs in a many-particle system, which can vary as a result of light–matter interactions in a nanometric space. For this description, creation and annihilation operators have to be defined by quantizing the light and elementary particles. However, in the conventional quantum theory of light, the concept of an on-shell photon has been established by quantizing the electromagnetic field of light that propagates through macroscopic free space whose size is larger than the wavelength of light [15]. The on-shell photon corresponds to an electromagnetic mode in a virtual cavity defined in free space for quantizing light. However, a serious problem for off-shell photon is that a virtual cavity cannot be defined in a sub-wavelength sized nanometric space, which makes it difficult to derive the

Hamiltonian of the optical energy. In addition, the wavelength (wave-number) of light and the photon momentum have large uncertainties due to the sub-wavelength size of the space under study.

(2) The off-shell photon is generated and localized on the surface of a nanomaterial under light irradiation. Furthermore, this photon corresponds to virtual photons mediating the interaction between the polarizations induced on the nanomaterial surface. Therefore, for detecting this photon, another nanomaterial has to be placed in close proximity to convert the virtual photon to the real photon via multiple scattering of the virtual photon. This conversion enables detection of the virtual photon through detection of the scattered light in the far field region. Through these processes, generation and detection of the virtual photon are achieved. Here, the first and the second nanomaterials may be regarded as the source and detector of the virtual photon, respectively. However, in contrast to conventional optical phenomena, the source and detector are not independent of each other but are coupled via the virtual photon.

(3) In practice, nanomaterials are fixed on a macroscopic substrate or buried in a macroscopic host crystal. Furthermore, they are surrounded by macroscopic electromagnetic fields belonging to the applied propagating light and scattered light. In short, since the nanomaterials in an actual nanometric subsystem are always surrounded by a macroscopic subsystem composed of macroscopic materials and electromagnetic fields, the contribution from the macroscopic subsystem must be taken into account to analyze the interaction between the nanomaterials for estimating the magnitude of the resultant energy transfer and dissipation in the nanometric subsystem.

Novel theories have been developed to solve problems (1)–(3) above, and these theories have succeeded in painting a physical picture of the optical near field and virtual photon consistently, which was outside the scope of conventional classical and quantum optics that were designed for the on-shell photons in the macroscopic space. Solutions to problems (1)–(3) are:

(a) In order to solve problem (1), an infinite number of electromagnetic modes with infinite frequencies, polarization states, and energies was assumed, which corresponds to representing the large number of normal modes and the spectral sideband features of (1) and (2) in Sect. 1.1, respectively. An infinite number of energy states was also assumed for the electrons and holes. Based on these assumptions, the total Hamiltonian was derived to define the creation and annihilation operators of a quasi-particle in order to represent the light–matter interaction in a nanometric space [16]. Since these operators are given by the sum of the operators of photons and electron–hole pairs, this quasi-particle was named a dressed photon (DP), which is a photon that dresses the material energy, i.e., the energy of the electron–hole pair [17]. As a result, it was concluded that the DP was modulated temporally and spatially because of the infinite electromagnetic modes and infinite energy states. The temporal modulation feature was represented by an infinite number of modulation sidebands. That is, even though the

nanomaterial was irradiated with propagating light of a single mode, the generated DP had an infinite number of modulation sidebands. It was also found that the DP could couple with multi-mode coherent phonons in the nanomaterial to create another quasi-particle, named the dressed-photon–phonon (DPP) [18].

(b) In order solve problem (2), the theoretical approach reviewed in (a) was used to analyze the interaction between the two nanomaterials by using the concepts of the annihilation of a DP from the first nanomaterial and its creation on the second nanomaterial. Furthermore, it was also found from experimental and theoretical studies that the second particle exhibits a unique optical response if it absorbs the energy of the modulation sideband described in (a), which is different from the conventional optical response induced by absorbing on-shell photons [19].

(c) In order to solve problem (3), the virtual photon interaction between the nanomaterials in the nanometric subsystem was analyzed by renormalizing the effects originating from the macroscopic subsystem in a consistent and systematic way. This renormalization was carried out by using the projection operator method [20]. As a result, the spatial distribution of the virtual photon interaction energy was derived and expressed by using a Yukawa function, which also succeeded in representing the interaction between the two nanomaterials mediated by the DP (DP-mediated interaction) [21]. This function quantitatively showed that the interaction range was equivalent to the size of the nanomaterial and did not depend on the wavelength of the incident propagating light. Originating from this size-dependent interaction range, novel optical response characteristics were found: Since the DP is localized in nanometric space, the long-wavelength approximation, which is valid for conventional light–matter interactions in macroscopic space, is not valid for the DP-mediated interaction. As a result, an electric dipole-forbidden transition turned out be allowed. Furthermore, size-dependent resonance was also found [22]. That is to say, the efficiency of the energy transfer between nanomaterials depends on the size of the nanomaterials that are interacting. It should be noted that this resonance is unrelated to diffraction that governs the conventional wave-optical phenomena.

In the classical age, the name optical near field has been used for representing the spatial features of the light generated on the surface of a nanomaterial. In the modern age, the term optical near field was replaced by DP, which is the quasi-particle representing the coupled state of photons and electron-hole pairs in a nanometric space. This replacement has been successful in describing the light–matter interactions in a nanometric space accurately.

1.3 Applications of Dressed Photons

This section reviews several applications that have been developed by using the intrinsic features of the DP-mediated interaction and the resultant DP energy transfer described in Sect. 1.2. Several examples, to be reviewed in Sects. 1.3.1–1.3.3, has

been described in [23]. Novel theoretical models based on mathematical science, different from the theory described in (a)–(c) of Sect. 1.2, are also described, as well as a future outlook of dressed photon technology.

1.3.1 Optical Functional Devices

Novel optical functional devices, named DP devices, have been developed by using semiconductor nanomaterials. They enabled the transmission and readout of optical signals by the energy transfer and subsequent dissipation of the DP energy. The operation of these DP devices was analyzed by using a quantum mechanical master equation based on a density matrix formulation for describing the DP-mediated interaction between nanomaterials [24].

Examples of DP devices developed so far are: a logic gate device for controlling optical signals [12], an energy transmitter for transmitting optical signals between DP devices [25], and an input interface device for converting incident an on-shell photon to a DP [26]. Furthermore, a unique delayed-feedback-type optical pulse generator has been proposed for use as a DP signal pulse generator [27]. Practical NOT gate and AND gate devices that operate at room temperature have also been fabricated by using InAs nanomaterials [28].

One advantage of these devices is their extremely small volume, far beyond the diffraction limit of propagating light. Other advantages are their superior performance levels and unique functionality, such as high figures of merit [29], low energy consumption [30], tamper-resistance [31], skew-resistance [32], and autonomous energy transfer [33], all of which originate from the unique operating principles of DP devices, utilizing electric-dipole-forbidden transitions and size-dependent resonance of DP-mediated interactions, as described in (c) of Sect. 1.2.

1.3.2 Nano-fabrication

This subsection reviews two examples of nano-fabrication technologies based on the intrinsic nature of the DP. The first example is lithography using DPs generated at the aperture of a photo-mask. In classical near field optical technology, linearly-aligned aperture patterns on a photo-mask have been transcribed to a photo-resist film [34]; however, sufficiently high resolution has not been obtained because the photo-resist is exposed also by the diffracted on-shell photons transmitted through the aperture pattern. In order to avoid this exposure, a novel method has been developed by irradiating a UV-sensitive photo-resist with visible light. It should be noted that the UV-sensitive photo-resist can be excited by DPs even though they are generated from visible light. This is possible because the DPP has high-frequency sidebands of modulation, generated as a result of temporal modulation (refer to Sect. 1.2). In other words, this is possible due to the energy up-conversion via energy levels of

coherent phonons in DPPs. As a result, the photo-mask pattern can be accurately transcribed to the photo-resist while the photo-resist remains un-exposed by the visible on-shell photon transmitted through the apertures [35]. With this method, a diffraction-free resolution as high as that determined by the aperture size has been realized by a compact lithography machine for practical use [36]. This method has enabled duplication of an integrated circuit pattern, multiple exposure, and pattering using an optically inactive photo-resist [35]. As applications of this method, a two-dimensional array of DP devices [37], a diffraction grating for soft-X rays [38], and a Fresnel zone plate for soft-X rays [39] have been fabricated.

The second example is smoothing a material surface by photochemical etching. In this process, bumps on a rough material surface are autonomously removed by chemically radical atoms. These atoms are created by photo-dissociating gaseous molecules using energy up-conversion, as was the case with the lithography described above, due to DPP energy transfer from the apex of the bump to the molecules under visible light irradiation [40]. Using this method, the surfaces of glass substrates have been smoothed for use as high-power laser mirrors [41], for magnetic storage memory disks [42], and for EUV masks [43]. Side walls of densely aligned corrugations of a diffraction grating have been also smoothed [44]. This method has been applied to other materials, such as plastic PMMA [45], crystalline GaN [46], and crystalline diamond [47]. This method realizes high-throughput smoothing because no special devices, like a fiber probe or a photo-mask, are required for generating the DPs and DPPs. Furthermore, because no mechanical components are required, this method can be more advantageous than conventional chemical-mechanical polishing [48], which uses a sliding pad on the material surface to be polished. Based on a principle equivalent to the smoothing reviewed above, scratches on a transparent poly-Al_2O_3 crystal surface have been filled-in by using chemical vapor deposition in order to smooth the substrate surface for ceramic laser media applications [49].

1.3.3 Energy Conversion

Conversions between optical and electrical energies have been realized based on energy up- or down-conversions by using DPs and DPPs. These include:

(1) Optical-to-optical energy conversion: Near infrared light has been converted to visible light by using energy up-conversion in the process of DPP energy transfer between organic dye particles. Red, green, and blue light has been emitted from DCM, coumarine 540A, and stilbene 420 particles, respectively, by irradiating them with 0.8–1.3 μm wavelength infrared light [50, 51]. These conversion methods have been applied to infrared optical pulse shape measurements [52]. On the other hand, energy down-conversion by DPPs has been applied to convert short-wavelength light to long-wavelength light. For example, a high-efficiency down-conversion method has been developed by using nanometric droplets autonomously grown in an optically curable resin [53–55].

(2) Optical-to-electrical energy conversion: Novel devices have been developed for efficiently converting optical energy to electrical energy, using the energy up-conversion via DPPs. One example is a photovoltaic device using an organic film of P3HT. The electrode surface conformation of this device was autonomously modified by using novel DPP-assisted deposition of silver particles for efficient DPP generation [56]. Another example is a Si photodiode in which the spatial distribution of doped boron atoms was autonomously modified by a novel DPP-assisted annealing method [57], as have been used in fabricating the photon breeding devices to be reviewed in Sect. 1.3.4. In these two examples, effective energy conversion has been confirmed even when the photon energy of the incident light is lower than the bandgap energy E_g of the semiconductor materials used. Furthermore, in the case of the Si photodiode, an optical amplification capability was confirmed, which was due to stimulated emission triggered by the DP. This optical amplification was also used to installed to the visible Si photodiode in order to increase the sensitivity of detecting a blue-ultraviolet light with the photon energy higher than E_g [58].

1.3.4 Photon Breeding Devices

This subsection reviews novel electrical-to-optical energy conversion devices, which are novel light emitting diodes (LEDs) fabricated by using Si bulk crystals [59–62] and indirect transition-type semiconductors. The autonomous modification method reviewed in (2) of Sect. 1.3.3 was also used, resulting in efficient momentum transfer between electrons and phonons in Si. After the autonomous modification, the Huang-Rhys factor [63], a parameter representing the magnitude of the coupling between electron–hole pairs and phonons, was determined to be 4.08 ± 0.02 [64], which is 10^2–10^3 times higher than that of a conventional Si crystal device. Furthermore, it was confirmed that the DPs coupled with the coherent phonons of the longitudinal optical mode, creating DPPs [65]. Besides Si, an indirect transition-type GaP semiconductor has been used for fabricating an LED emitting yellow-green light [66, 67]. An indirect transition-type SiC semiconductor has also been used for fabricating LED emitting blue-violet light [68], ultraviolet light [69], and white light [70]. In addition to LEDs, an optical and electrical relaxation oscillator [71] and a near infrared laser have been realized by using crystalline Si [72–74]. Furthermore, an LED [75], a light polarization rotator [76], and a light beam deflector [77] have been developed by using ZnO crystal. A light polarization rotator using SiC crystal has been also developed [78]. It should be pointed out that the fabrication and operation principles of these devices are different from those of conventional LEDs and lasers fabricated by using direct transition-type semiconductors. This subsection describes these differences.

To realize a device by using a Si bulk crystal, DPPs are used two times: first for device fabrication, and second for device operation.

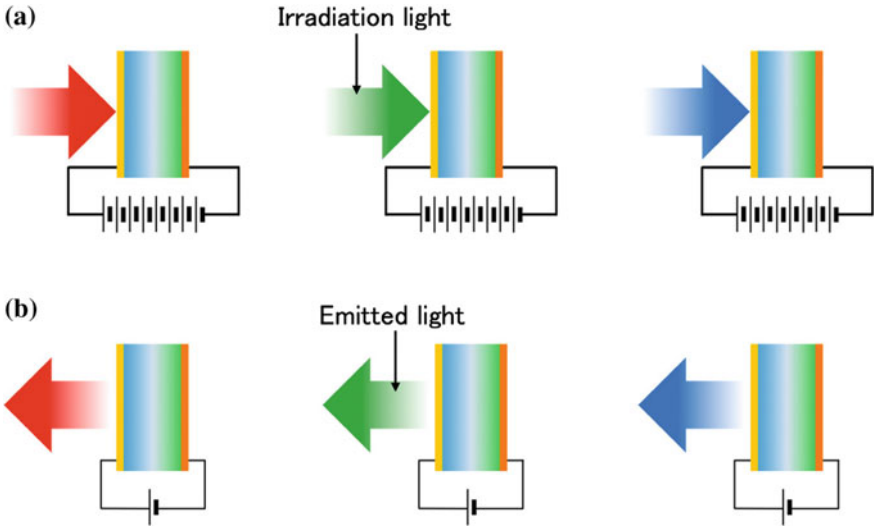

Fig. 1.2 Fabrication **a** and operation **b** of a photon breeding device

(1) For device fabrication, a p–n homojunction formed in the Si crystal is annealed, via Joule-heat produced by current injection, in order to diffuse boron (B) atoms (the p-type dopant). During the annealing, the Si crystal surface is irradiated with light (Fig. 1.2a) to create DPPs on the B atom surface. Driven by the created DPPs, electron–hole recombination takes place, emitting light. Since the energy of the emitted light dissipates from the Si crystal, the efficiency of the Joule-heating decreases. As a result, a unique spatial distribution of B atoms is realized, which depends on the created DPP energy. This novel annealing is called DPP-assisted annealing. In this spatial distribution, neighboring B atoms form a pair, and the resultant B atom-pair orients in a specific direction to efficiently create localized phonons [79].

(2) For the operation of the fabricated Si-LED, the light irradiation is not required any more; it is used only during the DPP-assisted annealing. Only forward current that is much lower than that used for annealing is injected, as is the case of the conventional LED operation. By this forward current, an electron is injected into the conduction band at the p–n homojunction and creates a photon by spontaneous emission even though its probability is very low. However, once this photon is created, it subsequently creates a DPP on the surface of the B atom at the p–n homojunction, and this DPP interacts with another electron in the conduction band to exchange momentum so that a secondary photon is created. By repeating these momentum exchange and photon creation processes, the emitted light intensity is amplified and reaches a stationary value within a short duration, so that light with a sufficiently high intensity is emitted from the p–n homojunction.

It should be noted that photon breeding occurs during device operation [80]. As a result, the photon energy of the emitted light is equal to the photon energy $h\nu_{aneal}$ of the light irradiated during the annealing (Fig. 1.2b). This is in contrast to a conventional device, where the photon energy of the emitted light is determined by the bandgap energy E_g of the semiconductor material used. This is because the difference between $h\nu_{aneal}$ and E_g is compensated for by the energy of the created phonons. This means that the photon energy of the light emitted from the device is identical to $h\nu_{aneal}$. This is because the spatial distribution of the B atoms has been controlled by the light irradiated during the DPP-assisted annealing, enabling most efficient stimulated emission and spontaneous emission of photons with identical photon energy. In other words, the light irradiated during the DPP-assisted annealing serves as a "breeder" that creates photons with an energy equivalent to $h\nu_{aneal}$. This is the reason why this novel phenomenon is named photon breeding with respect to photon energy. Photon breeding has been observed in the radiation energy dissipation process from relativisitic jets in blazars [81, 82]. However, in this astrophysical phenomenon, a very-high-energy photon (X ray) is generated from a low-energy photon (infrared or visible light) by inverse Compton scattering with a charged particle. Therefore, the photon breeding discussed in this subsection, producing equal-energy photons by using a DPP in a nanometric-sized space in a material, is quite different from that described above. Due to this difference, the present photon breeding may have to be called "nano-photon breeding" in order to avoid confusion. However, this subsection uses the name "photon breeding" for conciseness.

Photon breeding has been observed not only for the photon energy but also for the photon spin [79]. For example, linearly polarized light is emitted from the LED if it was fabricated by irradiating linearly polarized light during the annealing step. (Remember that the light emitted from a conventional LED is not polarized.)

In summary, the principles, operation, and functions of the present devices are different from those of conventional LEDs and lasers because DPPs and electric dipole-forbidden transitions are involved. Furthermore, photon breeding occurs, so that the energy and spin of the emitted photons are identical to those of the light irradiated during the annealing. Due to this difference, it is appropriate to call this novel device "a third light source", or more concretely, "a photon breeding device". For the readers' convenience, the fabrication and performance of the photon breeding devices are summarized as follows:

1 Fabrication

(1.1) In DPP-assisted annealing, an electric current is injected into the sample while irradiating it with light (photon energy: $h\nu_{anneal}$).
(1.2) DPP-assisted annealing is possible even when the value of $h\nu_{anneal}$ is lower than E_g.
(1.3) The optimum condition for effective DPP-assisted annealing is that the ratio of the electron injection rate to the photon irradiation rate be set to 1:1.
(1.4) The sample's temperature during the DPP-assisted annealing can be as low as 400 K; in other words, an extremely high temperature is not required.

(1.5) Conventional thermal annealing, e.g., by heating the sample in an electric furnace, is not compatible with the fabrication of photon breeding devices.

2 Spatial distribution of the dopant atoms [79]

(2.1) As a result of DPP-assisted annealing, p-type dopant atoms (B atoms in the case of a Si crystal) form pairs. The separation, d, between the atoms in the pair is given by $d = na$, where a is the lattice constant of the crystal. The integer n satisfies the relation $h\nu_{anneal} = E_g - nE_{phonon}$, where E_{phonon} is the energy of the generated phonon.

(2.2) The orientation of the pair of the dopant atoms is perpendicular to the propagation direction of the light irradiated during the DPP-assisted annealing. Furthermore, in the case where this light is linearly polarized, it is also perpendicular to the direction of polarization.

3 Performance

(3.1) The fabricated devices exhibit electroluminescence by injecting an electric current.

(3.2) The photon energy of the emitted light is identical to $h\nu_{anneal}$; i.e., photon breeding takes place with respect to the photon energy.

(3.3) The polarization direction of the emitted light is identical to that of the light irradiated during the DPP-assisted annealing; i.e., the device exhibits photon breeding with respect to the photon spin [79, 83].

(3.4) When the device is fabricated under the condition described in (1.2) above, the photon energy of the emitted light is lower than E_g, as can be deduced from (3.2). Therefore, the emitted light is not absorbed by the crystal, enabling high efficiency and high output power [59, 66, 70, 73–75].

4 Family of photon breeding devices
The photon breeding devices that have been fabricated are listed in Table 1.1.

1.3.5 Information Processing Systems

Novel information processing systems using the DP devices reviewed in Sect. 1.3.1 have been proposed [84, 85]. A first example is a nanometric optical computing system utilizing the DP energy transfer [86]: Although several optical methods have been proposed by following the concepts of Von Neumann computing systems, the collapse of the scaling-law for computing time and energy consumption has remained a critical problem. In order to solve these problems, a non-Von Neumann computing system has been proposed by using DP devices, and its ability to solve decision making problems [87, 88], constraint satisfaction problems [89], and intractable computational problems [90] has been demonstrated.

A second example is an information processing system using the dissipations and fluctuations of the DP energy [91]. The last example is an information security

Table 1.1 Family of photon breeding devices [62]

Devices	Photon energy	Crystal	Refer to
Light emitting diode	Visible	Si	[58]
		SiC	[68–70]
		GaP	[66, 67]
		ZnO[a]	[75]
	Infrared	Si	[59–61]
Laser	Infrared	Si	[72–74]
Optical and electrical relaxation oscillator	Infrared	Si	[71]
Photodiode[b]	Infrared	Si	[57]
	Visible	Si	[58]
Modulator[c]	Visible	ZnO[a]	[76, 77]
		SiC	[78]

[a]Although ZnO is a direct transition-type semiconductor, a p-type semiconductor is difficult to fabricate by the conventional method
[b]Provided with optical amplification gain
[c]Light polarization rotator and light beam deflector

system that uses the size-dependent resonance of the DP energy transfer described in Sect. 1.2 [92]. This system has realized a hierarchical hologram [93], a lock-and-key [94] and nonsymmetric polarization transformation [95].

1.3.6 Novel Theoretical Models and Future Outlook

Novel theoretical models based on mathematical science, different from the theory described in (a)–(c) of Sect. 1.2, have been proposed for analyzing the spatio-temporal properties of DP energy transfer. By using these theoretical models, a novel information processing method has been developed by taking the hierarchy of the DP energy transfer into account [96]. These models have also been applied to analyze the dynamic process of material surface smoothing by photochemical etching, reviewed in Sect. 1.3.2 [97]. Furthermore, they have been applied to analyze nano-fabrication processes, such as morphological- and arrayed-structure formations on a material surface [98, 99]. By generalizing the model of [98], the essential role of DPs generated on the electrode surface has been clarified [100]. That is, a transition from a trivial particle-deposition state to a nontrivial self-controlled particle-deposition state was described. The properties of transition in this mesoscopic surface model in nonequilibrium were studied by the analogy of equilibrium phase transitions associated with critical phenomena. The criteria of transition was also discussed. Based on this generalized model, temporal variation of the dopant B atoms in Si crystal for the photon breeding devices were also analyzed [101]. It should be noted that the DP-mediated processes described in Sects. 1.3.2–1.3.4 were governed by the autonomy

of DP creation and annihilation. Therefore, for designing these processes, it is difficult to employ the deterministic methods that have been used to design and fabricate conventional materials and devices. In other words, since the autonomous creation and annihilation of DPs take place in multiple nanometric areas on the surface or inside the material, deterministic theoretical models of these processes inevitably involve an extremely long computing time. In order to shorten the computing time, the validity of the theoretical models above has been confirmed by the work described above.

In contrast to these models, a non-uniform light–matter interaction theory that directly solves the Schrödinger equation and Maxell equation simultaneously has been recently proposed [102]. This theory was also applied to study the DP effect on electron excitation in a nanomatric particle via model calculations combining a density matrix formalism and a classical Lorentz model [103]. The results were applied to investigate experimental observation by reinterpreting the results of the lithography of Sect. 1.3.2. This theory is expected to provide a powerful tool for rigorously analyzing light–matter interactions in nanometric space.

As a future outlook, it should be pointed out that there still remain problems to be solved for gaining a deeper understanding of DPs and exploring more applications. These include: (1) Improving the accuracy of the physical picture of the quasi-particle representing the coupled state of a photon, an electron, and a phonon in a nanometric space. (2) Elucidating the details of energy transfer and dissipation between nanomaterials, mediated by DPs or DPPs. (3) Elucidating the details of phonon-assisted light–matter interactions in nanometric space. (4) Elucidating the physical origins of autonomy and hierarchy. (5) Developing technical methods based on statistical mechanics, mathematical science, and numerical simulation to analyze and solve problems (1)–(4) above.

For more advanced methods that will allow us to see the DP and to describe its origin, further studies on the energy transfer from the nano- to macro-systems are required. In particular, as a comment on problem (4) above, the physics of this complex system have to be developed on the basis of micro–macro duality in quantum theory [104], which facilitates the formation of micro–macro composite systems consisting of the object physical systems and the probe systems [105]. The specific features that originate from the inherent hierarchy of DPs will be smoothly and conveniently described in this framework with the aid of category-theoretical concepts [106]. Furthermore, for describing the energy dissipation, a novel theoretical model has to be developed based on the non-equilibrium statistical mechanics of the open system.

Many phenomena in nature have similar features to those of the DP, and these have been observed in a variety of systems, including nano-systems, macro-systems, inorganic materials, and organic materials (Fig. 1.3). Examples include: the meson, light-dependent magnetosensitivity in drosophila [107], a light-harvesting photosynthetic system [108], natural computing observed in single-celled amoeboid organisms [87, 88, 90], weathering of rocks, photon breeding in the radiation energy dissipation from relativistic jets in blazars [81, 82], and a close binary star [109]. By clarifying the similarities and differences between these phenomena and those of the DP, we

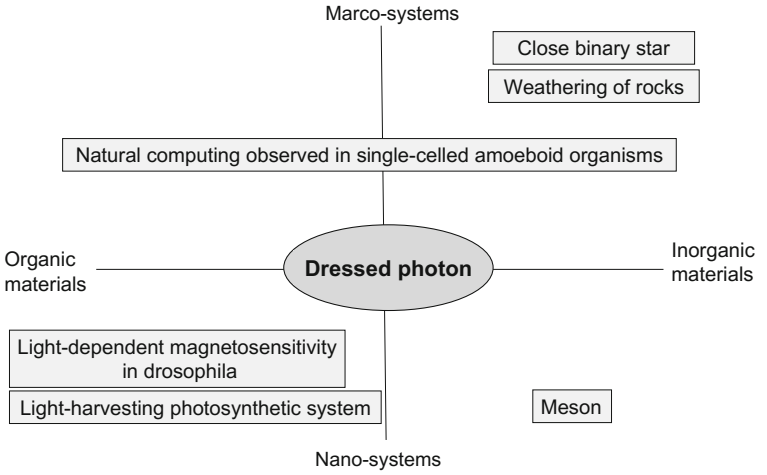

Fig. 1.3 Phenomena, which have similar features to those of the dressed photon

expect that it will be possible to establish a method of seeing the DP more precisely. A novel dressed photon technology, also called light–matter fusion technology, is expected to be established in the future via further studies of DPs, e.g., by investigating the possibility of coupling DPs not only with phonons but also with other types of primary excitations. As a result, this method will demonstrate that DP can be used to realize a generic technology of the 21st century.

1.4 Summary

This article discussed the concepts of dressed photon based on the off-shell photon picture. Applications made possible by this modern picture were reviewed, including optical functional devices, nano-fabrication technologies, energy conversion technologies, photon breeding devices, and information processing systems. Furthermore, novel mathematical scientific models were introduced, and finally, the future outlook for dressed photon technology was presented.

Acknowledgments The author thanks to Profs. I. Ojima (formerly Kyoto Uinv.), H. Saigo (Nagahama Inst. Bio-Sci. and Technol.), M. Katori (Chuo Univ.), H. Hori (Yamanashi Univ.), K. Kobayashi (Yamanashi Univ.), T. Kawazoe (Univ. of Tokyo), T. Yatsui (Univ. of Tokyo), N. Tate (Kyushu Univ.), Drs. M. Naruse (NICT), W. Nomura (Kyusyu Univ.) and K. Okamura (Nagoya Univ.) for their encouragement and collaborations throughout the course of the authors research work on dressed photon technology.

References

1. D. Pines, *Elementary Excitation in Solids* (Perseus Books, Reading, Massachusetts, 1999)
2. M. Ohtsu, K. Kobayashi, *Optical Near Fields* (Springer, Berlin, 2004)
3. M. Thomson, *Modern Particle Physics* (Cambridge Univ. Press, Cambridge, 2013), pp. 117–119
4. R.P. Feynman, *The Theory of Fundamental Processes* (W.A. Benjamin, New York, 1962), pp. 95–100
5. M. Ohtsu, H. Hori, *Near-Field Nano-Optics* (Kluwer Academic/Plenum Publishers, New York, 1999), pp. 29–31
6. E.H. Synge, Phil. Mag. **6**, 356 (1928)
7. E.A. Ash, G. Nicholls, Nature **237**, 510 (1972)
8. H. Bethe, Phys. Rev. **56**, 163 (1944)
9. C.J. Bouwkamp, Philips Res. Rep. **5**, 401 (1950)
10. C. Girard, D. Courjon, Phys. Rev. B **42**, 9340 (1990)
11. D.W. Pohl, D. Courjon (eds.), *Near Field Optics* (Kluwer, Dordrecht, 1993), pp.1–324
12. T. Kawazoe, K. Kobayashi, S. Sangu, M. Ohtsu, Appl. Phys. Lett. **82**, 2957 (2003)
13. V.A. Podolskiy, A.K. Sarychev, V.M. Shalaev, Opt. Express **11**, 735 (2003)
14. M. Ohtsu, Opt. Rev. **21**, 905 (2014)
15. J.J. Sakurai, *Advanced Quantum Mechanics* (Addison-Wesley, Reading, 1967), pp. 20–74
16. K. Kobayashi, Surf. Sci. **30**, 638 (2009). [in Japanese]
17. M. Ohtsu, *Dressed Photons* (Springer, Berlin, 2013), pp. 11–36
18. Y. Tanaka, K. Kobayashi, Physica E **40**, 297 (2007)
19. T. Kawazoe, K. Kobayashi, S. Takubo, M. Ohtsu, J. Chem. Phys. **122**, 024715 (2005)
20. H. Hyuga, H. Ohtsubo, Nucl. Phys. A **294**, 348 (1978)
21. K. Kobayashi, M. Ohtsu, J. Microscopy **19**, 2494 (1999)
22. S. Sangu, K. Kobayashi, M. Ohtsu, J. Microscopy **202**, 279 (2001)
23. M. Ohtsu, Program, in *Nanophotonics 1*, ed. by M. Ohtsu (Springer, Berlin, 2011), pp. 1–58
24. S. Sangu, K. Kobayashi, S. Shojiguchi, M. Ohtsu, Phys. Rev. B **69**, 1153343 (2004)
25. W. Nomura, T. Yatsui, T. Kawazoe, M. Ohtsu, J. Nanophotonics **1**, 011591 (2007)
26. T. Kawazoe, K. Kobayashi, M. Ohtsu, Appl. Phys. Lett. **86**, 103102 (2005)
27. M. Naruse, H. Hori, K. Kobayashi, T. Kawazoe, M. Ohtsu, Appl. Phys. B **102**, 717 (2011)
28. T. Kawazoe, M. Ohtsu, S. Aso, Y. Sawado, Y. Hosoda, K. Yoshizawa, K. Akahane, N. Yamamoto, M. Naruse, Appl. Phys. B **103**, 537 (2011)
29. M. Ohtsu, K. Kobayashi, T. Kawazoe, T. Yatsui, M. Naruse, *Principles of Nanophotonics* (CRC Press, Boca Raton, 2008), p. 122
30. M. Naruse, P. Holmstrom, T. Kawazoe, K. Akahane, N. Yamamoto, L. Thylen, M. Ohtsu, Appl. Phys. Lett. **100**, 241102 (2012)
31. M. Naruse, H. Hori, K. Kobayashi, M. Ohtsu, Opt. Lett. **32**, 1761 (2007)
32. M. Naruse, F. Pepper, K. Akahane, N. Yamamoto, T. Kawazoe, N. Tate, M. Ohtsu, ACM, J. Emerg. Technol. Comput. Syst. **8**, 1 (2012)
33. M. Naruse, K. Leibnitz, F. Peper, N. Tate, W. Nomura, T. Kawazoe, M. Murata, M. Ohtsu, Nano. Commun. Netw. **2**, 189 (2011)
34. M.M. Alkaisi, R.J. Blaikie, S.J. McNab, R. Cheung, D.R.S. Cumming, Appl. Phys. Lett. **75**, 3560 (1999)
35. H. Yonemitsu, T. Kawazoe, K. Kobayashi, M. Ohtsu, J. Photoluminescence **122–123**, 230 (2007)
36. Y. Inao, S. Nakasato, R. Kuroda, M. Ohtsu, Microelectron. Eng. **84**, 705 (2007)
37. T. Kawazoe, K. Kobayashi, K. Akahane, M. Naruse, N. Yamamoto, M. Ohtsu, Appl. Phys. B **84**, 243 (2006)
38. T. Kawazoe, T. Takahashi, M. Ohtsu, Appl. Phys. B **98**, 5 (2010)
39. M. Koike, S. Miyauchi, K. Sano, T. Imazono, *Nanophotonics and Nanofabrication*, ed. by M. Ohtsu (Wiley-VCH, Weinheim, 2009), p. 179

40. T. Yatsui, K. Hirata, W. Nomura, Y. Tabata, M. Ohtsu, Appl. Phys. B **93**, 55 (2008)
41. T. Yatsui, K. Hirata, Y. Tabata, W. Nomura, T. Kawazoe, M. Naruse, M. Ohtsu, Nanotechnology **21**, 355303 (2001)
42. W. Nomura, T. Yatsui, T. Kawazoe, N. Tate, M. Ohtsu, Appl. Phys. A **121**, 1403 (2015)
43. R. Teki, A.J. Kadaksham, M. House, J. Harris-Jones, A. Ma, S.V. Babu, A. Hariprasad, P. Dumas, R. Jenkins, J. Provine, A. Richmann, J. Stowers, S. Meyers, U. Dietze, T. Kusumoto, T. Yatsui, M. Ohtsu, Proc. SPIE **8322**, 83220B (2012)
44. T. Yatsui, K. Hirata, Y. Tabata, Y. Miyake, Y. Akita, M. Yoshimoto, W. Nomura, T. Kawazoe, M. Naruse, M. Ohtsu, Appl. Phys. B **103**, 527 (2011)
45. T. Yatsui, W. Nomura, M. Ohtsu, Adv. Opt. Technol. **2015**, 701802 (2015)
46. T. Yatsui, W. Nomura, F. Stehlin, O. Soppera, M. Naruse, M. Ohtsu, Beilstein J. Nanotechnol. **4**, 875 (2013)
47. T. Yatsui, W. Nomura, M. Naruse, M. Ohtsu, J. Phys. D **45**, 475302 (2012)
48. T. Yatsui, Hirabayashi. Proc. SPIE **8166**, 81663T (2011)
49. W. Nomura, T. Yatsui, Y. Yanase, K. Suzuki, M. Fujita, A. Kamata, M. Naruse, M. Ohtsu, Appl. Phys. B **99**, 75 (2010)
50. T. Kawazoe, H. Fujiwara, K. Kobayashi, M. Ohtsu, IEEE. J. Select. Top. Quantum Electron. **15**, 1380 (2009)
51. H. Fujiwara, T. Kawazoe, M. Ohtsu, Appl. Phys. B **98**, 283 (2010)
52. H. Fujiwara, T. Kawazoe, M. Ohtsu, Appl. Phys. B **100**, 85 (2010)
53. N. Tate, Y. Liu, T. Kawazoe, M. Naruse, T. Yatsui, M. Ohtsu, Appl. Phys. B **110**, 293 (2013)
54. N. Tate, Y. Liu, T. Kawazoe, M. Naruse, T. Yatsui, M. Ohtsu, Appl. Phys. B **110**, 39 (2013)
55. N. Tate, M. Naruse, Y. Liu, T. Kawazoe, T. Yatsui, M. Ohtsu, Appl. Phys. B **112**, 587 (2013)
56. S. Yukutake, T. Kawazoe, T. Yatsui, W. Nomura, K. Kitamura, M. Ohtsu, Appl. Phys. B **99**, 415 (2010)
57. H. Tanaka, T. Kawazoe, M. Ohtsu, Appl. Phys. B **108**, 51 (2012)
58. M. Ikegawa, T. Kawazoe, M. Ohtsu, in Abstracts of the 10th Asia-Pacific Conference on Near-field Optics (Hakodate, Japan, 7–10 July 2015), p. 106
59. T. Kawazoe, M.A. Mueed, M. Ohtsu, Appl. Phys. B **104**, 747 (2011)
60. M.A. Tran, T. Kawazoe, M. Ohtsu, Appl. Phys. A **115**, 105 (2014)
61. M. Yamaguchi, T. Kawazoe, T. Yatsui, M. Ohtsu, Appl. Phys. A **121**, 1389 (2015)
62. M. Ohtsu, *Silicon Light-Emitting Diodes and Lasers* (Springer, Berlin, 2016)
63. K. Huang, A. Rhys, Proc. R. Soc. Lond. Ser. A Math. Phys. Sci. **204**, 406 (1950)
64. M. Yamaguchi, T. Kawazoe, M. Ohtsu, Appl. Phys. A **115**, 119 (2014)
65. N. Wada, M.-A. Tran, T. Kawazoe, M. Ohtsu, Appl. Phys. A **115**, 113 (2014)
66. J.-H. Kim, T. Kawazoe, M. Ohtsu, Adv. Opt. Technol. **2015**, 236014 (2015)
67. J.-H. Kim, T. Kawazoe, M. Ohtsu, Appl. Phys. A **121**, 1395 (2015)
68. T. Kawazoe, M. Ohtsu, Appl. Phys. A **115**, 127 (2014)
69. Q.H. Vo, T. Kawazoe, M. Ohtsu, Ext. Abstr. (61st Spring Meet., March 2014); Japan Society of Applied Physics and Related Societies, 18A-F12-10 [in Japanese]
70. T. Kawazoe, M. Ohtsu, Ext. Abstr. (59th Spring Meet., March 2012); Japan Society of Applied Physics and Related Societies, 17p-B11-1 [in Japanese]
71. N. Wada, T. Kawazoe, M. Ohtsu, Appl. Phys. B **108**, 25 (2012)
72. T. Kawazoe, M. Ohtsu, K. Akahane, N. Yamamoto, Appl. Phys. B **107**, 659 (2012)
73. H. Tanaka, T. Kawazoe, M. Ohtsu, K. Akahane, Fluorescent Mat. **1**, 1 (2015)
74. H. Tanaka, T. Kawazoe, M. Ohtsu, K. Akahane, N. Yamamoto, Appl. Phys. A **121**, 1377 (2015)
75. K. Kitamura, T. Kawazoe, M. Ohtsu, Appl. Phys. B **107**, 293 (2012)
76. N. Tate, T. Kawazoe, W. Nomura, M. Ohtsu, Sci. Rep. **5**, 12762 (2015)
77. N. Tate, T. Kawazoe, S. Nakashima, W. Nomura, M. Ohtsu, in *Proceeding of The 22nd International Display Workshops (IDW15)*, (Otsu, Japan, 9–11 Dec 2015), p. 1066
78. T. Kawazoe, N. Tate, M. Ohtsu, in Proceedings The 22nd International Display Workshops (IDW15), (Otsu. Japan **9–11**, 1081 (Dec 2015)
79. T. Kawazoe, K. Nishioka, M. Ohtsu, Appl. Phys. A **121**, 1409 (2015)

80. M. Ohtsu, inProgress, in *Nanophotonics 3*, ed. by M. Ohtsu, T. Yatsui (Springer, Berlin, 2015), pp. 1–56
81. J. Poutanen, B.E. Stern, Mon. Not. R. Astron. Soc. **372**, 1217 (2006)
82. B.E. Stern, J. Poutanen, Mon. Not. R. Astron. Soc. **383**, 1695 (2008)
83. T. Kawazoe, K. Nishioka, M. Ohtsu, in *Proceedings of the 21st International Display Workshops (IDW14)*, (Niigata, Japan, 3-5 Dec 2014), p. 1061
84. M. Naruse, N. Tate, M. Aono, M. Ohtsu, in *Nanophotonic Information Physics*, ed. by M. Naruse (Springer, Berlin, 2013), p. 1
85. M. Naruse, N. Tate, M. Aono, M. Ohtsu, Rep. Prog. Phys. **76**, 056401 (2013)
86. C. Pistol, C. Dwyer, A.R. Lebeck, IEEE Micro. **28**, 7 (2008)
87. M. Naruse, M. Aono, S.-J. Kim, IEICE Trans. Commun. **E96-B**, 2724 (2013)
88. S.-J. Kim, M. Naruse, M. Aono, M. Ohtsu, M. Hara, Sci. Rep. **3**, 2370 (2013)
89. M. Naruse, M. Aono, S.-J. Kim, T. Kawazoe, W. Nomura, H. Hori, M. Hara, M. Ohtsu, Phys. Rev. B **86**, 125407 (2012)
90. M. Aono, M. Naruse, S.-J. Kim, M. Wakabayashi, H. Hori, M. Ohtsu, M. Hara, Langmuir **29**, 7557 (2013)
91. M. Takahashi, N.S. Humam, N. Tsumori, T. Saiki, P. Regreny, M. Gendry, Appl. Phys. Lett. **102**, 093120 (2013)
92. M. Naruse, N. Tate, M. Ohtsu, J. Opt. **14**, 094002 (2012)
93. N. Tate, M. Naruse, T. Yatsui, T. Kawazoe, M. Hoga, Y. Ohyagi, T. Fukuyama, M. Kitamura, M. Ohtsu, Opt. Express **18**, 7497 (2010)
94. N. Tate, H. Sugiyama, M. Naruse, W. Nomura, T. Yatsui, T. Kawazoe, M. Ohtsu, Opt. Express **17**, 11113 (2009)
95. M. Naruse, N. Tate, Y. Ohyagi, M. Hoga, T. Matsumoto, H. Hori, A. Drezet, S. Huant, M. Ohtsu, Opt. Express **21**, 21857 (2013)
96. M. Naruse, H. Hori, K. Kobayashi, M. Ishikawa, K. Leibnitz, M. Murata, N. Tate, M. Ohtsu, J. Opt. Soc. Am. B **26**, 1772 (2009)
97. M. Naruse, T. Yatsui, W. Nomura, T. Kawazoe, M. Aida, M. Ohtsu, Appl. Phys. Lett. **102**, 071603 (2013)
98. M. Naruse, T. Kawazoe, T. Yatsui, N. Tate, M. Ohtsu, Appl. Phys. B **105**, 185 (2011)
99. M. Naruse, Y. Liu, W. Nomura, T. Yatsui, M. Aida, L.B. Kish, M. Ohtsu, Appl. Phys. Lett. **100**, 193106 (2012)
100. K. Takahashi, M. Katori, M. Naruse, M. Ohtsu, Appl. Phys. B **120**, 247 (2015)
101. K. Takahashi, M. Katori, M. Naruse, T. Kawazoe, M. Ohtsu, Ext. Abstr. (70th Autumn Meet., Sept. 2015); Phys. Soc. Jpn, 18aCR-3 [in Japanese]
102. T. Iwasa, K. Nobusada, Appl. Phys. A **80**, 043409 (2009)
103. M. Yamaguchi, K. Nobusada, T. Kawazoe, T. Yatsui, Appl. Phys. Lett. **106**, 191103 (2015)
104. I. Ojima, in *Proceedings International conference on Stochastic Analysis*, ed. by T. Hida (World Scientific, 2005). arXiv:math-ph/0502038
105. I. Ojima, H. Saigo, Mathematics **3**, 897 (2015)
106. S. MacLane, *Categories for the Working Mathematician*, (Springer, 1971)
107. R.J. Gegear, A. Casselman, S. Waddell, S.M. Reppert, Nature **454**, 1014 (2008)
108. G. McDormott, S.M. Prince, A.A. Freer, A.M. Hawthornthwaite-Lawless, M.Z. Papiz, R.J. Cogdell, N.W. Isaacs, Nature **374**, 517 (1995)
109. R.W. Hilditch, *An Introduction to Close Binary Stars*, (Cambridge University Press, 2001)

Chapter 2
Nonequilibrium Statistical Mechanical Models for Photon Breeding Processes Assisted by Dressed-Photon-Phonons

Makoto Katori and Hirotsugu Kobayashi

Abstract The novel phenomenon called photon breeding realized in Si and GaP light emitting diodes (LEDs) fabricated by dressed-photon-phonon (DPP)-assisted annealing is studied from the viewpoint of nonequilibrium statistical mechanics. Experimental studies reported that the polarization and spectrum characteristics of the light irradiated in fabrication are embedded in spatial configurations of B and Zn atoms doped in the crystals of Si and GaP, respectively, and they are inherited to the light emitted from the LEDs. Stochastic models are introduced to simulate this phenomenon. There the diffusive motion of doped atoms in the DPP-annealing is represented by an interacting random-walk model on a lattice, which shows an aggregation process to make pairs of particles with specified separations. On the spatial structure of these pairings, which corresponds to the experimental condition that phonons with specified momenta are created successively, coupling of electrons and photons are phenomenologically expressed by coupled Poisson processes. Numerical results on the model systems qualitatively explain many basic properties of photon breeding both in fabrication and operation processes observed in experiments.

2.1 Introduction

The present authors are statistical physicists and have learned the recent progress of researches on dressed photon phenomena by reading the book written by Motoichi Ohtsu entitled 'Dressed Photons—Concepts of Light-Matter Fusion Technology' (2014) [1]. The dressed photon (DP) and the dressed-photon-phonon (DPP) are

M. Katori (✉)
Faculty of Science and Engineering, Department of Physics, Chuo University,
1-13-27 Kasuga, Bunkyo-ku, Tokyo 112-8551, Japan
e-mail: katori@phys.chuo-u.ac.jp

H. Kobayashi
Faculty of Business Administration, Department of IT Solutions,
Business Breakthrough University, Koujimach Square Bldg.
2F 3 Nibancho Chiyoda-ku, Tokyo 102-0084, Japan
e-mail: hikobayashi@ohmae.ac.jp

M. Ohtsu and T. Yatsui (eds.), *Progress in Nanophotonics 4*,
Nano-Optics and Nanophotonics, DOI 10.1007/978-3-319-49013-7_2

compound states of photon and electron, and photon, electron, and phonon, respectively, and thus they are quantum mechanical objects. We have found, however, the notion of DP and DPP and the observed mesoscopic and macroscopic phenomena associated with DP and DPP are very interesting also from the viewpoint of nonequilibrium statistical physics. It should be noted that the DP and DPP states cannot be sustained in chemical and thermal equilibrium, and hence they should be considered as 'dynamical states' of the elementary particles cooperating to maintain highly nontrivial mesoscopic and macroscopic stationary states in dissipative open systems. First we would like to discuss the aspects of DP and DPP phenomena, which stimulate us.

1. Important DP and DPP processes used in new light-matter fusion technology and informatics reported in [1–5] are realized in open systems in nonequilibrium. There energy, matter, and information are injected into a system (for instance, by irradiation light and electric current) and we get useful output from the system (for instance, as the light emission with specified polarization and wavelength stimulated by DPPs) in dissipative open systems. The physical states treated there are out of thermal and chemical equilibrium, but they seem to be stable and have a kind of robustness, if some conditions imposed both on input and output are satisfied.
   One of the most important topics in modern statistical physics is extension of the Boltzmann-Gibbs scheme for thermal and chemical equilibrium statistical mechanics into the generalized formula which is applicable to nonequilibrium but steady-state phenomena. Fruitful examples are found in the extensive studies on the generalized *fluctuation theorem* for currents of heat and matter [6, 7] in the systems related to traffic current problems and time evolution of random rough surfaces [8–10].
   The DP technology and informatics control transformation and transmission of energy, matter, and information in dissipative open systems with large numbers of degrees of freedom. Control of transmission will be supported by effective suppression of dissipation of energy, matter, and information, and dissipation should be related to fluctuations of the systems. DP experiments are expected to provide useful data for developing basic researches of nonequilibrium statistical mechanics.
2. In a previous paper [11], one of the present authors improved the stochastic cellular-automaton model of Naruse et al. [12] for the self-controlled particle-deposition process assisted by DPP. This process was experimentally realized by Yukutake et al. [13] on an electrode of a novel photovoltaic device as a process of Ag deposition under irradiation light. As discussed in [11–13], Ag deposition assisted by DPP gives a feedback mechanism to create DPP inside of the device. Therefore, when the unique granular structure of Ag file is formulated successfully on the electrode surface, the creation of DPP is automatically stopped and the system is stabilized.

Such a self-controlled process will be related to the physical property called the *self-organized criticality*, which has been extensively studied in statistical physics [14–17]. A typical model showing the self-organized criticality studied in statistical physics is the *sandpile model*, in which the discrete random variable defined on each lattice site represents the height of sandpile at that location. Given an inhomogeneous configuration of sandpiles on a finite lattice, we give a local perturbation; that is, we choose a site randomly and add one grain of sand at this site. In some situation, it makes the slope around this site be larger than the rest angle and causes a toppling of grains of sand into surrounding sites. Such a toppling can make sandpiles on neighboring sites be unstable and will cause successive topplings. We assume the open boundary condition in this finite lattice-system such that grains of sand dissipate to outside of the system through the edges of lattice. Due to this dissipation mechanism, chain reactions of toppling will cease soon or later, but their spatial scales and time durations are distributed depending on the sandpile configuration when the first toppling occurred. The chain reactions of topplings are called *avalanches*. The important point of this model is that the local perturbation is put only after each avalanche ceases. In other words, the time scale of intervals for local perturbations is assumed to be larger than the time durations of avalanches, even though each avalanche consists of in general a large number of topplings which change local sandpile-configuration quickly. In this way the sandpile model represents a *hierarchical structure involved in dynamics*, and it is considered to mimic the unpredictable behavior of earthquakes [17, 18].

Here we would like to point out the fact that hierarchical structures in space and time play important roles in DP and DPP phenomena as explained in Chap. 8 of [1]. Emergence of complex patterns from rather simple mechanisms has been extensively studied in physics of *fractals* and *pattern formations* [19], and of self-organized criticality [20]. DP and DPP phenomena are expected to provide a lot of interesting open problems for these research fields [21].

3. DP and DPP are 'fundamental particles' which trigger and also work to sustain many novel processes reported in [1–5], but they are not elementary particles. If we divide them into the elementary particles; photon, electron, and phonon, we cannot expect such new phenomena. Reductionism has been a standard strategy in modern sciences, but now we often encounter the situations in which the fundamental objects and principles are not unique and we have to take into account plural fundamentals simultaneously at the basic level to understand higher level structures. Systems in such situations are generally called *complex systems* in modern statistical physics.

   Most famous particle which plays a 'fundamental' role in phenomena and also in theories, but is not an elementary particle is the Brownian particle. A typical particle which executes the Brownian motion is a small granular particle in cavities inside pollen grains, when it is put in water. As a matter of course, such a granular particle is not an elementary particle, which consists of a large number of molecules and thus is visible through a microscope. The granular particle cannot move by itself. Random motion of such a tiny but still visible particle observed in water

is caused by its successive random collisions with a tremendously large number of invisible molecules of water surrounding it. Even though the Brownian particles are not elementary particles, we can discuss microscopic descriptions of diffusion processes using Brownian particles; e.g., the diffusion equation is regarded as an equation describing the averaged behavior of trajectories of a single Brownian motion. Here it seems that the derivation of Brownian motion from interacting systems of a granular particle and infinite number of water molecules is only phenomenological. It should be emphasized the fact that, however, once the basic properties of Brownian motion as a 'fundamental particle' are defined, we can construct a rigorous theory for many particle systems as well as infinite particle systems of Brownian particles. Recent progress in probability theory shows that Itô's stochastic calculus starting from the Brownian motion gives us a powerful theory for critical phenomena associated with continuous phase transitions and for random fractal patterns on a plane (the Schramm-Loewner Evolution, see, for instance, [22]). Random matrix theory [23] was originally a statistical theory for matrices whose entries are random variables, but recently it has been developed to the stochastic theory for matrix-valued processes whose entries are Brownian motions. The eigenvalue processes of such matrix-valued diffusion processes (e.g., Dyson's Brownian motion models) provide highly nontrivial particle systems called log-gases in which correlations among particles are very strong and long-ranged, but which are exactly solvable in some cases [22, 24].

We agree that the basic researches of DP and DPP phenomena should be performed in order to derive the fundamental properties of DP and DPP from elementary theories of physics and mathematics, e.g., quantum mechanics, quantum field theory, and category theory. At the same time we believe that there will be another direction of researches on DP and DPP, which is aimed to construct mesoscopic and macroscopic theory for the phenomena. There DP and DPP will be regarded as 'fundamental particles'. We think that notions and techniques developed in probability theory, in particular, the calculus concerning conditional probabilities [22] will be useful in this direction of researches.

Mathematical modeling and analysis of the DP and DPP phenomena using stochastic processes were pioneered by Naruse, and a series of papers have been already published [11, 12, 25–27]. In the present paper, we will concentrate on the novel phenomenon called *photon breeding*, which is recently observed in the fabrication and operation processes of infrared Si and GaP light-emitting diodes (LEDs) reported in [28–30]. In Sect. 2.2, we will briefly review the experimental results and considerations given in [28–30]. There we will list up the important observations and the fundamental properties of DPP. Then in Sect. 2.3, based on the nonequilibrium statistical mechanics, we propose a family of stochastic models with a set of external and internal parameters defined on lattices showing the photon breeding processes. Simulation results and analysis of them are reported in Sects. 2.4–2.7. Future problems are discussed in Sect. 2.8.

2.2 Experimental Results

2.2.1 Si-LED

Kawazoe et al. [29] reported the polarization-controlled infrared LED fabricated by DPP-assisted annealing of a Si crystal. Since the present theoretical study is based on their experimental results, here we give a brief review of them.

2.2.1.1 Fabrication of Si Crystal with Doped B by DPP-Assisted Annealing

An As-doped n-type Si crystal was prepared, where the electrical resistivity was 10 Ω cm. The top surface of the Si crystal was a (001) plane. Assume that the three-dimensional Cartesian coordinates (x_1, x_2, x_3) are introduced such that the top surface of the Si crystal is located on the x_1-x_2 plane at $x_3 = 0$, which makes a square with size $L = 3$ mm. The thickness of the Si crystal used in the experiment was 625 μm, thus the bottom surface of the crystal is assumed to be located at $x_3 = -625$ μm. See Fig. 2.1. By ion implantation B atoms were doped to form a p-type layer in the upper part of this crystal. The implantation direction was the negative direction of the x_3-axis, normal to the x_1-x_2 plane. The secondary ion mass spectroscopy showed that the B atoms are doped only in a rather thin layer between $x_3 = -1.5\,\mu$m and $x_3 = -2.0\,\mu$m. The concentration of B atoms attains its maximum value at $x_3 \simeq -1.8\,\mu$m, which is only about 0.04 % of the Si atom concentration (see Fig. 1 of [29]). Since the size of the Si crystal is 3 mm × 3 mm × 625 μm as mentioned above, we can say the following as an experimental fact.

[E1] The region of Si crystal doped by B atoms will be well approximated to be two-dimensional. The concentration of B in the Si crystal is relatively low even in this quasi-two-dimensional domain.

This layer plays as the p-n homojunction. For the DPP-assisted annealing, a forward bias voltage was applied to inject the electric current I (170 mA) and Joule heat was generated.

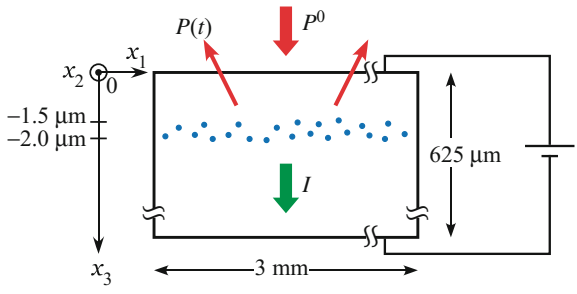

Fig. 2.1 Schematic figure showing the fabrication process of Si-LED

[E2] The Joule heat given by the injected electric current I causes the B atoms to execute diffusion processes and the spatial distribution of their locations were changing in time during the annealing.

Infrared light was incident normally on the top surface during the annealing. The power density and wave length were 3.3 W cm^{-2} and 1.342 μm, respectively. The photon energy was $h\nu_{\mathrm{anneal}} = 0.924$ eV. This photon energy $h\nu_{\mathrm{anneal}}$ is lower than the bandgap energy of Si, $E_{\mathrm{g}} = 1.12$ eV, and thus the irradiation light cannot be absorbed by the Si crystal.

[E3] The incident light propagates through the Si crystal and reaches the layer (the quasi-two-dimensional region) where B atoms exist and diffuse in the annealing.

In the annealing process, it was verified that the spatial distribution of B atoms reaches a stationary state. By the atom-prove field ion microscopy with subnanometer resolution, it was proved that B atoms formed pairs with specified separation $d = \delta a$, where a denotes the lattice constant of Si crystal and δ is an integer. Kawazoe et al. [29] argued that the B-atom pairs create phonons and, when the separation of pair is $d = \delta a$, the most frequent number of created phonons was equal to δ. The distribution of the spacing $d = \delta a$ in the stationary state of B atoms was measured by the atom-prove field ion microscopy and it was concluded that the typical spacing is given by $d = 3a$, that is, the most frequent number of photons created at a pair of B atoms is $\delta = 3$. The energy of relevant optical mode phonon is evaluated as $E_{\mathrm{phonon}} = 65$ meV and thus we see that

$$E_{\mathrm{g}} - 3E_{\mathrm{phonon}} = 1.12 - 3 \times 0.065 = 0.925\,\mathrm{eV} \tag{2.1}$$

coincides with the energy value of the light incident in the annealing, $h\nu_{\mathrm{anneal}} = 0.924$ eV. Moreover, Kawazoe et al. [29] showed the fact that the three phonons indeed compensate the momentum gap between the bottom of the conduction band (the X-point) and the top of the valence band (the Γ-point) in the energy band diagram of Si.

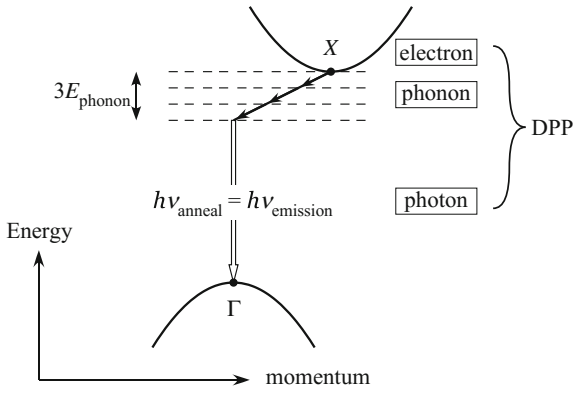

Fig. 2.2 Schematic figure showing the cooperation of photon, electron, and phonon in the proton breeding process. Such a dynamical combination of these elementary particles is regarded as a quasi-particle called a dressed-photon-phonon (DPP)

See Fig. 2.2. Hence electrons in the conduction band can change their momenta via interaction with the three phonons created at the pairs of B atoms and are allowed to execute transition down to a level in the valance band by emitting photons stimulated by incident light. This cooperation of photon, electron, and phonon is regarded as creation of DPP. The values of energy and wavelength of emitted light should be equal to those of incident light, since the photon creation by DPP is realized due to the exact matching of energy and momenta among photon, electron, and phonon as mentioned above. These basic properties of light are inherited from the incident light to the emitted light in this photon creation, and that is the reason why this process is called *photon breeding* [28, 29]. We summarize the statements as follows.

[E4] Under the irradiation light with fixed energy and wavelength, and the injection of electrons in the conduction band, if and only if pairing of B atoms with appropriate separation is realized, DPPs are created and they breed photons.

Since the energy of emitted photon is also less than E_g, it propagate through Si crystal. A part of emitted photons will contribute to create secondary DPPs, but large amount of their energy will dissipate from the Si crystal. As a result, the Joule-heat energy dissipates and it was observed as decrease of the temperature of Si crystal in the annealing process. See Fig. 1.11 of [28]. This cooling effect suppresses diffusive motion of B atoms and fix the pairing structures with suitable separation-number δ. In this way, DPP provides the positive feedback to DPP creation.

[E5] Photon breeding by DPPs guarantees relaxation of spatial distribution of B atoms to the equilibrium distribution in the annealing process. In this relaxation process, B-atom pairs with the suitable separation for creating DPPs are selectively stabilized.

2.2.1.2 Operation of Si-LED with Photon Breeding

In the operation of the fabricated Si-LED, the infrared light is not injected. The forward current is injected, but its value can be much smaller than that injected in the fabrication process. In the fabrication process, it has been required to provide Joule-heat energy by injecting electric current, but in the operation process it is not needed. Kawazoe et al. [29] reported the following.

[E6] The photon energy at the peak of the emitted light spectrum in the operation process was close to $h\nu_{\text{anneal}}$ (see Fig. 2a of [29]). In other words, the photon energy was inherited in the photon breeding.

Kawazoe et al. [29] used linearly polarized infrared light for incident light in the DPP-assisted annealing. Concerning the direction of B-pairs constructed in the fabrication process, the following was verified by experimental measurement.

[E7] The B-atom pairs with specified separation constructed in the fabrication process are parallel to the top surface of the Si crystal (i.e., all pairs are in

the x_1-x_2 planes) for any incident light independently of its polarization state. Moreover, if the irradiation light is linearly polarized, the B-atom pairs are mainly aligned perpendicularly to the polarization direction of the incident light on the x_1-x_2 planes.

By using a linear polarizer, the emitted light was decomposed into two linearly polarized components. Let $P_{\rm h}$ and $P_{\rm v}$ be the intensities of linearly polarized component in the x_1-direction (the horizontal direction) and in the x_2-direction (the vertical direction) of the emitted light, respectively. They measured the degree of polarization,

$$d_{\rm pol} = \frac{P_{\rm h} - P_{\rm v}}{P_{\rm h} + P_{\rm v}}, \tag{2.2}$$

and concluded the following.

[E8] The polarization characteristics of the emitted light from fabricated Si-LED was controlled by the linearly polarized light irradiated during the DPP-assisted annealing.

2.2.2 GaP-LED

Kim et al. [30] studied the GaP LED fabricated by DPP-assisted annealing. Instead of B atoms, they used Zn atoms as dopant in the fabrication. They reported the dependence of the power of emitted light on the value of current I and the power of light incident in the DPP-assisted annealing. They evaluated the numbers of electrons and photons per appropriate units injected in the fabrication processes. They concluded the following.

[E9] When the ratio of the number of injected electrons to the number of irradiated photons is closed to 1, the effect of DPP-assisted annealing was maximized (see Fig. 6 of [30]).

2.3 Stochastic Models on Lattices

Now we introduce a family of stochastic models defined on lattices, each of which is specified by several external and internal parameters. Our theoretical models do not depend on any details of materials, and hence will be applicable both to Si-LED and to GaP-LED. In order to clarify the explanations, however, we will use the Si system with doped B in the following descriptions.

2.3.1 Discrete Setting of Space and Time

Let L be an integer and consider an $L \times L$ square lattice $\Lambda_L = \{1, 2, \ldots, L\}^2$. Each site in Λ_L is specified by the Cartesian coordinates, $\mathbf{x} = (x_1, x_2) \in \Lambda_L$. For any pair of sites $\mathbf{x} = (x_1, x_2) \in \Lambda_L$ and $\mathbf{y} = (y_1, y_2) \in \Lambda_L$, the horizontal distance d_{h} and the vertical distance d_{v} are defined by

$$d_{\mathrm{h}}(\mathbf{x}, \mathbf{y}) = |x_1 - y_1|, \quad d_{\mathrm{v}}(\mathbf{x}, \mathbf{y}) = |x_2 - y_2|, \tag{2.3}$$

respectively. The Euclidean distance d between $\mathbf{x}$ and $\mathbf{y}$ is given by $d(\mathbf{x}, \mathbf{y}) = \sqrt{d_{\mathrm{h}}(\mathbf{x}, \mathbf{y})^2 + d_{\mathrm{v}}(\mathbf{x}, \mathbf{y})^2}$. This square lattice approximates the quasi-2 dim. domain of Si crystal where the concentration of B atoms is maximized in the fabrication by DPP-assisted annealing. See **[E1]** in Sect. 2.2.1.

We will consider the discrete-time stochastic model for the fabrication and the operation of Si-LED assisted by DPP. The time step is denoted by $t \in \{0, 1, 2, 3, \ldots\}$.

2.3.2 Random Walks of B Atoms Induced by I

We consider an interacting system of *random walkers* on Λ_L to simulate the diffusion process of B atoms described in **[E2]** in Sect. 2.2.1. Let N be the total number of B atoms in the lattice, where we assume that N is conserved. In other words, the density of numbers of B atoms in Λ_L, defined by

$$\rho = \frac{N}{L^2} \tag{2.4}$$

is a constant in the present model.

The N particles are labeled by the index $j = 1, 2, \ldots, N$ and the position of the j-th particle is denoted by $\mathbf{x}^{(j)}(t) = (x_1^{(j)}(t), x_2^{(j)}(t)) \in \Lambda_L$ at each time $t \in \{0, 1, 2, \ldots\}$.

In the DPP-assisted annealing, a forward bias voltage was applied to inject the electric current in order to generate Joule heat. It has caused the B atoms to perform diffusion in the Si crystal. If the thermal energy of a B atom is lost, however, it will be trapped at a site in the Si crystal as shown in Fig. 5 of [29] and the diffusive motion is stopped until it gains an enough amount of thermal energy again from the Joule energy of the electric current. In our modeling of such motions of B atoms, we consider two states for each particles, $j = 1, 2, \ldots, N$;

$$\alpha^{(j)} = \begin{cases} + & \text{for the thermally activated state,} \\ - & \text{for the non-activated state.} \end{cases} \tag{2.5}$$

We assume that if and only if $\alpha^{(j)} = +$, the j-th particle has possibility to perform random walk.

We denote the *value of the electric current* by I, which plays an external parameter of the model. Let $\mathbf{e}_{\rm h}$ and $\mathbf{e}_{\rm v}$ be the unit vectors in Λ_L, which are in the horizontal and the vertical directions, respectively; $\mathbf{e}_{\rm h} = (1, 0)$ and $\mathbf{e}_{\rm v} = (0, 1)$. For each time step $t \in \{0, 1, 2, \ldots\}$, if $\alpha^{(j)}(t) = +$,

$$\mathbf{x}^{(j)}(t) \to \begin{cases} \mathbf{x}^{(j)}(t+1) = \mathbf{x}^{(j)}(t) + \mathbf{e}_{\rm h} & \text{with probability } \tanh(c_1 I)/4, \\ \mathbf{x}^{(j)}(t+1) = \mathbf{x}^{(j)}(t) - \mathbf{e}_{\rm h} & \text{with probability } \tanh(c_1 I)/4, \\ \mathbf{x}^{(j)}(t+1) = \mathbf{x}^{(j)}(t) + \mathbf{e}_{\rm v} & \text{with probability } \tanh(c_1 I)/4, \\ \mathbf{x}^{(j)}(t+1) = \mathbf{x}^{(j)}(t) - \mathbf{e}_{\rm v} & \text{with probability } \tanh(c_1 I)/4, \\ \text{and} & \\ \mathbf{x}^{(j)}(t+1) = \mathbf{x}^{(j)}(t) & \text{with probability } 1 - \tanh(c_1 I), \end{cases} \tag{2.6}$$

where $c_1 > 0$ is a fitting parameter. We assume that the particles are *exclusive* in Λ_L and each site can be occupied at most one particle. That is, if the site is already occupied by a particle, any hopping of particle to that site is forbidden. In the model, as a result of transition (2.6), if we have a site with two particles, then that transition (2.6) is canceled and we set $\mathbf{x}^{(j)}(t+1) \equiv \mathbf{x}^{(j)}(t)$. Moreover, the particles located at the boundary sites of Λ_L cannot go outside of the lattice; i.e., we put the *closed boundary condition*.

Note that the hopping is isotropic in the two dimensions and the hopping transition probability is proportional to $\tanh(c_1 I)$. Then, if the electric current is not injected, $I \equiv 0$, then random walk does not occur. The probability to remain at the same site, $1 - \tanh(c_1 I)$, is a decreasing function of $I > 0$ and only in the limit $I \to \infty$, the process (2.6) becomes a simple symmetric (and exclusive) random walk on Λ_L.

2.3.3 *Elementary Processes of Photon Breeding*

2.3.3.1 δ-Pairing of B Atoms

Assume that an N-particle configuration on Λ_L, $\{\mathbf{x}^{(j)}(t)\}_{j=1}^N$, is given at time t. Let δ be a small integer, for instance, $\delta = 3$. For a pair of particles labeled by k and ℓ, if $d_{\rm h}(\mathbf{x}^{(k)}(t), \mathbf{x}^{(\ell)}(t)) = \delta$ or $d_{\rm v}(\mathbf{x}^{(k)}(t), \mathbf{x}^{(\ell)}(t)) = \delta$, we say that these particles make a *horizontal δ-pair* or a *vertical δ-pair*. When we simply say that the particles k and ℓ make a δ-pair, it means that the pair is either horizontal or vertical. For each configuration $\{\mathbf{x}^{(j)}(t)\}_{j=1}^N$, we consider a set of horizontal and vertical δ-pairs,

$$\begin{aligned} A_{\rm h}^{\delta}(t) &= \{(k, \ell) : \text{it makes a horizontal } \delta\text{-pair}\}, \\ A_{\rm v}^{\delta}(t) &= \{(k, \ell) : \text{it makes a vertical } \delta\text{-pair}\}, \quad \text{and} \\ A^{\delta}(t) &= A_{\rm h}^{\delta}(t) \cup A_{\rm v}^{\delta}(t). \end{aligned} \tag{2.7}$$

The numbers of these δ-pairs at time t are denoted as

$$M_{\rm h}^{\delta}(t) = |A_{\rm h}^{\delta}(t)|, \quad M_{\rm v}^{\delta}(t) = |A_{\rm v}^{\delta}(t)|, \quad \text{and}$$
$$M^{\delta}(t) = |A^{\delta}(t)| = M_{\rm h}^{\delta}(t) + M_{\rm v}^{\delta}(t). \tag{2.8}$$

The construction of δ-pairs is interpreted as formation of a local structure. It can create phonons contributing to DPP, if appropriate conditions are satisfied as claimed in **[E4]** in Sect. 2.2.1.

If DPPs are created on the δ-pair, they breed photons. The created photons are emitted from the system, in which the Joule energy is transmitted to the propagating-photon energy and is dissipated from the system. As a result, the B atoms which make the δ-pair lose their thermal energy. Hence we assume that both of the k-th and ℓ-th particles forming a δ-pair (k, ℓ) are inactivated

$$\left.\begin{array}{l} \alpha^{(k)}(t) = + \to \alpha^{(k)}(t+1) = - \\ \alpha^{(\ell)}(t) = + \to \alpha^{(\ell)}(t+1) = - \end{array}\right\} \quad \text{for } (k, \ell) \in A^{\delta}(t). \tag{2.9}$$

That is, random walk of the k-th and ℓ-th particles are stopped and the δ-pair (k, ℓ) is stabilized by photon breeding. In other words, the present interacting random-walk model exhibits an *aggregation process* forming δ-pair structures on a lattice. Remark that soon later we will take into account an aging process of δ-pairs.

2.3.3.2 Creation of Electrons and Photons

For a positive real number a, its integer part is denoted by $[a]$ in this paper. Given $I \geq 0$, we consider a non-negative integer $X \in \{0, 1, 2, \ldots\}$ as follows. If $I = 0$, X is zero, and if $I > 0$, X follows the *Poisson distribution* with the parameter

$$\lambda = [I]. \tag{2.10}$$

That is,

$$\text{if } \ I = 0, \ \ X \equiv 0,$$
$$\text{if } I > 0, \ \ \text{Prob}(X = n) = \frac{\lambda^n}{n!} e^{-\lambda}, \quad n \in \{0, 1, 2, \ldots\}. \tag{2.11}$$

This random integer X will represent the *number of electrons* having a possibility to contribute to create DPPs at a δ-pair.

We introduce another external parameter P^0 in addition to I, which represents the *incident light power*, which is irradiated on the system. It is decomposed into two parts,

$$P^0 = P_{\rm h}^0 + P_{\rm v}^0, \tag{2.12}$$

where $P_{\rm h}^0$ and $P_{\rm v}^0$ give the powers of incident-light components linearly polarized in the horizontal $\mathbf{e}_{\rm h}$ and in the vertical $\mathbf{e}_{\rm v}$ directions, respectively. We denote the polarization angle of incident light with respect to the $\mathbf{e}_{\rm h}$-axis by φ, we have

$$P_{\rm h}^0 = P^0 \cos^2 \varphi, \quad P_{\rm v}^0 = P^0 \sin^2 \varphi. \tag{2.13}$$

In the following, we will define $P_{\rm h}(t)$ and $P_{\rm v}(t)$ inductively at each time t, which represent the *powers of emitted light* from the system having each polarization. On a *horizontal* δ-pair, δ phonons can interact with one photon polarized in the *vertical* direction, and on a *vertical* δ-pair, δ phonons can interact with one photon polarized in the *horizontal* direction. The orthogonality of directions between δ-pairs and photon polarizations is due to the experimental observation **[E7]** given in Sect. 2.2.1. We define

$$p_{\rm h}^{\rm total}(t) = \frac{P_{\rm h}^0}{L^2} + \frac{P_{\rm h}(t)}{M_{\rm v}^\delta(t)}, \quad p_{\rm v}^{\rm total}(t) = \frac{P_{\rm v}^0}{L^2} + \frac{P_{\rm v}(t)}{M_{\rm h}^\delta(t)}. \tag{2.14}$$

With a fitting parameter $c_2 > 0$, we set

$$\mu_{\rm h}(t) = \left[c_2 p_{\rm h}^{\rm total}(t)\right], \quad \mu_{\rm v}(t) = \left[c_2 p_{\rm v}^{\rm total}(t)\right]. \tag{2.15}$$

Then we consider the random variables $Y_{\rm h}$ and $Y_{\rm v}$ as follows;

$$\begin{aligned} &\text{if } p_{\rm h}^{\rm total}(t) = 0, \ \ Y_{\rm h} \equiv 0, \\ &\text{if } p_{\rm h}^{\rm total}(t) > 0, \ \ \mathrm{Prob}(Y_{\rm h} = n) = \frac{\mu_{\rm h}(t)^n}{n!} e^{-\mu_{\rm h}(t)}, \quad n \in \{0, 1, 2, \ldots\} \end{aligned} \tag{2.16}$$

and

$$\begin{aligned} &\text{if } p_{\rm v}^{\rm total}(t) = 0, \ \ Y_{\rm v} \equiv 0, \\ &\text{if } p_{\rm h}^{\rm total}(t) > 0, \ \ \mathrm{Prob}(Y_{\rm v} = n) = \frac{\mu_{\rm v}(t)^n}{n!} e^{-\mu_{\rm v}(t)}, \quad n \in \{0, 1, 2, \ldots\}. \end{aligned} \tag{2.17}$$

The random numbers $Y_{\rm h}$ and $Y_{\rm v}$ will represent the *numbers of photons* operating on a δ-pair, which are linearly polarized in the horizontal direction and in the vertical direction, respectively.

At each time t, we label the δ-pairs by an index $m = 1, 2, \ldots, M(t)$ and denote the m-th pair by $\pi^{(m)}$. For each $\pi^{(m)}$, $m = 1, 2, \ldots, M(t)$, we generate a random integer $X^{(m)}$, which is independently and identically distributed (i.i.d.) with X following (2.11). If $\pi^{(m)} \in A_{\rm v}^\delta(t)$ (resp. $\pi^{(m)} \in A_{\rm h}^\delta(t)$), we also generate a random integer $Y_{\rm h}^{(m)}$ (resp. $Y_{\rm v}^{(m)}$), which is i.i.d. with $Y_{\rm h}$ (resp. $Y_{\rm v}$) following (2.16) (resp. (2.17)). If $X^{(m)} \geq 1$ on the δ-pair $\pi^{(m)}$, one photon will be created additionally by spontaneous emission. Then we put

$$\widetilde{Y}_{\mathrm{h}}^{(m)} = \begin{cases} Y_{\mathrm{h}}^{(m)} + 1, & \text{if } X^{(m)} \geq 1, \\ Y_{\mathrm{h}}^{(m)}, & \text{if } X^{(m)} = 0, \quad \text{for } \pi^{(m)} \in A_{\mathrm{v}}^{\delta}(t), \end{cases}$$

$$\widetilde{Y}_{\mathrm{v}}^{(m)} = \begin{cases} Y_{\mathrm{v}}^{(m)} + 1, & \text{if } X^{(m)} \geq 1, \\ Y_{\mathrm{v}}^{(m)}, & \text{if } X^{(m)} = 0, \quad \text{for } \pi^{(m)} \in A_{\mathrm{h}}^{\delta}(t), \end{cases}$$

where $m = 1, 2, \ldots, M(t)$.

2.3.3.3 Creation of DPPs and Photon Breeding

We assume that each photon interacting with δ phonons on a δ-pair will be able to cooperate with one electron from the injected electric current I to create one DPP. This one-to-one correspondence between photon and electron to create DPP is due to the experimental observation **[E9]** by Kim et al. [30]. Moreover, we assume that this DPP creates one photon, which is polarized in the same direction with the photon making that DPP. If perfect matching between the numbers of electrons and photons are established at a δ-pair, say, $X^{(m)} = \widetilde{Y}_{*}^{(m)} \equiv k \geq 1$ ($* =$ h or v), k photons can be created. But if $X^{(m)} \neq \widetilde{Y}_{*}^{(m)}$ ($* =$ h or v), the number of created photons can be only $\min\{X^{(m)}, \widetilde{Y}_{*}^{(m)}\}$. We set

$$Z_{*}^{(m)}(t) = \min\{X^{(m)}, \widetilde{Y}_{*}^{(m)}\}, \quad * = \text{h or v}, \quad m = 1, 2, \ldots, M(t). \tag{2.18}$$

That is, the number of created photons at a δ-pair, $Z_{*}^{(m)}(t)$, $* =$ h or v, is determined by *coupled Poisson processes* of $X^{(m)}$ and $\widetilde{Y}_{*}^{(m)}$.

For $m = 1, 2, \ldots, M(t)$, the excess of electrons or photons is defined by

$$\begin{aligned} \Delta_{\mathrm{v}}^{(m)}(t) &= |X^{(m)} - Y_{\mathrm{h}}^{(m)}|, \quad \text{if } \pi^{(m)} \in A_{\mathrm{v}}^{\delta}(t), \\ \Delta_{\mathrm{h}}^{(m)}(t) &= |X^{(m)} - Y_{\mathrm{v}}^{(m)}|, \quad \text{if } \pi^{(m)} \in A_{\mathrm{h}}^{\delta}(t). \end{aligned} \tag{2.19}$$

Then we define the powers of emitted light at time $t + 1$ as the summations over δ-pairs of the numbers of created photons,

$$\begin{aligned} P_{\mathrm{h}}(t+1) &= \sum_{m:\pi^{(m)} \in A_{\mathrm{v}}^{\delta}(t)} Z_{\mathrm{h}}^{(m)}(t), \\ P_{\mathrm{v}}(t+1) &= \sum_{m:\pi^{(m)} \in A_{\mathrm{h}}^{\delta}(t)} Z_{\mathrm{v}}^{(m)}(t). \end{aligned} \tag{2.20}$$

Through the formulas (2.14) and (2.15) with replacing t by $t + 1$, we determine the values of parameters of Poisson distributions used to generate the random variables Y_h and Y_v representing the number of stimulated photons with each polarization at time $t + 1$. Here we emphasize the point that the parameters $\mu_{\mathrm{h}}(t)$ and $\mu_{\mathrm{v}}(t)$ for the Poisson processes Y_{h} and Y_{v} are time dependent random variables.

2.3.4 Aging of δ-Pairs and Re-activation of B Atoms by Excess Heat

As time step is passing $t = 1, 2, 3, \ldots$, the processes explained above are repeated. Among these iterations, at each δ-pair of B atoms $\pi^{(m)}$, the excesses of electrons or photons $\Delta_*^{(m)}$ defined by (2.19) are accumulated. The energy of excess electrons and photons cannot be transmitted to creation energy of photons. It will be gradually transmitted into thermal energy and used to heat up the δ-pair. In this sense, the accumulation of $\Delta_*^{(m)}$ in time will measure an *aging effect* of the δ-pair $\pi^{(m)}$. We introduce a parameter describing a threshold, $c_3 > 0$. Assume that a δ-pair was formed at time T_1 by the k-th particle and the ℓ-th particle, $\pi^{(m)} = (k, \ell)$, and then

$$T_2 = \min\left\{ s : s > T_1, \sum_{t=T_1}^{s} \Delta_*^{(m)}(t) > c_3 \right\}. \tag{2.21}$$

At time $t = T_2$, when the accumulated value of excesses exceeds c_3, we think that both of the k-th particle and the ℓ-th particle are thermally re-activated;

$$\left.\begin{array}{l} \alpha^{(k)}(T_2) = - \to \alpha^{(k)}(T_2 + 1) = + \\ \alpha^{(\ell)}(T_2) = - \to \alpha^{(\ell)}(T_2 + 1) = + \end{array}\right\} \text{ for the aged } \delta\text{-pair } (k, \ell). \tag{2.22}$$

The time deference $T_2 - T_1$ gives lifetime of the δ-pair, $\pi^{(m)} = (k, \ell)$. Since the times T_1 and T_2 are random variables, the lifetimes are also distributed.

2.4 Simulation for Fabrication and Operation of Si-LED

2.4.1 Four Regimes of Simulated Processes

We set

$$\begin{aligned} &L = 200, \\ &\rho = 0.01 \quad \Longleftrightarrow \quad N = 400. \end{aligned} \tag{2.23}$$

The initial configuration of particles representing B atoms, $\{\mathbf{x}^{(j)}\}_{j=1}^{N}$ is chosen at random; the particle positions are uniformly distributed on the lattice Λ_L without any multiple points: $\mathbf{x}^{(j)} \neq \mathbf{x}^{(k)}$, if $j \neq k$. We assume that all particles are thermally activated at time $t = 0$,

$$\alpha^{(j)}(0) = + \quad \text{for all } j = 1, 2, \ldots, N. \tag{2.24}$$

Here we set the parameters as

$$\begin{aligned} c_1 &= c_2 = 1, \\ c_3 &= 6000. \end{aligned} \tag{2.25}$$

The most important setting of parameters is concerning the current I and the incident light power $P^0 = P^0_{\mathrm{h}} + P^0_{\mathrm{v}}$. First we consider the simple case such that the horizontal and the vertical components of P^0 are the same,

$$P^0_{\mathrm{h}} = P^0_{\mathrm{v}} = \frac{P^0}{2}. \tag{2.26}$$

In other words, the polarization angle of incident light is set as

$$\varphi = \frac{\pi}{4} \tag{2.27}$$

and thus

$$P^0_{\mathrm{v}} = P^0 \cos^2 \frac{\pi}{4} = \frac{P^0}{2}, \quad P^0_{\mathrm{h}} = P^0 \sin^2 \frac{\pi}{4} = \frac{P^0}{2}. \tag{2.28}$$

We introduce a special time t_0 in our simulation. We set

$$I(t) = \begin{cases} I = \text{const.} & \text{for } 0 \le t < t_0, \\ \dfrac{I}{10} = \text{const.} & \text{for } t \ge t_0, \end{cases} \tag{2.29}$$

and

$$P^0(t) = \begin{cases} P^0 = \text{const.} & \text{for } 0 \le t < t_0, \\ 0 = \text{const.} & \text{for } t \ge t_0. \end{cases} \tag{2.30}$$

In the time period $0 \le t < t_0$, we simulate the *fabrication process*. There enough amount of current I is injected and incident light has positive power $P^0 > 0$ to realize the DPP-assisted annealing. When $t = t_0$, we stop the fabrication process and start to operate the system as an LED. In this *operation process* $t \ge t_0$, we stop irradiation of light, $P^0 \equiv 0$. The value of current for the operation process should be much smaller than that for annealing. Here we assume that the current injected in the operation process is only 1/10 of the current injected in the fabrication process as given by (2.29), since the current is used only for providing electrons to create DPPs into the system in the operation process. (Remark that we will consider different situations by changing this 1/10-factor in Sects. 2.5.2 and 2.6.2.) Moreover, we assume in our simulation that when we stop the fabrication process, the accumulation in time of excess electrons and photons is canceled at any δ-pair;

$$\Delta^{(m)}_{*}(t_0) = 0, \quad * = \mathrm{h} \text{ or } \mathrm{v}, \quad m = 1, 2, \ldots, M(t_0). \tag{2.31}$$

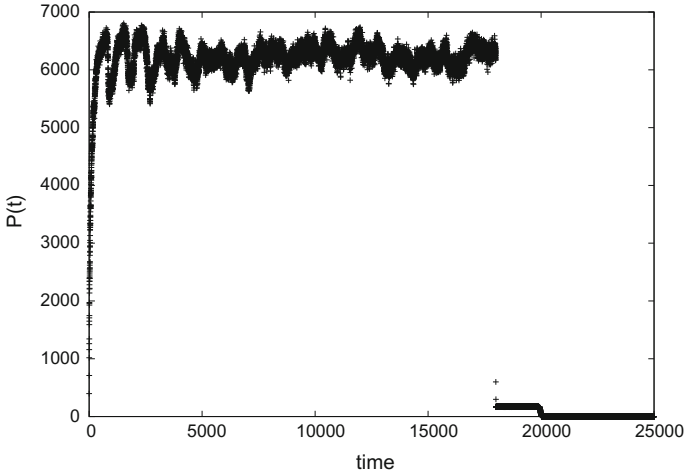

Fig. 2.3 Typical output of the power $P(t)$ of photon emission from the system. The time period $0 \leq t < t_0 = 18000$ simulates the fabrication process, and the time period $t \geq t_0$ does the operation process. Even though there is no incident light $P^0 \equiv 0$ for $t \geq t_0$, we have spontaneous emission of light $P(t) > 0$ up to time $t_{\rm stop} = 20056$

We calculate the total power of photon emission

$$P(t) = P_{\rm h}(t) + P_{\rm v}(t) \tag{2.32}$$

both for the fabrication period $0 \leq t < t_0$ and the operation period $t \geq t_0$. Figure 2.3 shows a typical output of our simulation in the case that

$$\begin{aligned} &I = 40, \quad P^0 = 80, \\ &t_0 = 18000. \end{aligned} \tag{2.33}$$

We find the following four regimes.

2.4.1.1 Transient Regime of Fabrication Process

At beginning $P(t)$ increases very rapidly. Then it shows oscillatory behavior. We find a relaxation phenomenon such that the amplitude of oscillation decreases in time as shown in Fig. 2.4.

2.4.1.2 Equilibrium Regime of Fabrication Process

In Fig. 2.3, the system arrives at the equilibrium state at time $t = t_{\rm eq} \simeq 8000$. For $t_{\rm eq} \leq t \leq t_0$, $P(t)$ shows a relatively small equilibrium fluctuation around its mean

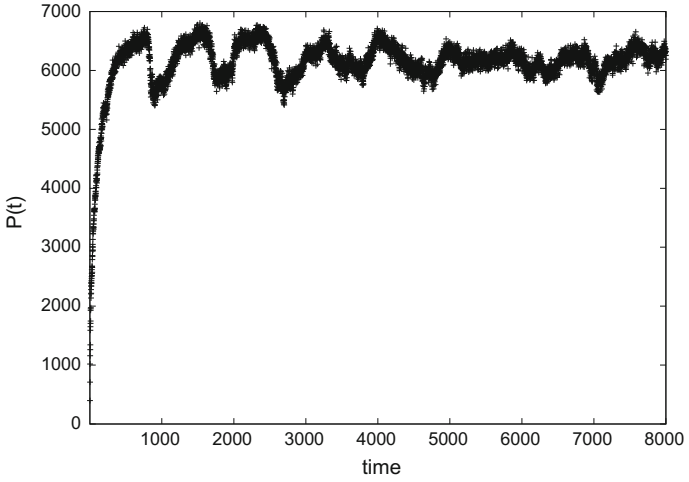

Fig. 2.4 Time evolution of $P(t)$ in the transient regime of fabrication process. A relaxation to the equilibrium state is observed; the amplitude of oscillation decreases and tends to show steady fluctuation around the equilibrium value $\overline{P}^{\mathrm{fab}} = 6247$

value calculated by

$$\overline{P}^{\mathrm{fab}} = \frac{1}{t_0 - t_{\mathrm{eq}}} \int_{t_{\mathrm{eq}}}^{t_0} P(t)dt. \tag{2.34}$$

Fig. 2.3 gives the value $\overline{P}^{\mathrm{fab}} = 6247$.

2.4.1.3 Stable Operation Regime

After t_0, the value of $P(t)$ becomes much smaller than $\overline{P}^{\mathrm{fab}}$, since we have reduced the value of current to 1/10 following (2.29). We emphasize the importance, however, that even though we set $P^0 \equiv 0$ for $t \geq t_0$, $P(t) > 0$, as shown by Fig. 2.5. That is, the system works as an LED, in which the electric-current energy is transmitted into light-emission energy. In Fig. 2.5, after $t = t_{\mathrm{det}} \simeq 19900$, $P(t)$ deceases very rapidly. The average power of the LED is defined as

$$\overline{P}^{\mathrm{op}} = \frac{1}{t_{\mathrm{det}} - t_0} \int_{t_0}^{t_{\mathrm{det}}} P(t)dt. \tag{2.35}$$

Fig. 2.5 gives the value $\overline{P}^{\mathrm{op}} = 169$.

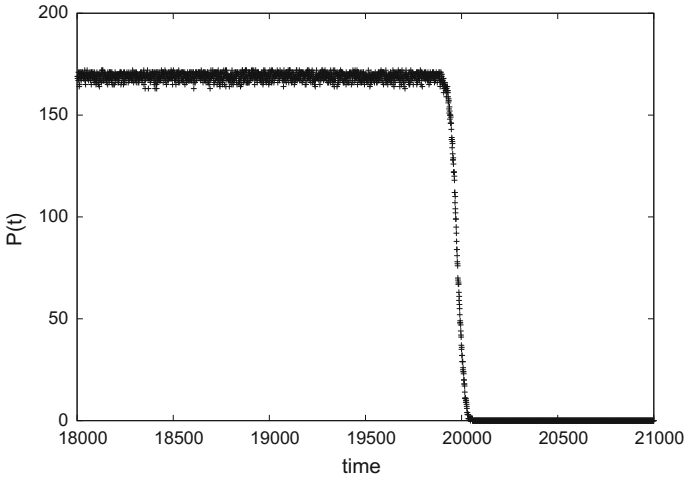

Fig. 2.5 Time dependence of the spontaneous emission of light $P(t)$ in the operation process, $t \geq t_0 = 18000$. At $t = t_{\rm det} \simeq 19900$, the emission power $P(t)$ starts to decrease. The deterioration process is very rapid and $P(t)$ becomes zero at $t = t_{\rm stop} = 20056$. The lifetime of system as an LED is $\tau = t_{\rm stop} - t_0 = 2056$

2.4.1.4 Deterioration Regime

In Fig. 2.5, $P(t)$ becomes zero at $t = t_{\rm stop} = 20056$ Since accumulation of excess energy of electrons and photons heats the δ-pairs and violates them, and hence DPP creation is suppressed. System has a lifetime

$$\tau = t_{\rm stop} - t_0, \tag{2.36}$$

as an LED. For this system, the lifetime as an LED is $\tau = 2056$ time steps.

We have studied these four regimes in detail as explained below.

2.4.2 Cooling of System in Transient Regime of Fabrication Process

Since we have started the simulation from the state that all B atoms are thermally activated as (2.24), they perform random walks and δ-pairs are randomly formulated. In the present setting of external parameters, $I = P_{\rm h}^0 = P_{\rm v}^0 = 40$, DPPs are effectively created and the thermal energy given to random walkers is transmitted into light-emission energy. Then δ-pairs are stabilized by inactivation of B atoms forming them, $\alpha^{(j)} = + \to -$. Figure 2.6 shows the time dependence of the number of δ-pairs up to time $t_{\rm eq} \simeq 8000$. The relaxation seems to be very rapid and the number of δ-pairs shows equilibrium fluctuation after $t \simeq 5000$.

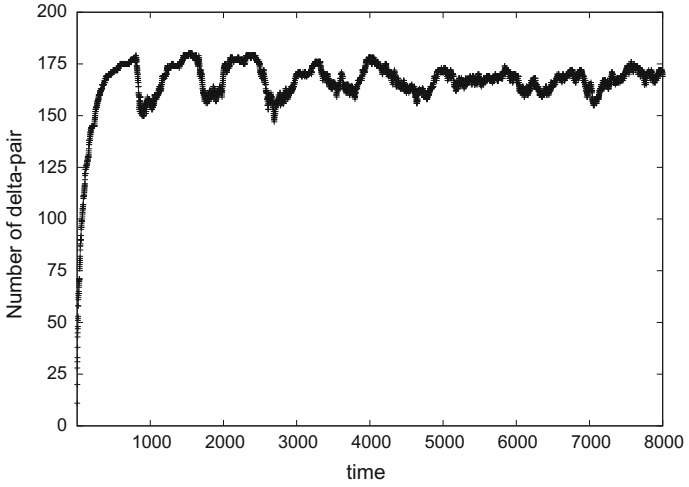

Fig. 2.6 Time dependence of the number of δ-pairs in fabrication process. The relaxation is rapid and equilibrium fluctuation is observed after $t \simeq 5000$

The random walkers have been thermally inactivated. The thermal inactivation will be observed as decrease of temperature of the LED surface. We plot the time dependence of the ratio of the number of particles which are still thermally activated to the total number N,

$$r^+(t) = \frac{1}{N}\Big|\{1 \le j \le N : \alpha^{(j)} = +\}\Big|, \tag{2.37}$$

in Fig. 2.7. It shows a rapid decrease from the initial value $r^+(0) = 1$ and then show fluctuation around its equilibrium value

$$\overline{r}^+ = \frac{1}{t_0 - t_{\rm eq}} \int_{t_{\rm eq}}^{t_0} r^+(t)dt. \tag{2.38}$$

In the present case shown by Fig. 2.7, $\overline{r}^+ = 0.156$. We think that the quantity (2.37) will simulate the temperature of the LED surface and it can be compared with the experimental measurement reported in Fig. 1.11 of [28].

2.4.3 Construction of δ-Pair Network in Equilibrium Regime of Fabrication Process

In the equilibrium regime of the fabrication process, we obtain a stationary configuration of δ-pairs. Figure 2.8 shows a snapshot of particle configuration $\{\mathbf{x}^{(j)}(t)\}_{j=1}^N$

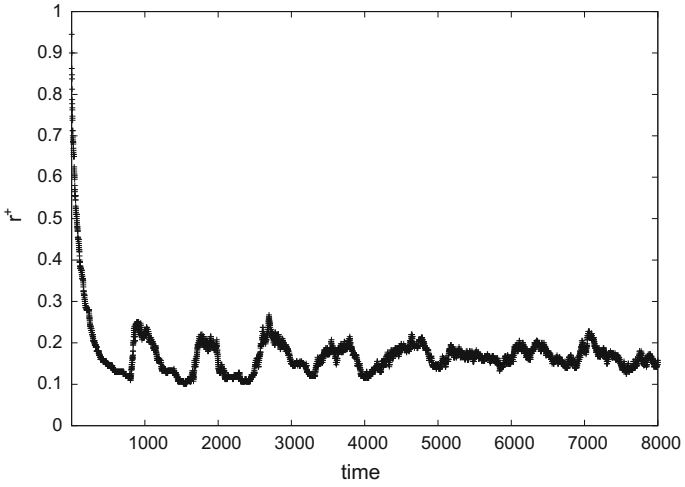

Fig. 2.7 Time dependence of the ratio $r^+(t)$ of the number of activated particles to the total number N. This quantity simulates the temperature of the LED surface

at time $t = 8697$. Here the thermally activated particles ($\alpha^{(j)} = +$) are expressed by red dots and the inactivated particles ($\alpha^{(j)} = -$) are by black dots. The δ-pairs are marked by green line-segments connecting two inactivated particles. The numbers of horizontal and vertical δ-pairs in this figure are $M^{\delta}_{\rm h}(8697) = 88$ and $M^{\delta}_{\rm v}(8697) = 83$ and the total number is $M^{\delta}(8697) = 171$.

Since the concentration of B atoms is low as $\rho = 0.01$, the distribution of δ-pairs are spatially sparse (see the experimental result **[E1]** in Sect. 2.2.1). As a matter of fact, the total number of δ-pairs on this typical configuration given by Fig. 2.8, $M^{\delta}(8697) = 171$, is almost the same as the value $N(1 - \overline{r}^{+})/2 = 400 \times (1 - 0.156)/2 = 168.8$. The emitted photons from each δ-pair are propagating whole in the present plane lattice Λ_L and are shared by all δ-pairs (see **[E3]** in Sect. 2.2.1). In our model, the factors $P_{\rm h}(t)/M^{\delta}_{\rm v}(t)$ and $P_{\rm v}(t)/M^{\delta}_{\rm h}(t)$ in (2.14) show that the creation of the photons at individual δ-pair are enhanced by (each polarized) photons propagating from other δ-pairs. In this sense, the sparse δ-pairs are considered to construct an effective network for photon breeding on the lattice.

It should be noted that the particle configuration is changing in time even in the equilibrium regime of fabrication process. Equilibrium configuration is stationary in the sense that the distribution of configurations becomes temporally independent. Also in the equilibrium regime, excesses of electrons and photons in producing DPP are accumulated in time at each δ-pair and when the accumulated value becomes larger than the threshold value c_3, the δ-pair becomes unstable. The energy of excess electrons and photons which cannot be transmitted to photon emission will become thermal energy and it activates the particles making that δ-pair. The activation allows them to perform random walks again and the δ-pair structure will be violated. Although the random walk of particle violates δ-pairs, however, it also gives

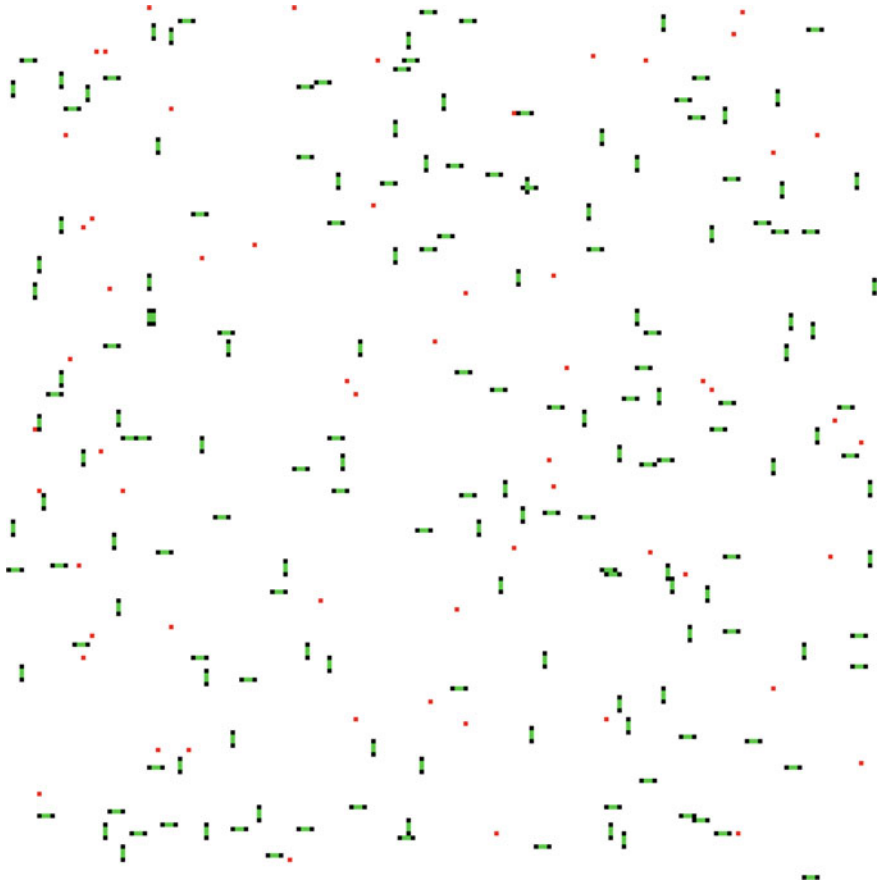

Fig. 2.8 Snapshot of the particle configuration at time $t = 8697$. Here the thermally activated particles are expressed by *red dots* and the inactivated particles are by *black dots*. The δ-pairs are marked by *green line-segments* connecting two inactivated particles. The numbers of horizontal and vertical δ-pairs in this figure are $M_{\mathrm{h}}^{\delta}(8697) = 88$ and $M_{\mathrm{v}}^{\delta}(8697) = 83$ and the total number is $M^{\delta}(8697) = 171$

possibility to make other δ-pairs and these newly formed δ-pair can start breeding photons by setting $\Delta_{*}^{(m')} = 0$ ($* = \mathrm{h}$ and v). Figure 2.9 shows the time dependence of the values of accumulated excesses summed over δ-pairs,

$$\Delta(t) = \sum_{m:\pi^{(m)} \in A_{\mathrm{h}}^{\delta}} \Delta_{\mathrm{h}}^{(m)}(t) + \sum_{m:\pi^{(m)} \in A_{\mathrm{v}}^{\delta}} \Delta_{\mathrm{v}}^{(m)}(t). \tag{2.39}$$

It shows oscillatory behavior in the transient regime and then relaxes to the stationary value in the equilibrium regime. The stationary value 3003 is about half of the parameter $c_3 = 6000$. In this way the δ-pair network is dynamically maintained in the equilibrium regime.

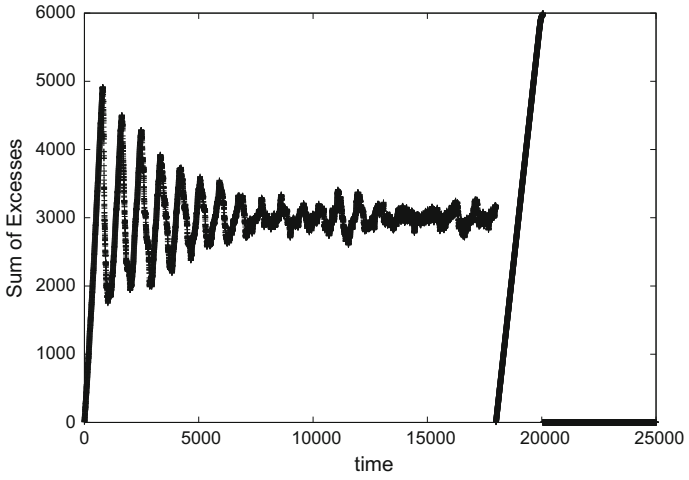

Fig. 2.9 Time dependence of the summation of excesses over δ-pairs. In the equilibrium regime of fabrication, $t_{\rm eq} \simeq 8000 \leq t \leq t_0 = 18000$, $\Delta(t)$ shows relatively small fluctuation around the equilibrium value $3003 \simeq c_3/2$. In the operation regime, $t \geq t_0 = 18000$, $\Delta(t)$ increases monotonically due to the unbalance between $P^0 \equiv 0$ and $I > 0$, and then all δ-pairs are broken at $t = t_{\rm stop} = 20056$

2.4.4 Accumulation of Excess Energy in Operation Process

After $t_0 = 18000$, we set $P^0 \equiv 0$, and thus there occurs no more emission of light stimulated by incident light. We inject current, which is only 1/10 of the current injected for the DPP-assisted annealing. By this weak current, however, spontaneous emission of light can occur. The important fact is that the δ-pair network has been already established at $t = t_0$. Therefore, once photons are created at δ-pairs, these photons interact with electrons injected by current and with phonons created at δ-pairs, and they create DPPs, which perform photon breeding. As shown in Fig. 2.5, the present model realizes such a spontaneous phenomenon and keeps $P(t) > 0$ in the time period $t_0 = 18000 < t < t_{\rm stop} = 20056$.

In this operation regime in the present model, the number of electrons and photons created at each δ-pair are distributed according to the Poisson distributions. Hence the excesses of them $\Delta_*^{(m)}$ emerge randomly and are accumulated in time. When $\sum_t \Delta_*^{(m)}(t) > c_3$, the particle forming the δ-pair becomes thermally re-activated and have a positive probability to re-start random walks. In the operation regime, the injected current is weak and hence random walk is very 'slow'. (Precisely speaking, the probability to remain at the same site, $1 - \tanh(c_1 I)$, takes a large value, see (2.6).) Then once the δ-pair is broken by random walk, the probability of reconstruction of another δ-pair will be very small, since the δ-pair distribution is sparse on the lattice. As a result, $\Delta(t)$ defined by (2.39) increases monotonically in the operation process $t \geq t_0$ as shown in Fig. 2.9 and the system is broken as an LED at time $t = t_{\rm stop} = 20056$.

2.5 Optimization of DPP-Assisted Annealing by Ratio $P_0/2I$

As given by the formula (2.11) with (2.10) and the formulas (2.16) and (2.17) with (2.13)–(2.15), the mean numbers of electrons X and photons Y_h and Y_v created at each δ-pair are approximately proportional to the values I and P^0. As discussed in Sects. 2.3.4, 2.4.3, and 2.4.4, the excesses defined by (2.19) will violate δ-pair structures and reduce the efficiency of DPP creation. We expect hence that the efficiency of DPP-assisted annealing to produce Si-LED is maximized when

$$I = P_\mathrm{h}^0 = P_\mathrm{v}^0 = \frac{1}{2}P^0, \tag{2.40}$$

since we have set $c_2 = 1$ in (2.15). In other words, the experimental result **[E9]** will be realized in the present model. In order to verify it, we have performed simulations by changing the values of I and P^0 keeping the relation

$$I + P_\mathrm{h}^0 = I + P_\mathrm{v}^0 = c_4 \tag{2.41}$$

with $c_4 = 80$.

2.5.1 Mean Emission Powers Versus $P^0/2I$

Figure 2.10 shows the mean values of emitted light powers in the equilibrium regime of fabrication process, $\overline{P}^{\mathrm{fab}}$, defined by (2.34) for various values of the ratio $P^0/2I$. Figure 2.11 shows the plots of $\overline{P}^{\mathrm{op}}$ calculated by (2.35) in the operation regimes versus $P^0/2I$.

As expected, both attains maxima at $P^0/2I = 1$. This result is consistent with **[E9]**; Fig. 2.10 should be compared with Fig. 6 of [30]. Precisely speaking, the experimental result shows that the maximum is attained when $P^0/2I \simeq 1.3$ in our parameterization, but this disagreement will be adjusted by choosing the parameter c_2 appropriately. More interesting thing is the asymmetry of the curves in these figures around the peaks, found both in the experimental results and in the present simulations. This asymmetry will be due to the fact that the electric current I is used not only to provide electrons in conduction band to formulate DPPs, but also to give Joule heat in the DPP-assisted annealing.

2.5.2 Lifetime of LED

Figure 2.12 shows the lifetime τ defined by (2.36) versus $P^0/2I$ in the operation processes. The life time seems to be monotonically increasing with the ratio $P^0/2I$.

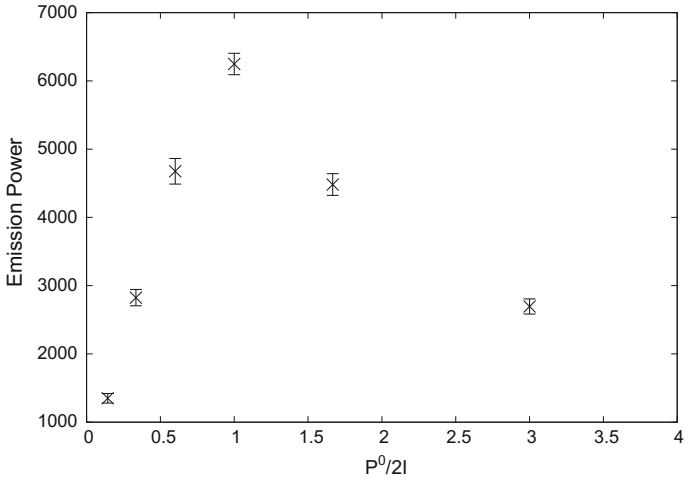

Fig. 2.10 Mean power of emitted light in the fabrication process $\overline{P}^{\mathrm{fab}}$ versus $P^0/2I$. Maximum is attained when (2.40) is satisfied as expected

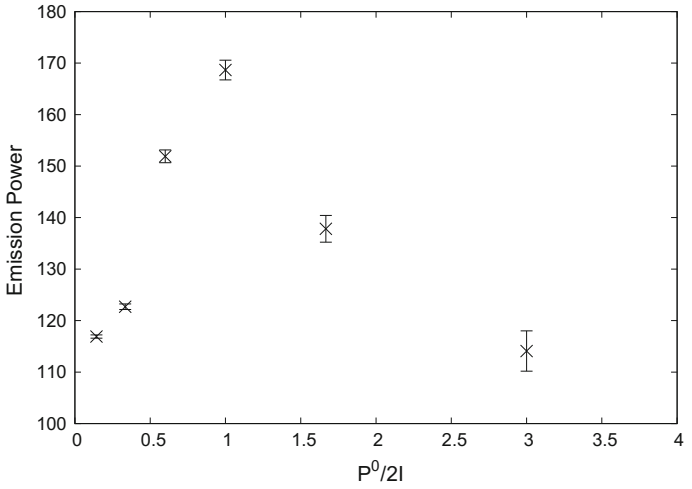

Fig. 2.11 Mean power of emitted light in the operation process $\overline{P}^{\mathrm{op}}$ versus $P^0/2I$. Maximum is attained when (2.40) is satisfied as expected

This result implies that if we use the present LED with smaller current, the LED will work longer. Here we introduce a parameter $0 < c_5 \leq 1$ and replace (2.29) by

$$I(t) = \begin{cases} I = \text{const.} & \text{for } 0 \leq t < t_0, \\ c_5 I = \text{const.} & \text{for } t \geq t_0. \end{cases} \tag{2.42}$$

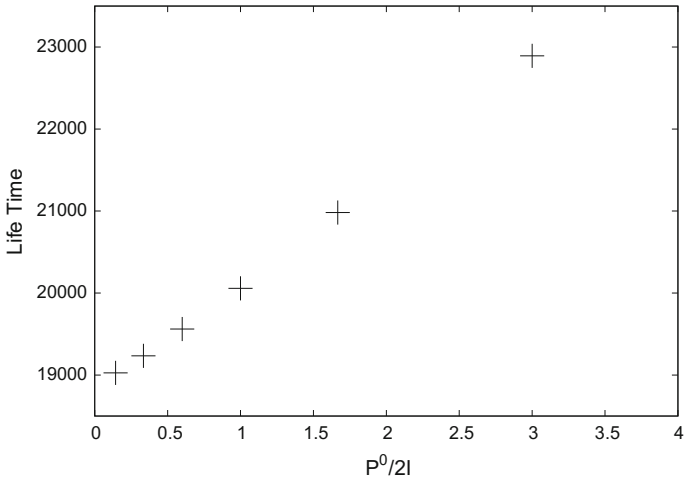

Fig. 2.12 Lifetime τ of LED in operation processes versus $P^0/2I$

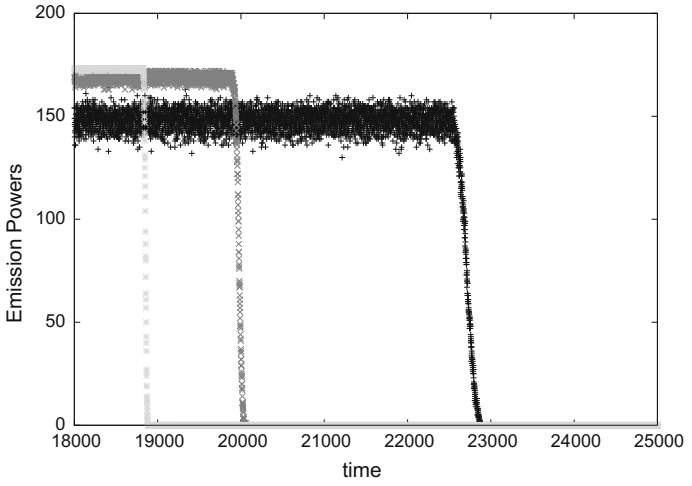

Fig. 2.13 Dependence on the reduction rate c_5 of the spontaneous emission of light in the operation process, $P(t), t \geq t_0$. Plots are given for $c_5 = 1/5$ (*light gray*), $c_5 = 1/10$ (*dark gray*), and $c_5 = 1/20$ (*black*), respectively

The fabrication process is completely the same as that reported in Sect. 2.4. Only the reduction rate of injected current in the operation process compared to the value in the fabrication process is changed. Figure 2.13 shows the dependence on the reduction rate c_5 of the spontaneous emission of light in the operation processes, $P(t), t \geq t_0$. Compared with the case $c_5 = 1/10$, in which $\tau = 2056$, the lifetime becomes shorter

as $\tau = 881$ for larger $c_5 = 1/5$, while it becomes longer as $\tau = 4869$ for smaller $c_5 = 1/20$. Note that the emission power decreases, however, as τ becomes longer.

We will discuss the present results on τ in comparison with the experimental results in Sect. 2.8.

2.6 Light Polarization Controlled in Photon Breeding

In this section, we will report the fact that our model can simulate the important property of photon breeding assisted by DPP given as **[E8]** in Sect. 2.2.1. In Sect. 2.4 we considered the case $\varphi = \pi/4$, in which $P_{\rm h}^0 = P_{\rm v}^0$ for the incident light components. Here we consider the other cases with $\varphi = 0, \pi/2$ and $\pi/6$.

2.6.1 The Cases $\varphi = 0$ and $\pi/2$

When $\varphi = 0$ and $\pi/2$, the incident light is linearly polarized in the horizontal direction, $(P_{\rm h}^0, P_{\rm v}^0) = (P^0, 0)$, and in the vertical direction, $(P_{\rm h}^0, P_{\rm v}^0) = (0, P^0)$, respectively. Figures 2.14 and 2.15 show the configurations of δ-pairs at the time $t = t_0 = 18000$, when the fabrication process is completed, for the cases $\varphi = 0$ and $\varphi = \pi/2$, respectively.

The directions of δ-pairs are allied in the vertical direction in the former case and in the horizontal direction in the latter case, respectively. The orthogonality of directions between the polarization of irradiation light and δ-pairs is due to our setting to realize the experimental fact **[E7]**. In this way, the polarization of incident light is memorized as the direction of δ-pairs of B atoms in the DPP-assisted annealing. As a matter of course, the emitted light has the same polarization as the incident light both in the fabrication processes and the operation processes in our simulation, when $\varphi = 0$ or $\varphi = \pi/2$.

2.6.2 The Case $\varphi = \pi/6$

Next we study the case that

$$\begin{aligned} &\varphi = \frac{\pi}{6} \\ \Longleftrightarrow\ & P_{\rm h}^0 = P^0 \cos^2 \frac{\pi}{6} = \frac{3}{4} P^0, \quad P_{\rm v}^0 = P^0 \sin^2 \frac{\pi}{6} = \frac{1}{4} P^0. \end{aligned} \tag{2.43}$$

Since we have set $P^0 = 80$, $P_{\rm h}^0 = 60$ and $P_{\rm v}^0 = 20$ in the present simulation. Instead of (2.29) with $I = 40$, here we assume the time dependence of the injection current

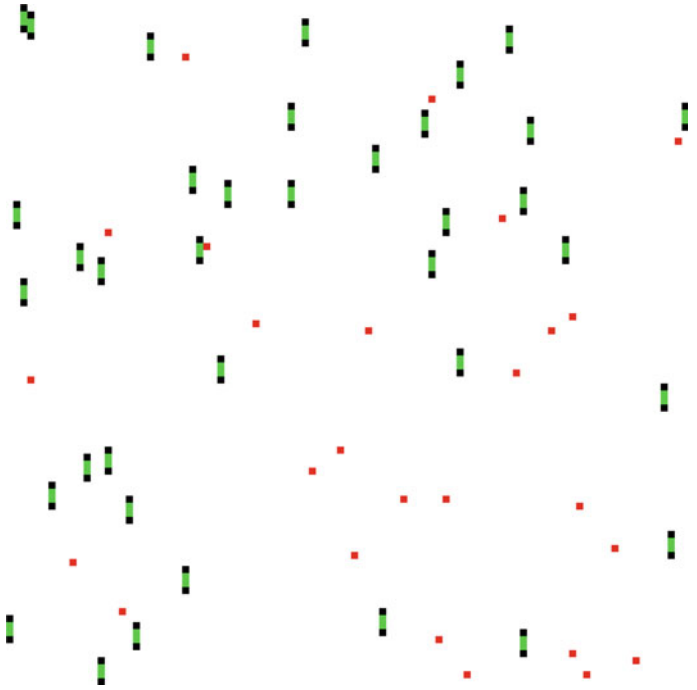

Fig. 2.14 Particle configuration (size 100×100) at time $t = t_0$ in the case $\varphi = 0$ (i.e., the incident light is polarized horizontally). The δ-pairs are marked by *green line-segments* connecting two inactivated particles. All δ-pairs are aligned in the vertical direction

as

$$I(t) = \begin{cases} 60 & \text{for } 0 \le t < t_0, \\ 4 & \text{for } t \ge t_0. \end{cases} \tag{2.44}$$

Figure 2.16 shows the time evolution of the powers of emitted light polarized in the horizontal direction $P_{\mathrm{h}}(t)$ and in the vertical direction $P_{\mathrm{v}}(t)$ as well as their sum $P(t) = P_{\mathrm{h}}(t) + P_{\mathrm{v}}(t)$. The results for the operation regimes $t \ge t_0$ are magnified in Fig. 2.17.

We define

$$\begin{aligned} \overline{P}_{*}^{\mathrm{fab}} &= \frac{1}{t_0 - t_{\mathrm{eq}}} \int_{t_{\mathrm{eq}}}^{t_0} P_{*}(t)dt, \\ \overline{P}_{*}^{\mathrm{op}} &= \frac{1}{t_{\mathrm{det}} - t_0} \int_{t_0}^{t_{\mathrm{det}}} P_{*}(t)dt, \quad \text{for } *=\mathrm{h} \text{ and } \mathrm{v}. \end{aligned} \tag{2.45}$$

The simulation results shown by Fig. 2.16 give the values, $\overline{P}_{\mathrm{h}}^{\mathrm{fab}} = 7057$, $\overline{P}_{\mathrm{v}}^{\mathrm{fab}} = 628$, $\overline{P}_{\mathrm{h}}^{\mathrm{op}} = 121$, $\overline{P}_{\mathrm{v}}^{\mathrm{op}} = 29$, and hence we have the ratios as

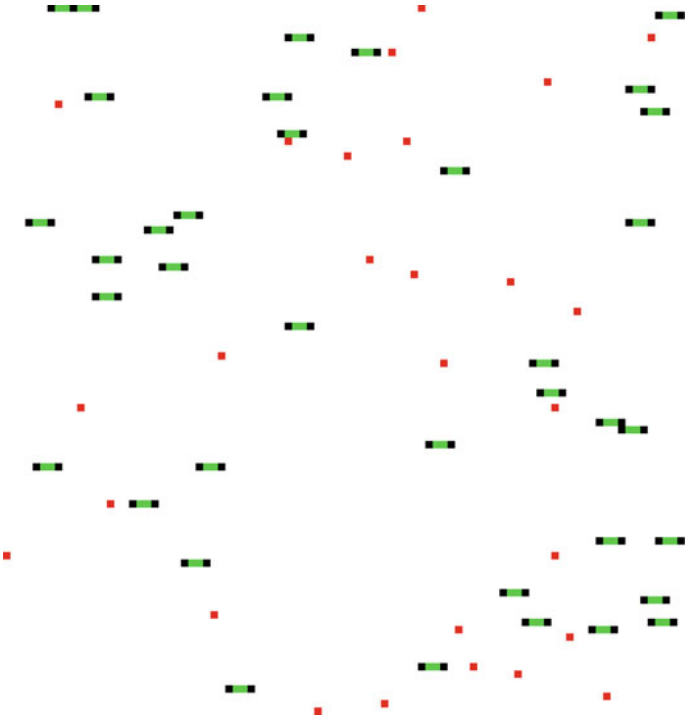

Fig. 2.15 Particle configuration (size 100×100) at time $t = t_0$ in the case $\varphi = \pi/2$ (i.e., the incident light is polarized vertically). The δ-pairs are marked by *green line-segments* connecting two inactivated particles. All δ-pairs are aligned in the horizontal direction

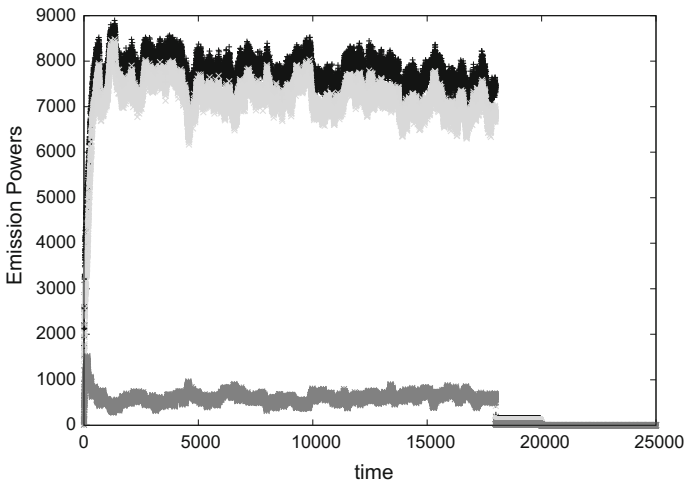

Fig. 2.16 Total power $P(t)$ (*black dots*) and its horizontal component $P_{\rm h}(t)$ (*light gray dots*) and vertical component $P_{\rm v}(t)$ (*dark gray dots*) of emitted light in the case $\varphi = \pi/6$

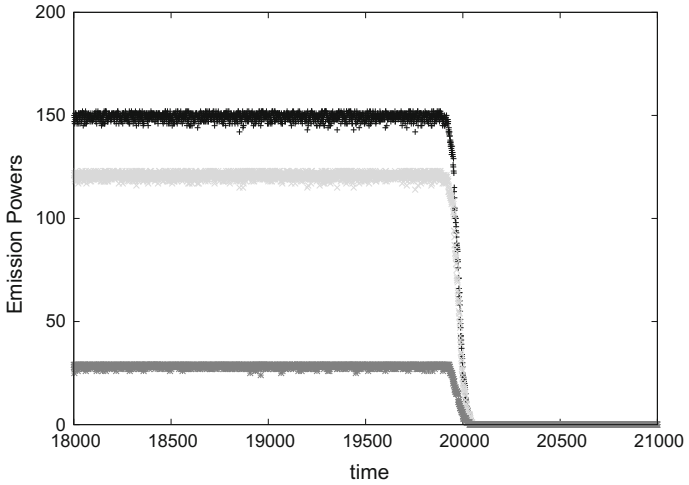

Fig. 2.17 Total power $P(t)$ (*black dots*) and its horizontal component $P_{\rm h}(t)$ (*light gray dots*) and vertical component $P_{\rm v}(t)$ (*dark gray dots*) of emitted light in the case $\varphi = \pi/6$ shown for the operation regimes

$$\frac{P_{\rm v}^0}{P_{\rm h}^0} = \frac{1}{3} \quad \Longrightarrow \quad \frac{\overline{P}_{\rm v}^{\rm fab}}{\overline{P}_{\rm h}^{\rm fab}} = 0.089, \quad \frac{\overline{P}_{\rm v}^{\rm op}}{\overline{P}_{\rm h}^{\rm op}} = 0.24. \tag{2.46}$$

If we define the polarization angles by

$$\overline{\varphi}^{\rm fab} = \tan^{-1}\sqrt{\frac{\overline{P}_{\rm v}^{\rm fab}}{\overline{P}_{\rm h}^{\rm fab}}}, \quad \overline{\varphi}^{\rm op} = \tan^{-1}\sqrt{\frac{\overline{P}_{\rm v}^{\rm op}}{\overline{P}_{\rm h}^{\rm op}}}, \tag{2.47}$$

the above results (2.46) give

$$\varphi = \frac{\pi}{6} \simeq 0.524 \quad \Longrightarrow \quad \overline{\varphi}^{\rm fab} = 0.290, \quad \overline{\varphi}^{\rm op} = 0.455. \tag{2.48}$$

That is, the polarization angle φ of light is modified in the photon breeding.

Figure 2.18 shows the configuration of δ-pairs at $t = t_0 = 18000$ when the fabrication is completed. We see $M_{\rm h}^{\delta}(t_0) = 29$ and $M_{\rm v}^{\delta}(t_0) = 152$, which gives

$$\left(\frac{M_{\rm v}^{\delta}(t_0)}{M_{\rm h}^{\delta}(t_0)}\right)^{-1} = 0.19. \tag{2.49}$$

If we define the 'canting angle' of δ-pairs $\varphi_{\rm pair}$ by

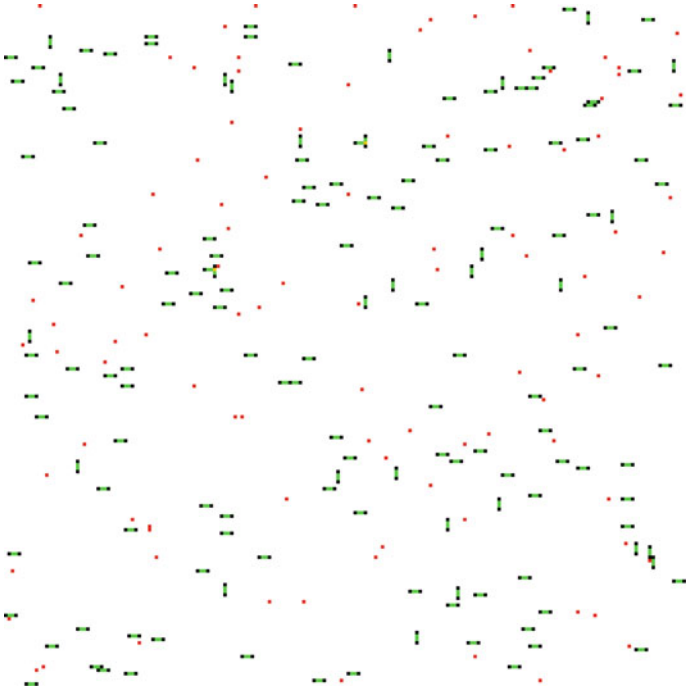

Fig. 2.18 Particle configuration at time $t = t_0 = 18000$ in the case $\varphi = \pi/6$. Here the thermally activated particles are expressed by *red dots* and the inactivated particles are by *black dots*. The δ-pairs are marked by *green line-segments* connecting two inactivated particles. We see $M_{\rm h}^{\delta}(t_0) = 29$ and $M_{\rm v}^{\delta}(t_0) = 152$

$$\tan^2 \varphi_{\rm pair} = \left(\frac{M_{\rm v}^{\delta}(t_0)}{M_{\rm h}^{\delta}(t_0)} \right)^{-1}, \tag{2.50}$$

the above result (2.49) gives

$$\varphi_{\rm pair} \simeq 0.412, \tag{2.51}$$

which is slightly smaller than $\overline{\varphi}^{\rm op}$ given by (2.48).

Kawazoe et al. [29] reported the time dependence of the degree of polarization in the fabrication process (see Fig. 2b in [29]). This quantity will be represented in our notation as

$$d_{\rm pol}(t) = \frac{P_{\rm h}(t) - P_{\rm v}(t)}{P_{\rm h}(t) + P_{\rm v}(t)} = \frac{1 - \tan^2 \varphi^{\rm fab}(t)}{1 + \tan^2 \varphi^{\rm fab}(t)}, \tag{2.52}$$

where

$$\varphi^{\rm fab}(t) = \tan^{-1} \sqrt{\frac{P_{\rm v}(t)}{P_{\rm h}(t)}} \tag{2.53}$$

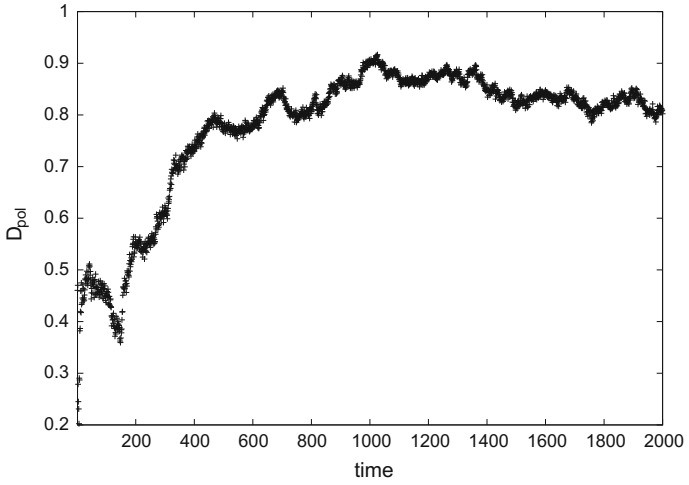

Fig. 2.19 Time dependence of the degree of polarization d_{pol} in the transient regime of fabrication process. d_{pol} shows a relaxation to the stationary value 0.843

denotes the polarization angle of the emitted light at time t in the fabrication process $0 < t < t_0$. Figure 2.19 shows the plots obtained from the simulation result given by Fig. 2.16. In this case $d(t)$ shows a relaxation to the equilibrium value 0.843. This figure shall be compared with the experimental results given by Fig. 2b in [29]. We will briefly discuss this modification of polarization angle from φ to $\overline{\varphi}^{\mathrm{fab}}$, $\overline{\varphi}^{\mathrm{op}}$, and $\varphi^{\mathrm{fab}}(t)$, $0 < t < t_0$ in Sect. 2.8.

2.7 Spectrum of Light Controlled in Photon Breeding

Here we would like to demonstrate that the present model can simulate another important property of photon breeding assisted by DPP; the spectrum of emitted light from the Si-LED is controlled by the light incident in the fabrication process. See **[E6]** in Sect. 2.2.1.

For simplicity, we choose two different wavelengths $\lambda_1 > \lambda_2$ and assume that the incident light consists of the light with these two wavelengths. Let the intensities of these two components be a_1 and a_2, respectively,

$$\rho(\lambda) = a_1\delta(\lambda - \lambda_1) + a_2\delta(\lambda - \lambda_2). \tag{2.54}$$

The balance equation of energy (2.1) between phonons and photons is generalized as

$$E_{\mathrm{g}} - \delta E_{\mathrm{phonon}} = h\nu_{\mathrm{anneal}} = h\nu_{\mathrm{emission}} \tag{2.55}$$

for general value δ of δ-pairs. If we use the dispersion relation of light, $E = h\nu = hc/\lambda$ with the light speed c, we have the formula

$$E_{\rm g} - \delta E_{\rm phonon} = \frac{hc}{\lambda}, \tag{2.56}$$

which relates the wavelength of the incident light in the fabrication process and the separation of δ-pairs constructed by the DPP-assisted annealing. We assume the correspondence

$$\lambda_1 \Longleftrightarrow \delta_1, \quad \lambda_2 \Longleftrightarrow \delta_2. \tag{2.57}$$

Note that the formula (2.56) implies, if $\lambda_1 > \lambda_2$ then $\delta_1 < \delta_2$.

Now we perform our simulation by setting

$$\delta_1 = 3 \quad \text{and} \quad \delta_2 = 5 \tag{2.58}$$

with the intensity rate $a_1 : a_2 = 2 : 1$ for the incident light.

We assume that the polarization angles are $\pi/4$ for both wavelengths. We set

$$\begin{aligned} P_{\rm h}^{0,\lambda_1} &= P_{\rm v}^{0,\lambda_1} = \frac{1}{2} P^{0,\lambda_1} = 40, \\ P_{\rm h}^{0,\lambda_2} &= P_{\rm v}^{0,\lambda_2} = \frac{1}{2} P^{0,\lambda_2} = 20. \end{aligned} \tag{2.59}$$

Other parameters are given by (2.25) and $I = 40$, $t_0 = 18000$.

Figure 2.20 shows the time dependence of the total power of emitted light with the wavelength $\lambda = \lambda_1$,

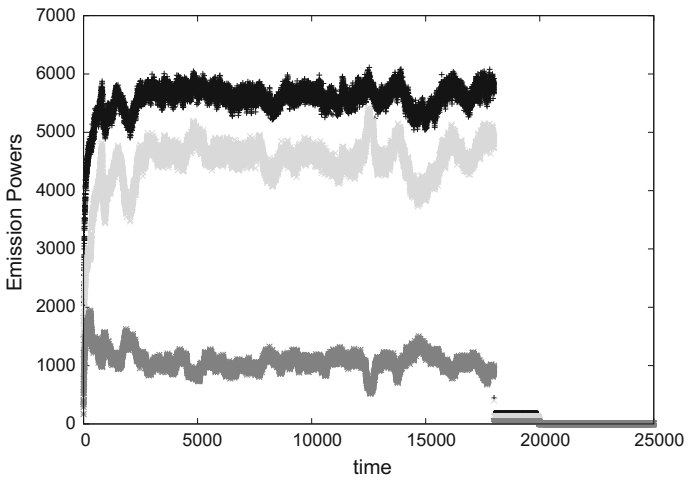

Fig. 2.20 $P^{\lambda_1}(t)$ (*light gray dots*), $P^{\lambda_2}(t)$ (*dark gray dots*), and their sum $P(t) = P^{\lambda_1}(t) + P^{\lambda_2}(t)$ (*black dots*) of emitted light

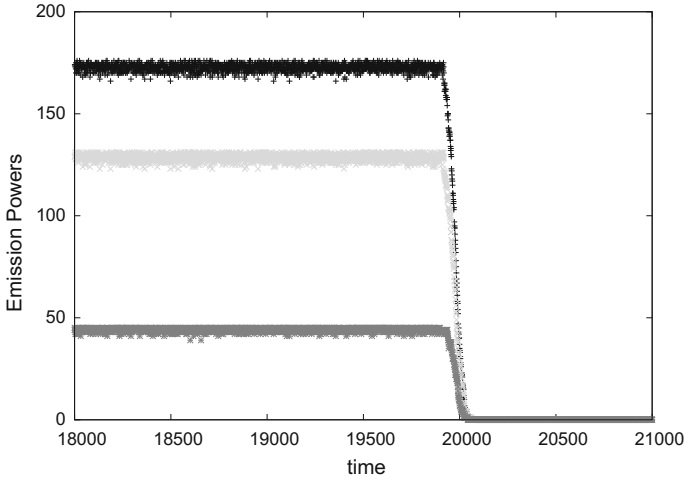

Fig. 2.21 Detailed plots of emitted light powers $P^{\lambda_1}(t)$ (*light gray dots*) and $P^{\lambda_2}(t)$ (*dark gray dots*), and their sum $P(t) = P^{\lambda_1}(t) + P^{\lambda_2}(t)$ (*black dots*) in the operation regimes

$$P^{\lambda_1}(t) = P_{\mathrm{h}}^{\lambda_1}(t) + P_{\mathrm{v}}^{\lambda_1}(t), \tag{2.60}$$

and that with wavelength $\lambda = \lambda_2$,

$$P^{\lambda_2}(t) = P_{\mathrm{h}}^{\lambda_2}(t) + P_{\mathrm{v}}^{\lambda_2}(t). \tag{2.61}$$

The plots only in the operation regimes are also given in Fig. 2.21.

These plots give the values, $\overline{P}^{\mathrm{fab},\lambda_1} = 4555$, $\overline{P}^{\mathrm{fab},\lambda_2} = 1055$, $\overline{P}^{\mathrm{op},\lambda_1} = 129$, $\overline{P}^{\mathrm{op},\lambda_1} = 44$, and thus we have the ratios as

$$\begin{aligned} &\frac{\overline{P}^{\mathrm{fab},\lambda_2}}{\overline{P}^{\mathrm{fab},\lambda_1}} = 0.232, \\ &\frac{\overline{P}^{\mathrm{op},\lambda_2}}{\overline{P}^{\mathrm{op},\lambda_1}} = 0.341. \end{aligned} \tag{2.62}$$

The intensity ratio of the two wavelengths is modified in the photon breeding from the value for the incident light $a_2/a_1 = P^{0,\lambda_2}/P^{0,\lambda_1} = 0.5$.

The spectrum of incident light (2.54) is memorized in the δ-pair distribution as shown by Fig. 2.22. We see $M^{\delta=3}(t_0) = 131$ and $M^{\delta=5}(t_0) = 45$, which gives

$$\frac{M^{\delta=5}(t_0)}{M^{\delta=3}(t_0)} \simeq 0.344. \tag{2.63}$$

This value coincides with the ratio $\overline{P}^{\mathrm{op},\lambda_2}/\overline{P}^{\mathrm{op},\lambda_1}$ given by (2.62).

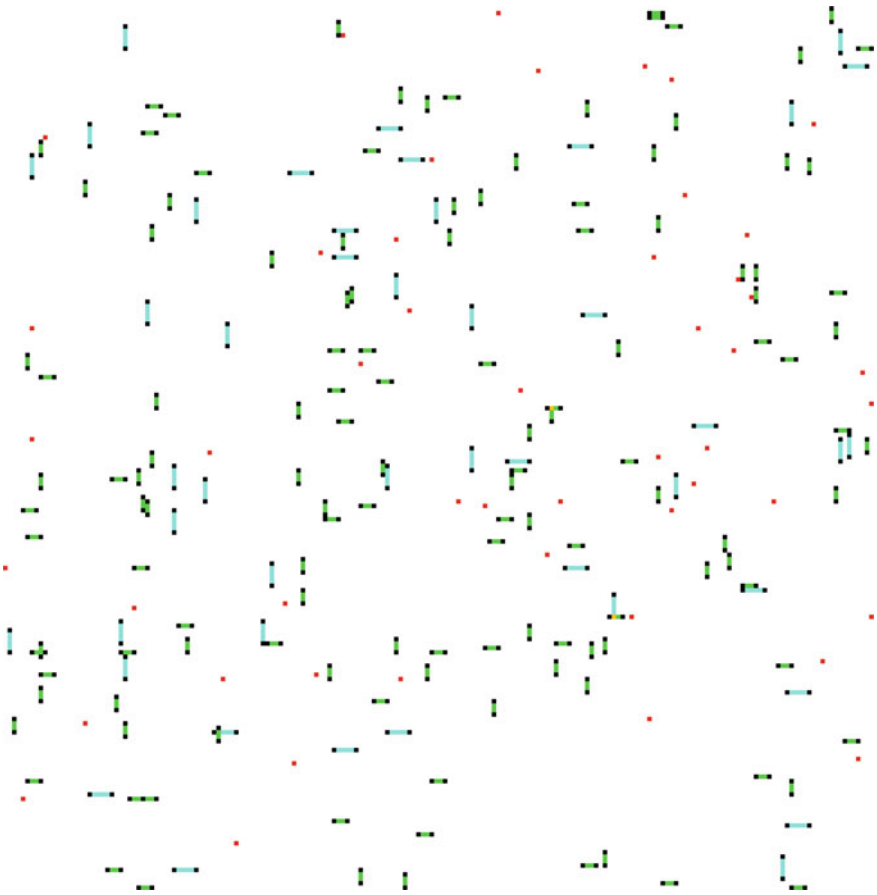

Fig. 2.22 Particle configuration at time $t = t_0 = 18000$. Here the thermally activated particles are expressed by *red dots* and the inactivated particles are by *black dots*. The δ-pairs with $\delta = 3$ are marked by *green line-segments* and the δ-pairs with $\delta = 5$ are by *blue line-segments*, respectively. We see $M^{\delta=3}(t_0) = 131$ and $M^{\delta=5}(t_0) = 45$

We will briefly discuss this modification of spectrum, i.e., the change of the ratio from $P^{0,\lambda_2}/P^{0,\lambda_1} = 0.5$ to (2.62), in Sect. 2.8.

2.8 Future Problems

In this last section, we list up future problems.

1. In Sect. 2.6.2, we reported the case that the incident light was linearly polarized in the direction $\varphi = \pi/6$ with respect to the x_1-axis ($\mathbf{e}_h$-axis). There, the powers

of the horizontal and the vertical components of the irradiation light were given by $P_{\rm h}^0 = 60$ and $P_{\rm v}^0 = 20$, respectively. As shown by (2.48), the polarization angles of emitted light averaged in the fabrication process, $\overline{\varphi}^{\rm fab}$, and that in the operation process, $\overline{\varphi}^{\rm op}$, are both smaller than the initial value $\varphi = \pi/6$. The reason of disagreement is the following. In the fabrication process, we have chosen the value of current as $I = 60$ as shown by (2.44). Therefore, we have matching, $I = P_{\rm h}^0$, for the horizontal component of incident light, and thus the power of emitted light was maximized as discussed in Sect. 2.5. This means at the same time that, concerning the vertical component of incident light, we have mismatching, $I = 60 > P_{\rm v}^0 = 20$, and $\overline{P}_{\rm v}^{\rm fab}$ (resp. $\overline{P}_{\rm v}^{\rm op}$) becomes smaller than 1/3 of $\overline{P}_{\rm h}^{\rm fab}$ (resp. $\overline{P}_{\rm h}^{\rm op}$). More systematic study of dependence on I injected in fabrication for this polarization-modification $\varphi \to (\overline{\varphi}^{\rm fab}, \overline{\varphi}^{\rm op})$ should be studied as a future problem. Time evolution of the polarization-modification $\varphi^{\rm fab}(t)$ in the fabrication process will be an interesting problem.

2. In Sect. 2.7, we considered the case that the incident light is the superposition of two components of light with different wavelengths, $\lambda_2 > \lambda_1$. The ratio of intensities of these two components was 2:1. We showed that the emitted light also consisted of two components with these two wavelengths, but the ratio of powers were modified as (2.62). This modification can be also explained qualitatively by the 'matching argument of I and P^0' as for the polarization-modification; In Sect. 2.7 we imposed the matching for the component with λ_1; $P_{\rm h}^{0,\lambda_1} = P_{\rm v}^{0,\lambda_1} = 40 = I$, but did not for the component with λ_2; $P_{\rm h}^{0,\lambda_2} = P_{\rm v}^{0,\lambda_2} = 20 < 40 = I$, and thus the ratios $\overline{P}^{{\rm fab},\lambda_2}/\overline{P}^{{\rm fab},\lambda_1}$ and $\overline{P}^{{\rm op},\lambda_2}/\overline{P}^{{\rm op},\lambda_1}$ were smaller than the initial ratio 1/2. We can expect that, if we impose the matching for the component with λ_2, these ratios would be larger than 1/2. This consideration implies the possibility such that we can control the spectrum of emitted light by changing the value of I injected in the fabrication process. Precise estimations for emitted-light spectra on I injected in the fabrication processes will be a future problem. One of the keys to solve this problem and the problem concerning the polarization-modification mentioned above will be the precise evaluation of emitted power of light as a function of $P^0/2I$ (see Figs. 2.10 and 2.11 in the present paper and Fig. 6 in [30]). Dependence of the maximum position, the variance, and the skewness of this function on various parameters of models as well as experimental conditions should be clarified.
3. In the present study, we have approximated the quasi-two-dimensional domains in the Si and GaP crystals in which B and Zn atoms are efficiently doped, by a square lattice. It was an oversimplification. As a matter of fact, inhomogeneity of the doped B atoms in the x_3-direction (the depth direction from the Si surface) has been carefully prepared by ion implantation before the DPP-assisted annealing. The density profile of B atoms along the x_3-axis observed after the annealing was shown by Fig. 1b in [29]. Such a unique profile of concentration will generate inhomogeneity along the x_3-axis of electrical resistivity, and hence the diffusive motion of B atoms caused by the Joule heat in the annealing process will essentially depend on the x_3-coordinate. In order to make it possible to compare

simulation results directly to the experimental data reported in [28–30], we should perform simulation of the models defined on more realistic three-dimensional lattices, e.g., on the diamond cubic crystal structures. One of the most interesting aspects of the photon breeding mechanics may be the experimental fact that the basic properties of light incident in the fabrication process are embedded in the random spatial-configurations of doped atoms. In the present work, we have studied only correlations between nearest-neighbor pairs of points representing doped atoms. Characterization of random point configurations with spatial correlations is in general very important and interesting problem in statistical mechanics and probability theory (see, for example, [31]). Further study of the random point configurations of doped atoms is desired, which are self-organized in the fabrication by DPP-assisted annealing.

4. Concerning the present results on lifetime of LED, Ohtsu kindly pointed out that the real Si-LEDs and GaP-LEDs fabricated in experiments seem to be very stable and their lifetimes as LEDs are much longer than the values evaluated in the present theoretical models. One of the reasons for this failure of our modeling would be that we did not take into account the experimental fact and the consideration reported by Kim et al. [30] that the barrier height $V_{\rm ex}$ in their *two-level two-state model* can be changed by applying an external field of irradiation light (see Sect. 4.1 of [30]). In our setting, the barrier height $V_{\rm ex}$ controls the transition rate between the thermally activated state ($\alpha^{(j)} = +$) and the non-activated state ($\alpha^{(j)} = -$) of random walkers representing B atoms. Kim et al. [30] concluded that $V_{\rm ex}$ becomes larger in the absence of an external filed, and it implies that the transition rate $\gamma \propto \exp(-V_{\rm ex}/k_{\rm B}T)$ will exponentially decrease. We will be able to take into account this effect by enlarging the threshold value c_3 for the aging effect of δ-pairs in the operation process, since $P^0 \equiv 0$ in this process. Further improvements of the present models should be done in the future.

Acknowledgements The present authors would like to thank M. Ohtsu, M. Naruse, T. Kawazoe, J.H. Kim, and S. Tojo for useful instructions and stimulating discussions on the DP and DPP phenomena. They are grateful to M. Ohtsu for careful reading of the manuscript, very useful comments for improving the descriptions, and giving them encouragements to study DP and DPP phenomena from the viewpoint of statistical mechanics. MK thanks K. Takahashi for the collaboration in an early stage of the present research program. MK also thanks T. Sasamoto for useful discussion on the recent progress of nonequilibrium statistical physics. This work was supported by the Grand-in-Aid for Challenging Exploratory Research (No. 15K13374) of Japan Society for the Promotion of Science. MK is supported in part by the Grant-in-Aid for Scientific Research (C) (No. 26400405) of Japan Society for the Promotion of Science.

References

1. M. Ohtsu, *Dressed Photons: Concepts of Light-Matter Fusion Technology, Nano-Optics and Nanophotonics* (Springer, Berlin, 2014)
2. M. Ohtsu (ed.), *Progress in Nanophotonics 1, Nano-Optics and Nanophotonics* (Springer, Berlin, 2011)

3. M. Ohtsu (ed.), *Progress in Nanophotonics 2, Nano-Optics and Nanophotonics* (Springer, Berlin, 2013)
4. M. Ohtsu, T. Yatsui (eds.), *Progress in Nanophotonics 3, Nano-Optics and Nanophotonics* (Springer, Berlin, 2015)
5. M. Naruse (ed.), *Nanophotonic Information Physics: Nanointelligence and Nanophotonic Computing, Nano-Optics and Nanophotonics* (Springer, Berlin, 2014)
6. D.J. Evans, D.J. Searles, Adv. Phys. **51**, 1529 (2002)
7. G. Gallavotti, *Statistical Mechanics: A Short Treatise* (Springer, Berlin, 1999)
8. K.A. Takeuchi, M. Sano, T. Sasamoto, H. Spohn, Sci. Rep. **1**, 34 (2011)
9. J. Quastel, H. Spohn, J. Stat. Phys. **160**, 965 (2015)
10. T. Sasamoto. Prog. Theor. Exp. Phys. **2016**, 022A01 (2016)
11. K. Takahashi, M. Katori, M. Naruse, M. Ohtsu, Appl. Phys. B **120**, 247 (2015)
12. M. Naruse, T. Kawazoe, T. Yatsui, N. Tate, M. Ohtsu, Appl. Phys. B **105**, 185 (2011)
13. S. Yukutake, T. Kawazoe, T. Yatsui, W. Nomura, K. Kitamura, M. Ohtsu, Appl. Phys. B **99**, 415 (2010)
14. P. Bak, C. Tang, K. Wiesenfeld, Phys. Rev. Lett. **59**, 381 (1987)
15. D. Dhar, Phys. Rev. Lett. **64**, 1613 (1990)
16. M. Katori, H. Kobayashi, Physica **229**, 461 (1996)
17. G. Pruessner, *Self-Organized Criticality—Theory. Models and Characterisation* (Cambridge University Press, Cambridge, 2012)
18. P. Bak, *How Nature Works* (Copernicus, New York, 1996)
19. T. Vicsek, *Fractal Growth Phenomena*, 2nd edn. (World Scientific, Singapore, 1992)
20. D. Dhar, T. Sadhu, J. Stat. Mech. **2013**, P11006 (2013)
21. M. Naruse, T. Yatsui, H. Hori, K. Kitamura, M. Ohtsu, Opt. Express **15**, 11790 (2007)
22. M. Katori, *Bessel Processes, Schramm–Loewner Evolution, and the Dyson Model* (Springer, 2016)
23. P.J. Forrester, *Log-Gases and Random Matrices* (Princeton University Press, Princeton, 2010)
24. G.W. Anderson, G.A. Guionnet, O. Zeitouni, *An Introduction to Random Matrices* (Cambridge University Press, Cambridge, 2010)
25. M. Naruse, Y. Liu, W. Nomura, T. Yatsui, M. Aida, L.B. Kish, M. Ohtsu, Appl. Phys. Lett. **100**, 193106 (2012)
26. M. Naruse, T. Yatsui, W. Nomura, T. Kawazoe, M. Aida, M. Ohtsu, Appl. Phys. Lett. **102**, 071603 (2013)
27. M. Naruse, S-J. Kim, T. Takahashi, K. Akahane, M. D'Acunto, H. Hori, L. Thylén, M. Katori, M. Ohtsu, Percolation of optical excitation mediated by near-field interactions, preprint
28. M. Ohtsu, T. Kawazoe, Silicon light emitting diodes and lasers using dressed photons, in *Progress in Nanophotonics 3*, ed. by M. Ohtsu (Springer, Berlin, 2015), pp. 1–56
29. T. Kawazoe, K. Nishioka, M. Ohtsu, Appl. Phys. A **121**, 1409 (2015)
30. J.H. Kim, T. Kawazoe, M. Ohtsu, Appl. Phys. A **121**, 1395 (2015)
31. J.B. Hough, M. Krishnapur, Y. Peres, B. Virág, *Zeros of Gaussian Analytic Functions and Determinantal Point Processes* (American Mathematical Society, Providence, 2009)

Chapter 3
Near-Field Assisted Chemical Reactions and Its Applications

Takashi Yatsui and Katsuyuki Nobusada

Abstract This chapter describes the recent progress of the near-field-assisted chemical reactions. Since the optical near-field localized only in the proximity of the nano-scale structures, it can achieve the selective optical reaction at the nano-scale. Using this phenomenon, many applications have been developed including the energy upconversion for an artificial photosynthesis and the energy upconversion for an near-field etching for ultraflat surface.

3.1 Optical Near-Field—Nonuniform Electric-Field Distribution—

Optical near-field offers a promising solution for decreasing the size of photonic devices [1, 2], and fabrication feature sizes [3] beyond the diffraction limit of light. If a nanoparticle is illuminated by propagating light, it generates scattered light, which propagates to the far field and exhibits diffraction. However, also generated at the surface of the particle is the optical near-field, which is non-propagating light whose energy is localized at the particle surface, in which due to its field localization the optical near-field can realize the dipole forbidden transitions [4, 5]. Furthermore, the extent of localization is equivalent to the particle size, which is independent of the incident light wavelength, and thus, in the case of a nanoparticle, it is much smaller than the wavelength. Therefore, if the optical near-field is utilized for fabrication, novel technologies that can break through the constraints imposed by the diffraction-limit can be realized [6].

T. Yatsui (✉)
School of Engineering, University of Tokyo, 7-3-1 Hongo, Bunkyo-ku, Tokyo 113-8656, Japan
e-mail: yastui@ee.t.u-tokyo.ac.jp

K. Nobusada
Department of Theoretical and Computational Molecular Science, Institute for Molecular Science, 38 Nishigo-Naka, Myodaiji, Okazaki, Aichi 444-8585, Japan
e-mail: nobusada@ims.ac.jp

M. Ohtsu and T. Yatsui (eds.), *Progress in Nanophotonics 4*,
Nano-Optics and Nanophotonics, DOI 10.1007/978-3-319-49013-7_3

More recently, it was found that the localization of the field has inherent property. In through the investigation of the effect on electron excitation in a quantum dot (QD) using model calculations taking account a density matrix formalism and a classical Lorentz model, the electric field gradient of the optical near-field generates second harmonics [7, 8]. The effect can be found by the following equations. Since the optical field gradient should be expressed as

$$\mathbf{E}(\mathbf{r}, t) = \mathbf{E}(\mathbf{r}_0 + \Delta\mathbf{r}, t) \simeq \mathbf{E}(\mathbf{r}_0, t) + \sum_{i,j} \left(\frac{\partial E_i}{\partial r_j} \right)_{\mathbf{r}_0} \Delta r_j \tag{3.1}$$

where i and j indicate a Cartesian coordinate (x or y), and $\mathbf{r}$ is the representative position of electrons following an oscillating electric field. By using $\mathbf{E}(\mathbf{r}_0, t) = \mathbf{E}_0(\mathbf{r}_0, t)\left(e^{-i\frac{\omega_0}{2}t} + e^{i\frac{\omega_0}{2}t}\right)$ and $\Delta\mathbf{r} = \Delta\mathbf{r}_0\left(e^{-i\frac{\omega_0}{2}t} + e^{i\frac{\omega_0}{2}t}\right)$, the (3.1) can be rewritten as

$$\mathbf{E}(\mathbf{r}, t) = \mathbf{E}(\mathbf{r}_0)\, e^{-i\frac{\omega_0}{2}t} + \Delta r_{j0} \sum_{i,j} \left(\frac{\partial E_{i0}}{\partial r_j} \right)_{\mathbf{r}_0} \left(1 + e^{-i\omega_0 t}\right) + c.c. \tag{3.2}$$

implying the electrons excited by the nonuniform electric field generate a second harmonic component ω_0. In other words, the energy upconversion is expected in the localized field.

3.2 Near-Field Assisted Energy Upconversion

As is described above, the optical near-field induces the energy upconversion. Many chemical reactions including photolithography [7], hydrogen generation, CO_2 reduction, require the high photon energy as much as 4 eV (wavelength of 310 nm) to dissociate molecules. Since the sun light has ultraviolet region as small as 5%, the energy upconversion of the photon will improve the efficiency of the sun light utilization.

3.2.1 Hydrogen Generation

Honda and Fujishima discovered that the excited electron in TiO_2 generates hydrogen from the water [9]. However, since TiO_2 has a bandgap energy of 3.2 eV (corresponds to the wavelength of 390 nm), it requires the ultraviolet light. Recent progress realize the visible light water splitting by using narrow band gap materials [10, 11], in other words, band gap engineering. In addition to the band gap engineering, the utilization of the optical near-field will improve the efficiency the utilization of the photon energy lower than the band gap energy [12].

To confirm the effect of the optical near-field, ZnO nanorods were used as a near-field source. To check the effect of the optical near-field the thick and thin nanorods were prepared. ZnO nanorods were deposited using metalorganic vapor epitaxy (MOVPE) method [13]. Diethylzinc (DEZn) and oxygen are used as the reactants, with argon as the carrier gas. The pressure inside the reactant chamber is maintained at 5 Torr. The substrate temperature is controlled using a thermocouple thermometer and radio-frequency-heated carbon susceptor. To observe the size dependence, we applied two-temperature growth method [14]; lower-temperature growth of vertically aligned thick ZnO nanorods and subsequent higher-temperature growth of vertically aligned thin ZnO nanorods. In the first step, vertically aligned thick nanorods are grown at 450°C for 30 min. In the second step, ultrafine nanorods were grown at 750°C for 10 min. at the tips of the preformed thick nanorods. Thick and thin nanorods were grown with first step only and two-step, respectively. The ZnO nanorods were grown on a 200 nm indium tin oxide (ITO) thin film on a sapphire (0001) substrate. Figure 3.1 shows the scanning electron microscopic (SEM) images of fabricated ZnO nanorods and the average diameters of thick and thin were 100 nm and 20 nm, respectively.

Figure 3.2 shows a schematic of the experimental setup. The counter and reference electrodes were a Pt wire and Ag/AgCl/NaCl (3 mol/L), respectively. To examine dependence of the photocurrent on the photon energy of the excitation light source relative to the band gap energy of ZnO (3.3 eV), a continuous wave (CW) He-Cd laser (photon energy $h\nu$ = 3.8 eV) was used as an ultraviolet (UV) radiation source. In addition, as light sources, CW lasers ($h\nu$ = 2.62, 2.33, and 1.85 1.53 eV) with a diameter of 1 mm were used. We used 0.1 mol/L NaOH solution as the electrolyte. All experiments were performed at room temperature. The lasers were irradiated for 20 s repeatedly at 20 s intervals. The value of the current was determined as the difference in the values before and after the laser was turned off. A potentiostat was used for the electrochemical measurements. The photoelectrochemical reaction rate was monitored as the current under laser irradiation. Hydrogen and oxygen

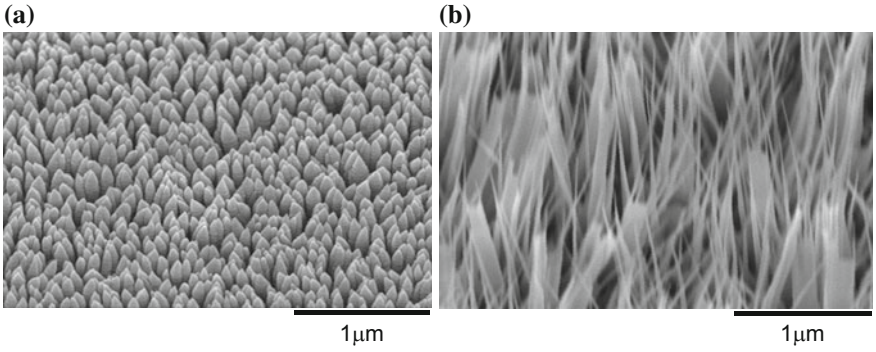

Fig. 3.1 SEM images of ZnO nanorods with a diameter of **a** 100 nm (one-step growth) and 20 nm (two-step growth)

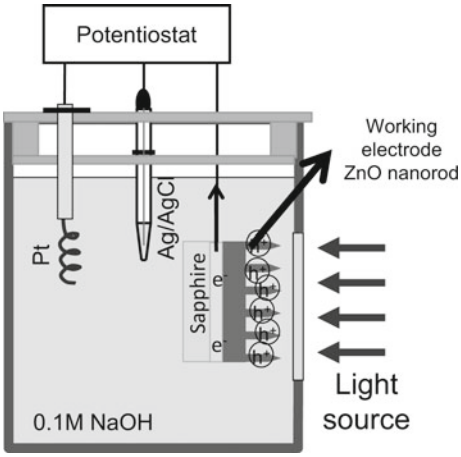

Fig. 3.2 Photocurrent measurement setup. The photocatalytic water splitting performance is evaluated by performing a photoelectrochemical measurement with ZnO nanorod as the working electrode, Ag/AgCl as the reference electrode, and Pt as the counter electrode

were respectively generated at the Pt counter electrode and ZnO nanorod working electrode as follows [15]:

$$2H_2O + 2e^- \rightarrow H_2 + 2OH^- \tag{3.3a}$$

$$2OH^- \rightarrow 1/2O_2 + H_2O + 2e^- \tag{3.3b}$$

The dependence of the photocurrent on the laser power was measure with photon energies hν of 2.62, 2.33, and 1.85 eV (see Fig. 3.3a–c). Although small photocurrent was detected for the bulk ZnO substrate, larger photocurrents were detected for both 100 nm and 20 nm nanorods electrodes. A linear dependence of the photocurrent on laser power was observed for all laser excitation. In the case of an excitation energy of 2.62 eV (Fig. 3.3a), the value of photocurrent in the 100 nm nanorods was 86 fold higher than that in the bulk substrate. Note that a laser power density on the order of W cm^{-2} is 10^{15} times smaller than that used in multiple-photon processing with an ultra-short-pulse laser [16]. Therefore, the near-field-assisted excitation process did not originate from a conventional multiple-photon excitation process.

For further evaluation of the dependence of the photocurrent on the incident photon energy, the incident-photon-to-current conversion efficiency (IPCE) were determined (see Fig. 3.4). The IPCE) were determined (see Fig. 3.4 value of the 100 nm nanorods was the largest at 2.62 eV, the IPCE) were determined (see Fig. 3.4 value of the 20 nm nanorods was the largest at all other excitation levels).

In though the above experiments, a near-field assisted excitation process was carried out using ZnO nanorods. Photocatalytic reaction with smaller photon energy than the band gap energy of the semiconductor electrode was realized. This near-field-assisted excitation process was also confirmed using TiO_2 nanorod electrode [17], and therefore, it can be applicable to other semiconductor materials with narrower bandgap energy.

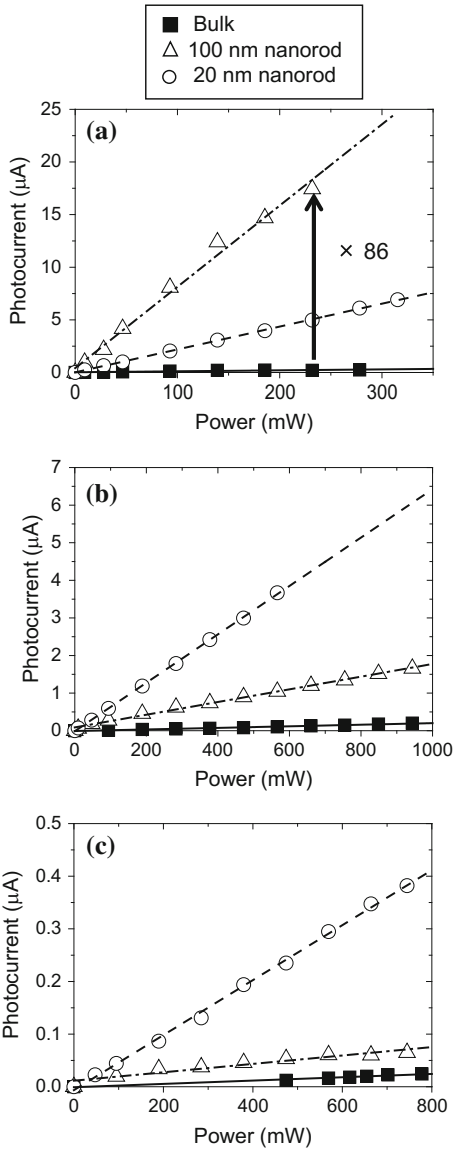

Fig. 3.3 Laser power dependence of current. **a** 2.62 eV (λ = 473 nm), **b** 2.33 eV (λ = 532 nm), and **c** 1.85 eV (λ = 671 nm). The electrode potential was set to 0.5 V (vs. Ag/AgCl)

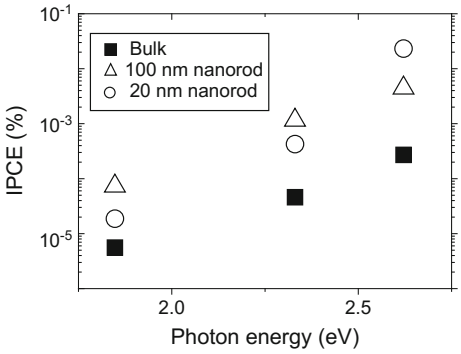

Fig. 3.4 Dependence of IPCE on excitation photon energy

3.2.2 CO_2 Reduction

Carbon dioxide (CO_2) is considered to be one of the major greenhouse gases responsible for global warming. The major reason is the high dissociation energy of CO_2 molecule as much as 7.47 eV, which is equivalent to photon energy of a light source with a wavelength of 166 nm (λ_{dis}) [18]. Therefore, it is considered to be impossible to use sunlight for CO_2 reduction due to the molecule's high bond dissociation energy. To overcome this difficulty, we evaluated near-field assisted energy upconversion to dissociate CO_2 with lower photon energy then the dissociation energy [19].

To induce near-field assisted process, we fabricated ZnO nanorods using two-temperature growth of MOVPE [14]. The SEM images of the fabricated ZnO nanorods are shown in Fig. 3.5. Figure 3.5a demonstrates the morphology of 1-step growth nanorods with an average diameter of 100 nm. Figure 3.5b shows 2-step growth nanorods with an average diameter of 20 nm.

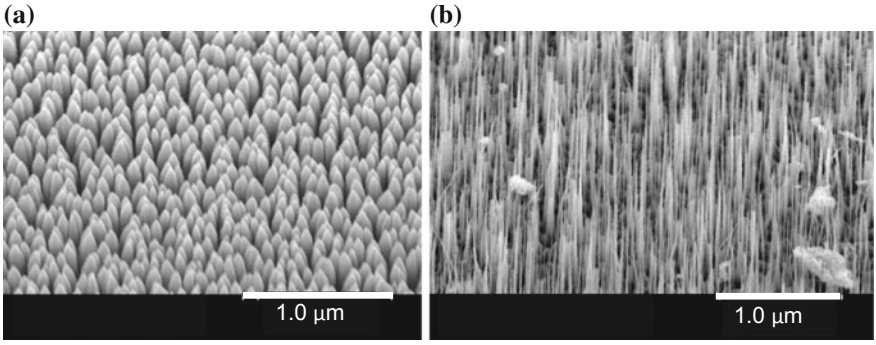

Fig. 3.5 SEM images of ZnO nanorods with a diameter of **a** 100 nm (one-step growth) and 20 nm (two-step growth)

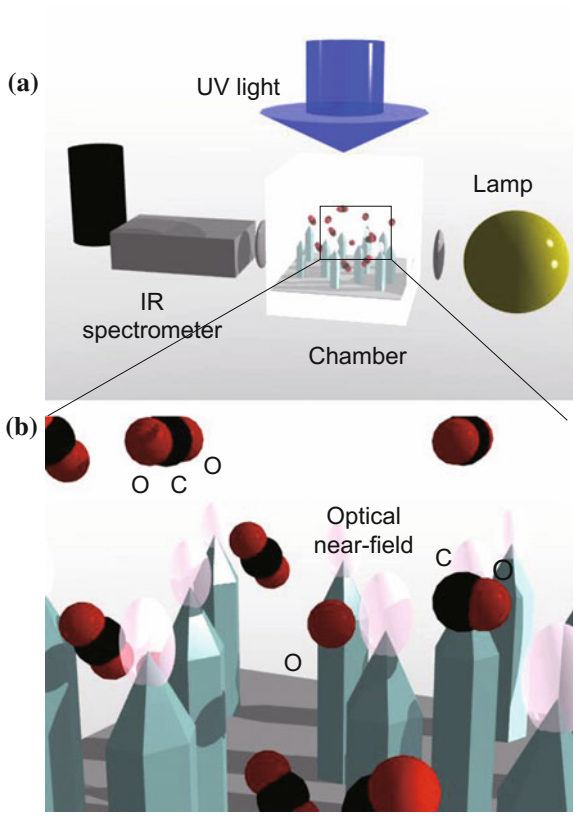

Fig. 3.6 **a** Schematic of CO_2 reduction setup. **b** The optical near-filed generated at the apex of ZnO nanorods, and the CO_2 dissociated selectively at the ZnO nanorod apex

We measured the absorption spectrum of CO_2 in the infrared region using the experimental setup shown in Fig. 3.6. An chamber was filled up with CO_2 gas and the absorption spectrum was measured using an infrared spectrometer. A halogen lamp was used as the light source and optical setup shown in the figure was applied for the measurement.

Using the experimental setup illustrated in Fig. 3.6, we measured the intensity of transmitted light (I_0) without inserting CO_2 gas into the airtight chamber. Later, we filled the chamber with CO_2 and measured the intensity of transmitted light (I). Then the absorption by CO_2 gas was calculated using the equation: absorbance, $A = \ln \frac{I_0}{I}$.

Figure 3.7 shows the typical absorption spectrum of CO_2 in the wavelength range from 1430 to 1440 nm. CO_2 has four independent modes: symmetric stretch (ν_1), antisymmetric stretch (ν_3) and two perpendicular bending modes (ν_2) [20]. The illustration of vibrational modes of CO_2 is shown in Fig. 3.8. Mode expression is expressed as $\nu_1 \nu_3 l \nu_3 n$, where l is angular momentum quantum number and n is the nth component in states linked by rovibrational interaction. The measured absorption spectra were compared with the ones recorded in HITRAN (High-resolution transmission molecular absorption) database [21]. And found that the observed spectrum

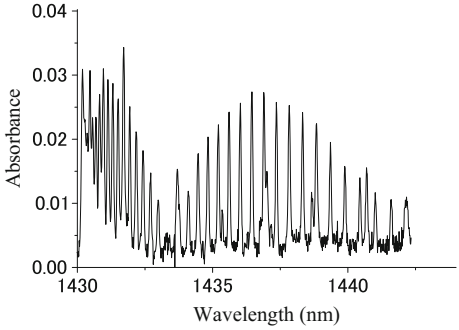

Fig. 3.7 CO_2 absorption spectrum

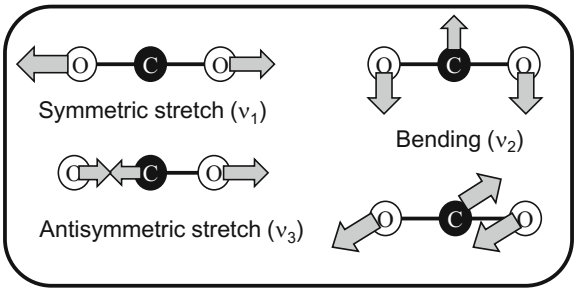

(a) Vibrational motion

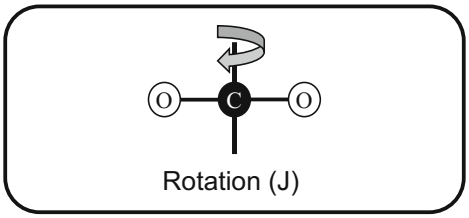

(b) Rotational motion

Fig. 3.8 Vibrational modes of CO_2

in this region corresponds to antisymmetric stretch mode. From the assigned peaks, we obtained the time dependences on A mode (00001 → 00031 at a wavelength of 1434.19 nm) and B mode (01101 → 01131 a wavelength of 1441.94 nm). The relation between A and B modes are shown in Fig. 3.9.

In Fig. 3.10a, the time dependence of absorption change of A mode using 2-step nanorods (Fig. 3.10b) was plotted, in which 5th harmonic YAG laser with a wavelength of 213 nm was used. Similar time dependence was observed in B mode (see Fig. 3.10b). In comparison to the spectra without using nanorods (see dashed lines in Fig. 3.10a, b), the reduction of the CO_2 concentration was confirmed. Figure 3.10a shows the time dependence of absorption change of A mode using 1-step nanorods (Fig. 3.10a), in which 4th harmonic YAG laser with a wavelength of 266 nm was

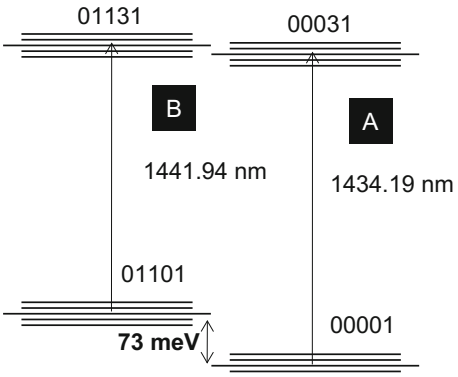

Fig. 3.9 Transition mode diagram of mode A and B

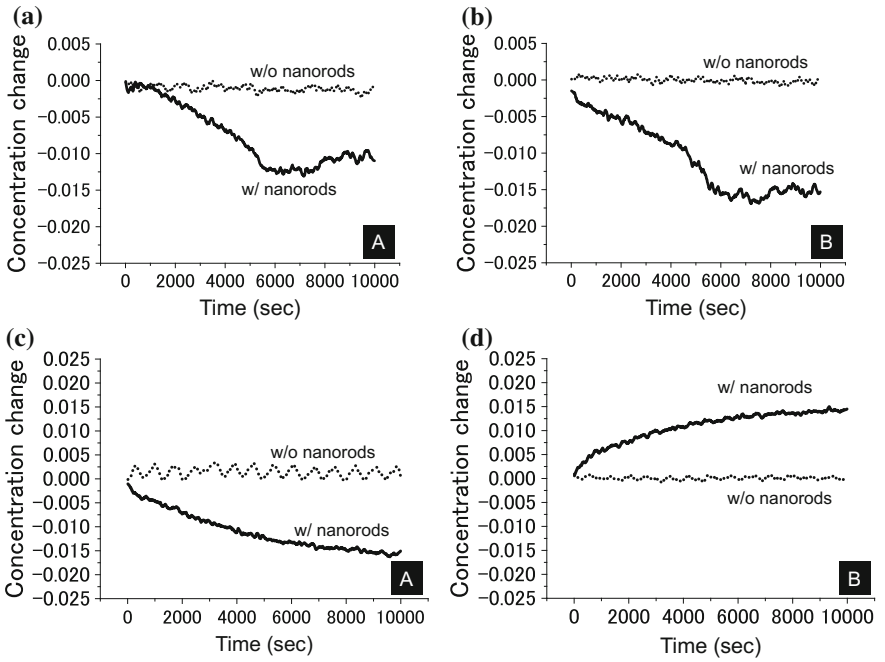

Fig. 3.10 Time dependence of absorption change. **a** Mode A with 213 nm irradiation. **b** Mode B with 213 nm irradiation. **c** Mode A with 266 nm irradiation. **d** Mode B with 266 nm irradiation

used. In comparison to the spectrum of A mode, the concentration of B mode was increased as the exposure time increased (see Fig. 3.10b).

Although it was mentioned that the reduction of CO_2 requires shorter wavelength than 166 nm, the dissociation of CO_2 was confirmed using 213 nm with ZnO nanorods. The absorption energy of CO_2 molecule lies between 200 and 120 nm, which is generally believed to result from electronic transitions from the ground state ($^1\Sigma_g^+$ as shown in Fig. 3.11) to singlet ($^1B_2$) and triplet ($^3B_2$) states. According

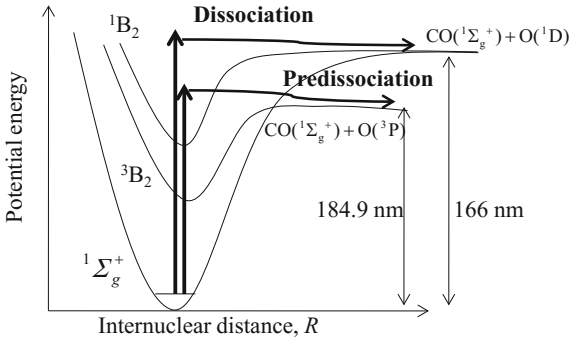

Fig. 3.11 Potential energy curve of CO_2

to the experiments of Slanger and Black [22, 23], incident light of wavelength $\lambda =$ 147 nm results in dissociation of CO_2 and produces CO and O (^{1}D) with a quantum yield of 1.0 [24].

$$CO_2 + h\nu \rightarrow CO(^1\Sigma_g{}^+) + O(^1D) \tag{3.4}$$

The dissociation path of (3.4) is applicable for incident light wavelength $\lambda <$166 nm according to the potential energy diagram of Fig. 3.11. However, dissociation has also been observed experimentally for $\lambda >$ 166 nm. Inn and Heimerl observed a unit quantum yield for dissociation in $\lambda >$ 174 nm [25] according to the following part [26]

$$CO_2 + h\nu \rightarrow CO(^1\Sigma_g{}^+) + O(^3P) \tag{3.5}$$

This dissociation process has also been confirmed by DeMore and Mosesman [27] for $\lambda =$ 184.9 nm; which is believed to take place due to the conversion from the singlet state ($^1B_2$) to the triplet state ($^3B_2$), observed in the potential energy curve. This interconversion between states is quite rapid; and it is concluded by the scientists that CO_2 dissociates at all wavelengths at which there is appreciable absorption ($\lambda <$ 195 nm), since the quantum energy is significantly higher than the barrier to dissociation.

As was shown in the Fig. 3.10, it was found that while irradiating with an incident light wavelength 213 nm, the absorption peaks decrease significantly, implying that dissociation of CO_2 molecules results in this decrease in absorption peaks. However, as was mentioned in the principles of CO_2 dissociation mechanism, propagating light of wavelength 213 nm cannot cause dissociation of CO_2 molecules. Irradiation of nanostructures induces the optical near-field (ONF); which eventually result in the absorption of coherent phonons by CO_2 molecules. As a result, two-step excitation takes place as shown in Fig. 3.12a which makes dissociation or pre-dissociation of CO_2 possible with λ (212 nm) > λ_{dis} (184.9 nm).

Irradiation of 1-step nanorods with incident light wavelength 266 nm cause some of the absorption peaks increase and some decrease. This phenomenon was explained using the near-field assisted process. From the experiment result, we can see that

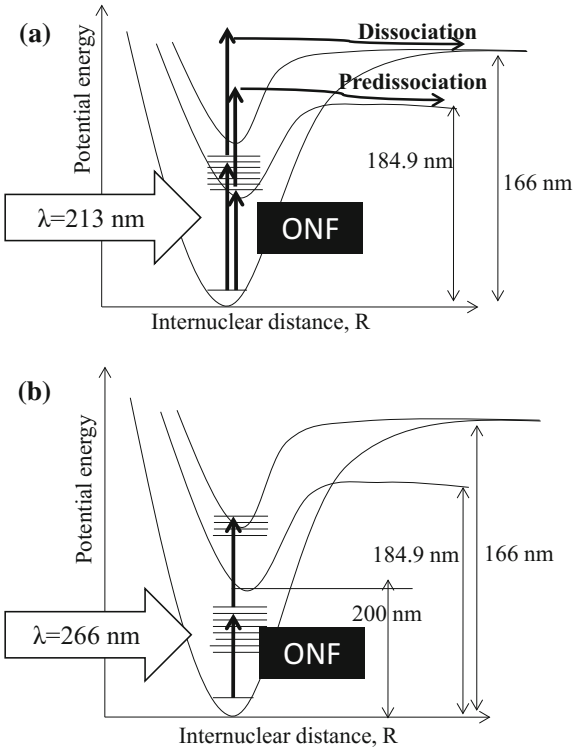

Fig. 3.12 Dissociation of a molecule with phonon assisted process. **a** 213 nm, **b** 266 nm

unlike 213 nm, incident light of wavelength 266 nm does not contain enough energy to cause dissociation of CO_2 molecules. Although the presence of nanorods induce the optical near-field and cause electrons reach the excited state via two-step excitation; the molecule still do not possess enough energy to dissociate. The situation is illustrated in Fig. 3.12b. As the molecules fail to reach a steady state, they relax and eventually emit phonons as heat energy. This heat can contribute to the transition between vibrational modes, specifically from 00001 to 01101. This time, the rate of excitation of vibration modes (i.e. 00001 → 01101) gets higher than the rate of relaxation.

3.3 Near-Field Etching

As was reviewed in the previous section, since the optical near-field dissociate the molecules with lower photon energy than dissociation energy at nano-scale structure, it can applicable to fabrication technique. One of the applications, this section reviews the near-field etching [28].

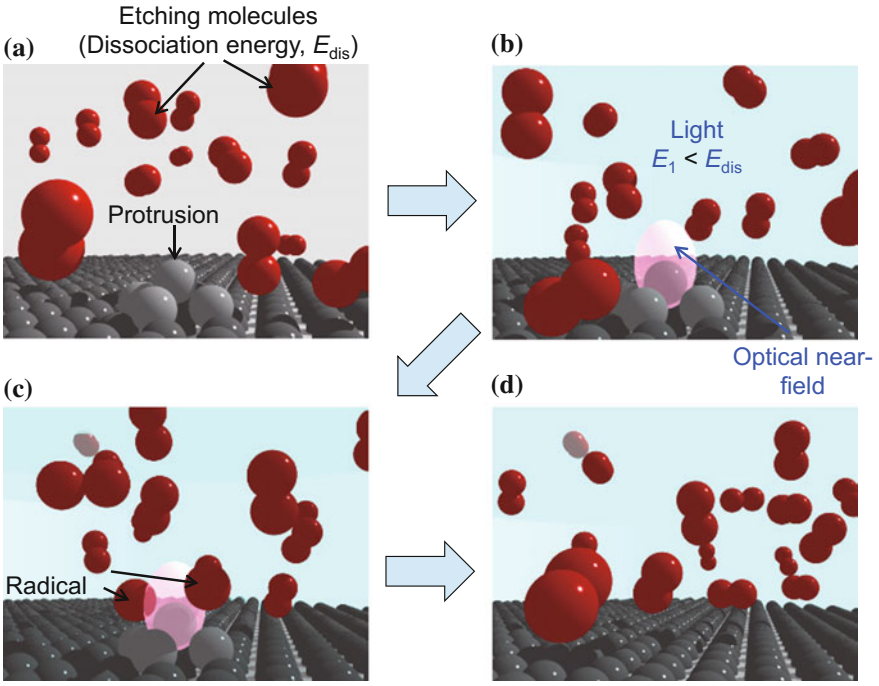

Fig. 3.13 Near-field etching. **a** Without irradiation. Etching molecules has a dissociation energy of E_{diss}. **b** When the light irradiates with a photon energy E_1 ($< E_{diss}$), the optical near-field generates at the protrusion. **c** The molecules comes in the optical near-field, the molecules dissociate selectively. **d** The protrusions are selectively etching away. The optical near-field disappear when the surface becomes flat

The realization of the ultra-flat surface is required in many applications because the rough surface induces the scattering loss of the carriers of electrons and/or photons. Conventionally, mechanical polishing has been developed to flatten surfaces. However, this method is has fatal problem because it resulted in the mechanical scratch and chemical residue such as CeO_2 in the chemical-mechanical polishing (CMP). Furthermore, since CMP is contact method, it cannot be applicable to three dimensional flattening.

To overcome the difficulties, the near-field etching has been developed. The process is following. The near-field etching performed using Cl_2 as an etching gas for glass, GaN, plastic, and so on. Since the absorption edge wavelength of Cl_2 is 400 nm [29], the wavelength used for the etching is selected longer than 400 nm. Now we consider the substrate in Cl_2 atmosphere, the Cl_2 is stable and does not react with the substrate (Fig. 3.13a). When the light with a wavelength of 532 nm is irradiated in Cl_2 atmosphere, the gas phase Cl_2 does not absorb the light. However, the optical near-field generated at the protrusions on the substrate selectively (Fig. 3.13b). Then, the Cl_2 molecules dissociate in the close proximity of the pro-

trusions (Fig. 3.13c). Consequently, the protrusions are selectively etched away and the ultra flat surface can be obtained (Fig. 3.13d). When the substrate becomes flat, since the optical near-field disappears, the etching process automatically stop.

3.3.1 Flat Surface

Using Cl_2 gas of 200 Pa and 532 nm laser (0.28 W cm^{-2}), (001) GaN substrate was flattened [30]. Figure 3.14a, b show the atomic force microscopic (AFM) images and found that the surface roughness R_a decreased as small as 0.14 nm in 30 min.

Similar R_a reduction has been confirmed in glass substrates [28, 31]. The reduction of the surface roughness was aimed to reduce the scattering the photon at the surface. Therefore, the scattering intensity was detected during the near-field etching. The near-field etching was performed with a 532-nm light (0.28 W/cm^2) over the substrate (see Fig. 3.15). The Cl_2 pressure in the chamber was maintained at 100 Pa at room temperature. The scattered light was generated with a 632-nm light (0.127 W/cm2) and spot size diameter 1 mm. The incident light for scattering light detection was polarized perpendicular to the x-axis (P-polarized light), and the polarized light parallel to the x-axis (S-polarized light) was detected through band pass filter (BPF, $\lambda = 632\,\text{nm} \pm 1.5\,\text{nm}$). The scattered light intensity Iscat, detected by a photodetector (PD1), was normalized to the incident light intensity IIN detected by another photodetector (PD2). The surface roughness was also evaluated with the AFM after near-field etching.

Figure 3.16 shows time-dependence of the normalized scattered intensity with the obtained Ra from AFM measurement. From this figure, it was confirmed that the scattered light intensity as Ra decreased. Because the intensity of scattered light decreases with decreasing surface roughness, it should be noted that the flattened substrate has a higher laser-damage threshold due to the reduction of scattered loss at the surface. As was confirmed, non-contact detection of the reduction of surface reduction could be applicable to the structures in which the surface could not be scanned using AFM such as the inner-wall surfaces of cylinders.

The near-field etching is the photo-chemical process, it can be utilize the other etching gas. As for the experiment, the diamond substrate was flattened using O_2 gas. Diamond has strongest hardness among semiconductors, diamond substrates are polished using diamond pad in CMP process. Therefore, the realization of ultra flat surface of diamond is highly required. Since the O_2 has the dissociation edge of 5.12 eV (242 nm) [32], He-Cd laser with a wavelength of 325 nm was used. Figure shows the time-dependent AFM images for diamond (111) substrate [33]. As can be seen, although the diamond substrate has large bump before etching with R_a of 0.457 nm shown in Fig. 3.17a, the near-field etching realized flat surface as small as 0.154 nm in 60 min (Figs. 3.17c and 3.18).

To confirm the near-field selective etching at the nanoscale protrusion, the surface roughness was evaluated using a new function of a standard deviation of the height difference function is given by

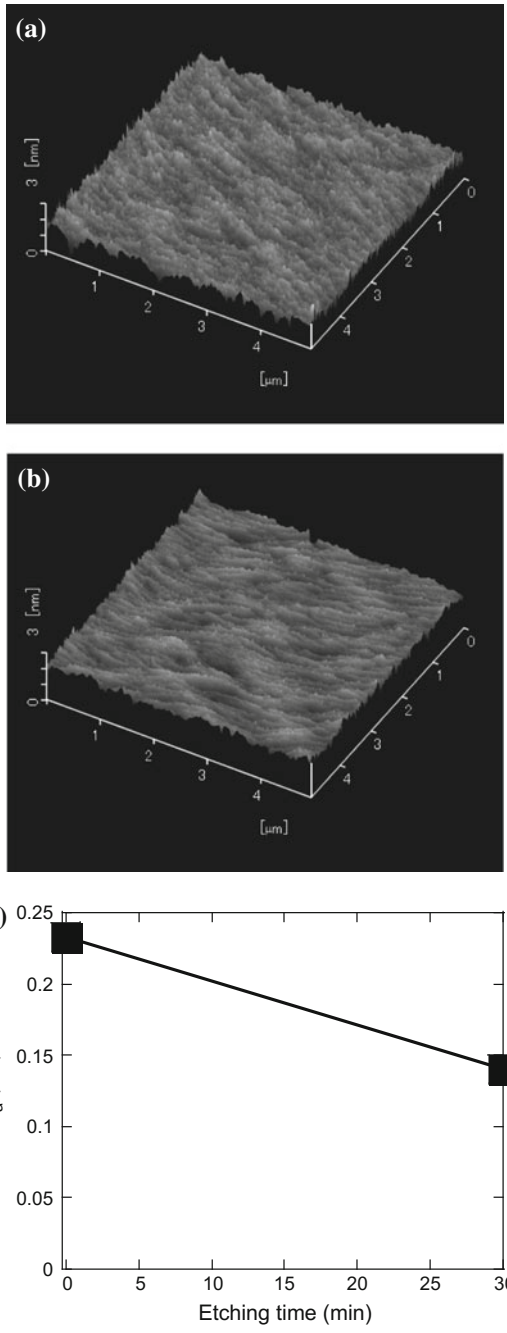

Fig. 3.14 AFM images. **a** Before etching. **b** After etching. **c** Time dependence of surface roughness

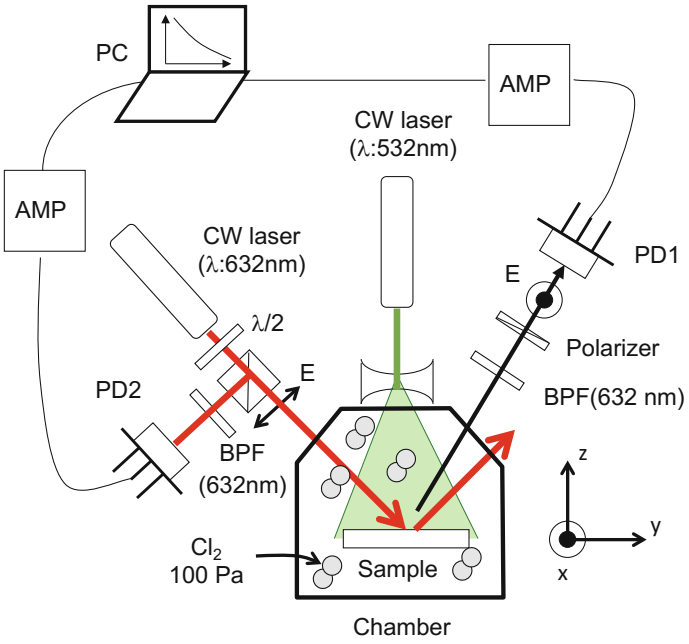

Fig. 3.15 Schematic of the in situ real time monitoring of the surface roughness during the near-field etching

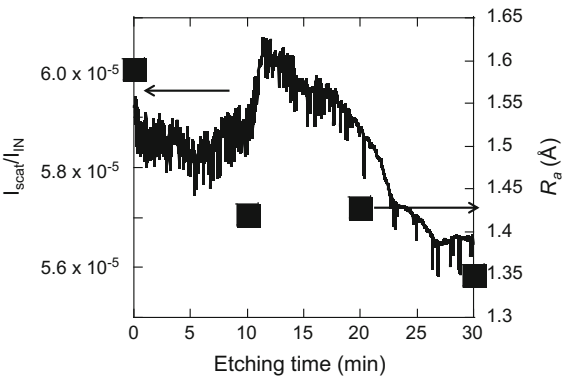

Fig. 3.16 The etching time dependence of the normalized scattered light intensity (*solid curve*) and the Ra (*solid squares*)

$$R\,(l) = \sqrt{\left\langle \left(\overline{z_{k+1}^{(l)}} - \overline{z_k^{(l)}}\right)^2 / 2 \right\rangle} \tag{3.6}$$

where l is the bin size, z is the height from the best-fitting plane, and $\overline{z_k^{(l)}}$ is the average z height of the bin (Fig. 3.19) [34]. While, the value of R_a is determined as

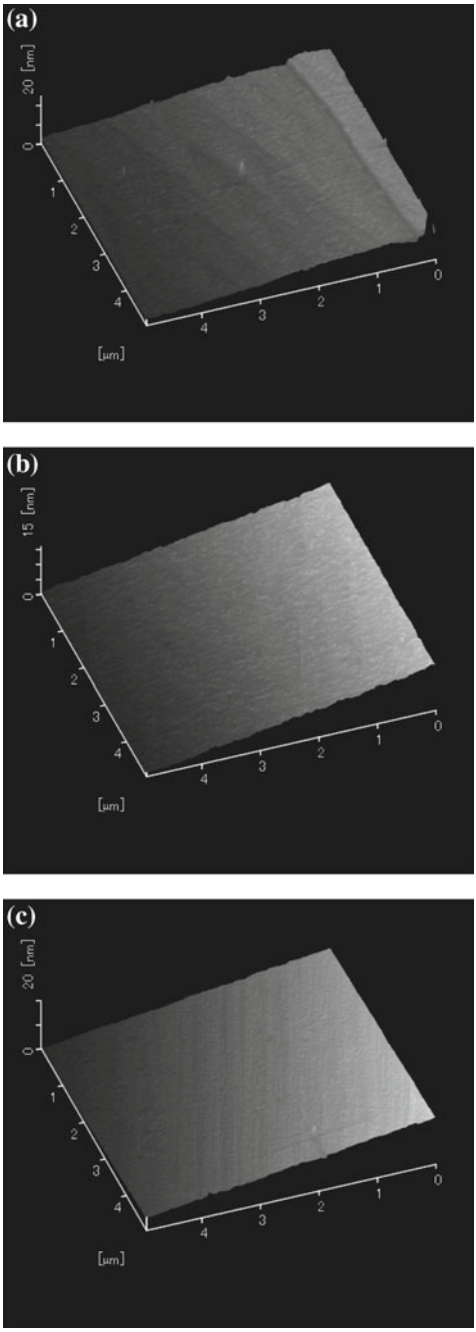

Fig. 3.17 AFM images of diamond (111) substrate. **a** Before, **b** after 30 min., and **c** after 60 min. etching

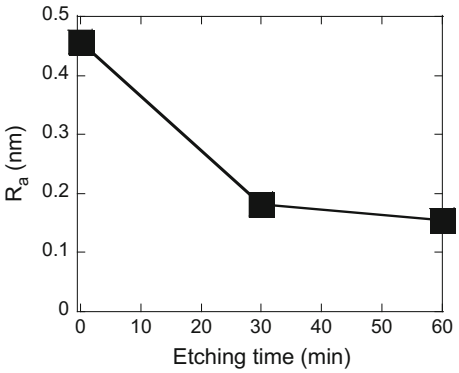

Fig. 3.18 Time dependence of R_a of diamond (111) substrate

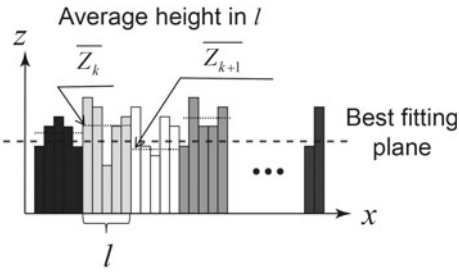

Fig. 3.19 Schematic of $R(l)$

$$R_a = \frac{1}{L}\int_0^L |z(x)|dx \cong \frac{1}{n}\sum_{i=1}^{n} |z(x_i)| \tag{3.7}$$

where $|z(x_i)|$ are the absolute deviations from the best-fitting plane, L is the evaluation length, dx is the spatial resolution of $z(x)$, and $n(= sL/dx)$ is the number of pixels in the measurement. Therefore, R_a provides information about the average value of the surface roughness for the entire region. In contrast, $R(l)$ provides much more information regarding the contributions of the surface roughness values at different length scales l to entire scanning region.

To compare the value of $R(l)$, near-field etching on plastic substrate was performed using light sources with both lower and higher photon energy than the absorption edge of O_2. For this purpose, Polymethyl methacrylate (PMMA) was used as for the etching [35]. Since the dissociation energy of O_2 is 242 nm (5.12 eV), the light source with lower and higher were selected as He-Cd laser with a wavelength of 325 nm (3.81 eV) and 5th harmonic YAG laser with a wavelength of 213 nm (5.82 eV, 20 Hz; pulse width 5 ns), respectively. Figure 3.20b, d show the respective AFM images after the near-field etching using the 325 nm light (etching time of 120 min.) and 213 nm light (etching time of 5 min.). By comparing the value of R_a, surface roughness was

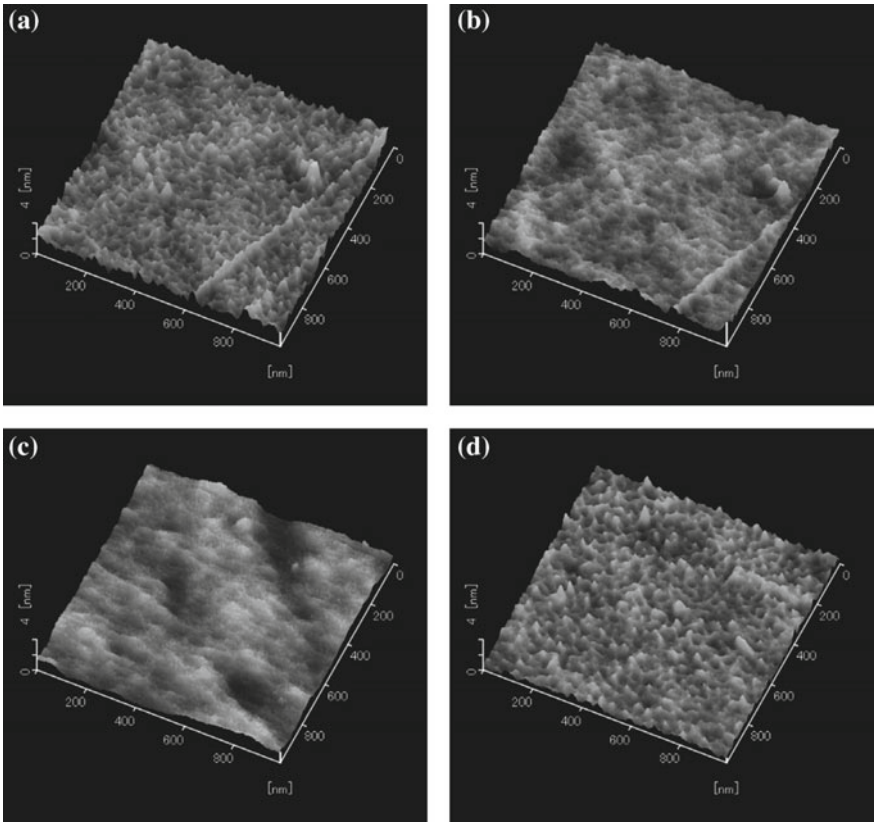

Fig. 3.20 AFM images. **a** Before etching for 325 nm etching. $R_a = 0.30$ nm. **b** After etching with 325 and 120 min. $R_a = 0.22$ nm. **c** Before etching for 213 nm etching. $R_a = 0.26$ nm. **d** After etching with 213 and 5 min. $R_a = 0.20$ nm

degreased from 0.30 to 0.22 nm (325-nm etching), and from 0.26 to 0.20 nm (213 nm etching).

Using those AFM data, $R(l)$ are plotted in Fig. 3.21. As shown in Fig. 3.21a, the 325 nm etching resulted in the decrease of l in the range of 5–100 nm, indicating the smaller scale component was decreased. In contrast, the 213 nm etching resulted in the decrease of l in the range of 100–1000 nm, indicating the larger scale component was decreased (Fig. 3.21a). By comparing those results, it was confirmed that the near-field etching using lower photon energy than the molecular dissociation energy etched the smaller scale protrusions selectively.

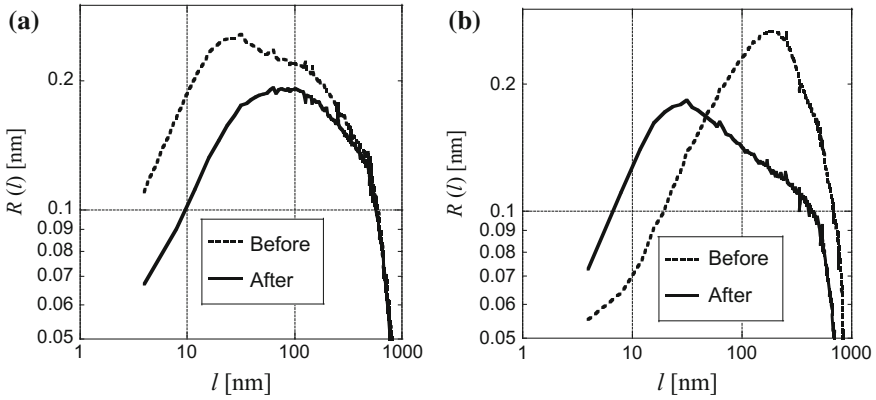

Fig. 3.21 Calculated $R(l)$ for **a** 325 nm etching and **b** 213 nm etching

3.3.2 Three Dimensional Structures

Near-field etching is a non-contact method, therefore, it can be applicable not only to the flat surface but also side wall of the three dimensional structures [35]. Recent progress of the diamond device, selective lateral growth of n-type diamond has been achieved on the side wall of the p-type diamond mesa structure [36]. However, since the diamond mesa structures are fabricated using the dry etching, the side wall has large corrugation due to the mask edge corrugation. To realize smooth side wall of the diamond mesa, the near-field etching was performed using O_2 gas and He-Cd laser (wavelength of 325 nm). Figure 3.22 shows the AFM images of before and after (30 min.) near-field etching, in which a high aspect ratio cantilever (SI-DF40H, Hitachi High-Technologies Corporation) was used so that the cantilever follow the side wall with a 2 μm height.

Figure 3.23a, b show the cross-sectional profiles along (a) x-direction and (b) y-direction indicated in Fig. 3.22. These figures reveled that the near-field etching drastically smoothed the side wall of the diamond mesa. In addition, the surface roughness Ra on both the top and bottom of the mesa drastically decreased using the near-field etching.

In thought the above results, it was confirmed that the near-field etching results in the decrease in the surface roughness. Such the modification of the surface is expected to improve the physical and/or chemical properties. To confirm this, the near-field etching was performed on the nanodiamonds (NDs) [37]. When the nitrogen vacancy (NV) in diamond has the minus charge (NV^-), the emission properties strongly depends on the environment parameters, including the magnetic field [38], the electric field, temperature, and so on. Since the diamond is non-toxic material, it is expected to utilize the implanted sensor. However, since the diamond is hard material and chemically inactive material, it is difficult to improve the surface properties especially in the case of NDs.

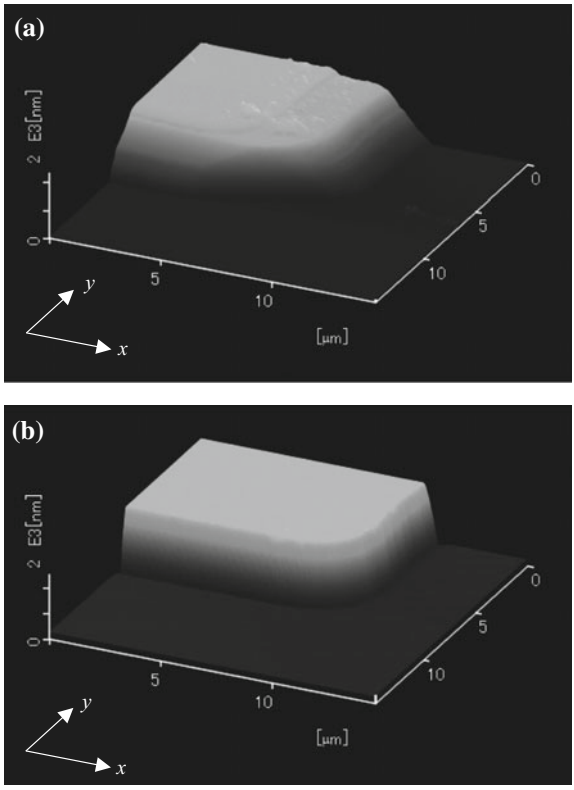

Fig. 3.22 AFM images of diamond mesa structure **a** before and **b** after near-field etching

The near-field etching on NDs with NV were performed using He-Cd laser with a wavelength of 325 nm. The NDs with a diameter of 100 nm were dispersed on the silicon substrate. Each ND contains 500 NV centers. Figure 3.24 shows the AFM images of NDs before and after near-field etching taken at the same position. From those comparison, the near-field etching resulted in the reduction of the NDs size.

To check the optical properties of NDs, the cathode luminescence (CL) spectra were obtained. All CL spectra were taken at −188°C. Figure 3.25 shows the typical CN of the NV, in which the peak 575 nm corresponds to the NV center (NV^0) [39]. Figure 3.25b shows the CL intensity ratio at 575 nm, normalized by the CL intensity before etching, as a function of etching time, indicating that the CL intensity increases as the etching time increased As can be seen in Fig. 3.24, the size of NDs decreased drastically, it is considered that the CL intensity of each NV increased. Thus, the CL intensity increase ratio per single NV center was plotted (Fig. 3.25c). From these results, the near-field etching resulted in 13.5 times increase of NV intensity.

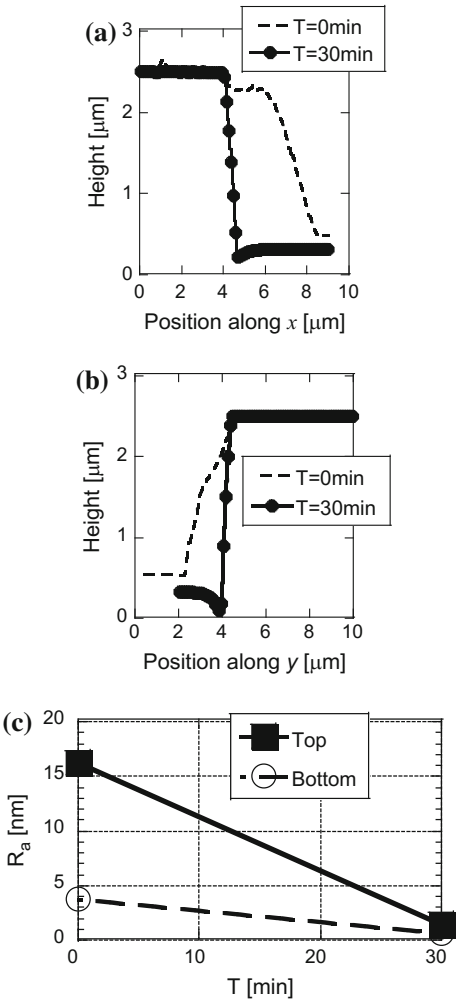

Fig. 3.23 Cross-sectional profiles along **a** x-direction and **b** y-direction indicated in Fig. 3.22. **c** Comparison of the value Ra on the top and the bottom of the mesa

3.3.3 Polarization Dependence

In this section, here is some results on the polarization dependence during the near-field etching [40]. For this purpose, ZrO_2 nano-stripe were prepared. The ZrO_2 nano-stripe patterns were prepared using the deep-ultraviolet (DUV) interferometric lithography method [41]. As is reported in the reference, this process uses a negative-tone resist based on photosensitive metal-oxo clusters, which are crosslinked and mineralised using DUV laser irradiation. Zirconium (IV) propoxide ($Zr(OPr)_4$) was used as a metal alkoxide, and methacrylic acid (MMA) was used as a ligand to form a metal complex, with a molar ratio of Zr:MAA = 1:8. Water and isopropanol were added to adjust the physico-chemical properties of the resist. DUV irradiation

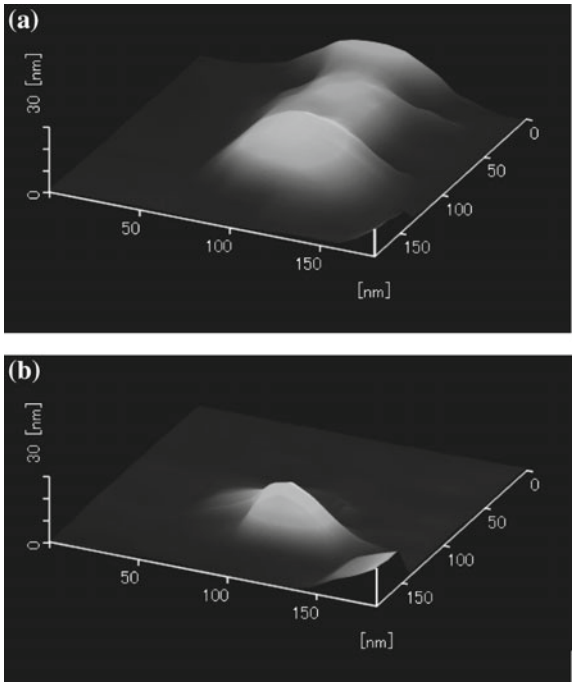

Fig. 3.24 AFM images of NDs **a** before and **b** after near-field etching

led to the cross-linked structure to form ZrO_2, after treatment of the non-exposed part with cyclohexanone [42]. From AFM images, the nano-stripe had a period of 598.4 ± 14.7 nm and a pre-etched width, w_b, of 438.1 ± 13.0 nm. For those ZrO2 nanostripe, near-field etching was performed using He-Cd laser with a wavelength of 325 nm. To obtain the polarization dependence, the incident light polarisation was controlled with a half waveplate. Figure 3.26 shows the cross sectional profiles obtained from AFM images. To find the difference on the polarization, the height difference between before and after the cross-sectional profiles. The dashed curves in Fig. 3.27 show the height difference. From those results, it was found that the height difference depend on the polarization.

To determine the etching-property dependence on the polarization, the electric and magnetic field distributions were calculated using a finite-difference time-domain (FDTD) method. Incident beam with an uniform field was irradiated from 600 nm from the top surface of the ZrO_2 structure (the refractive index of ZrO_2 was 1.8) [42]. The peak intensity of the incident electric-field was set to 1 [V/m]. As the ZrO_2 nanostripe, a periodic land- and space structure with 50-nm height, w-nm land width, and 100 nm spacing was used (see Fig. 3.28).

Figure 3.29 shows the FDTD results for $w = 400$ nm.

As shown in Fig. 3.29, the electric field localized at the corners of the stripe (Fig. 3.29a), which is reasonable that electrons are trapped at the corner in x-polarization. These distributions does not explain the results of height difference for

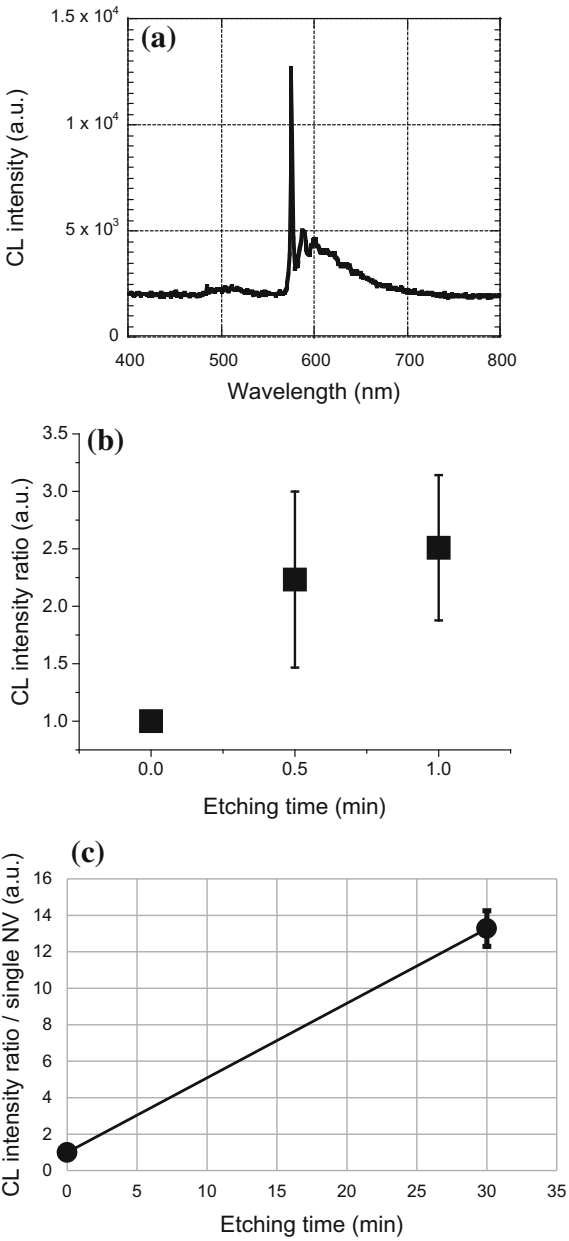

Fig. 3.25 **a** CL spectrum. **b** CL intensity ratio as function of etching time. **c** Normalized CL intensity

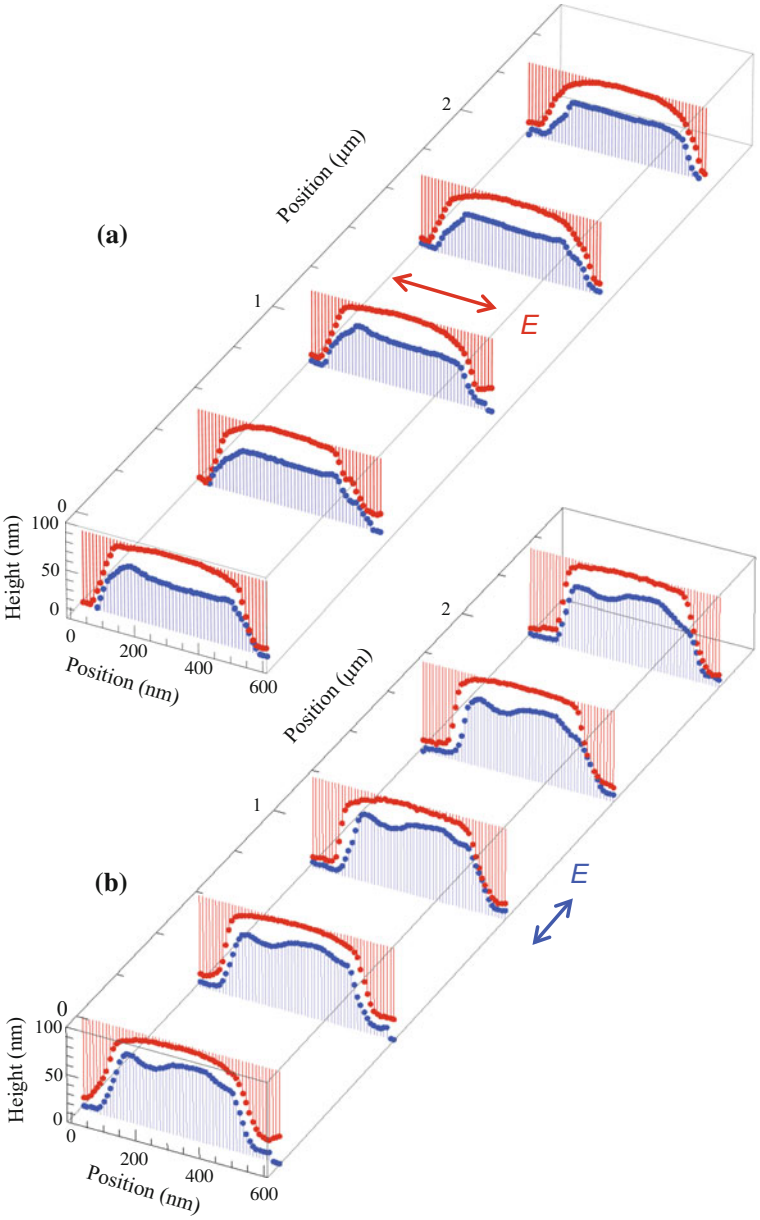

Fig. 3.26 Polarization dependence of the surface profiles. **a** Perpendicular polarization. **b** Parallel polarization. *Red profile* before etching, *Blue profile* after etching

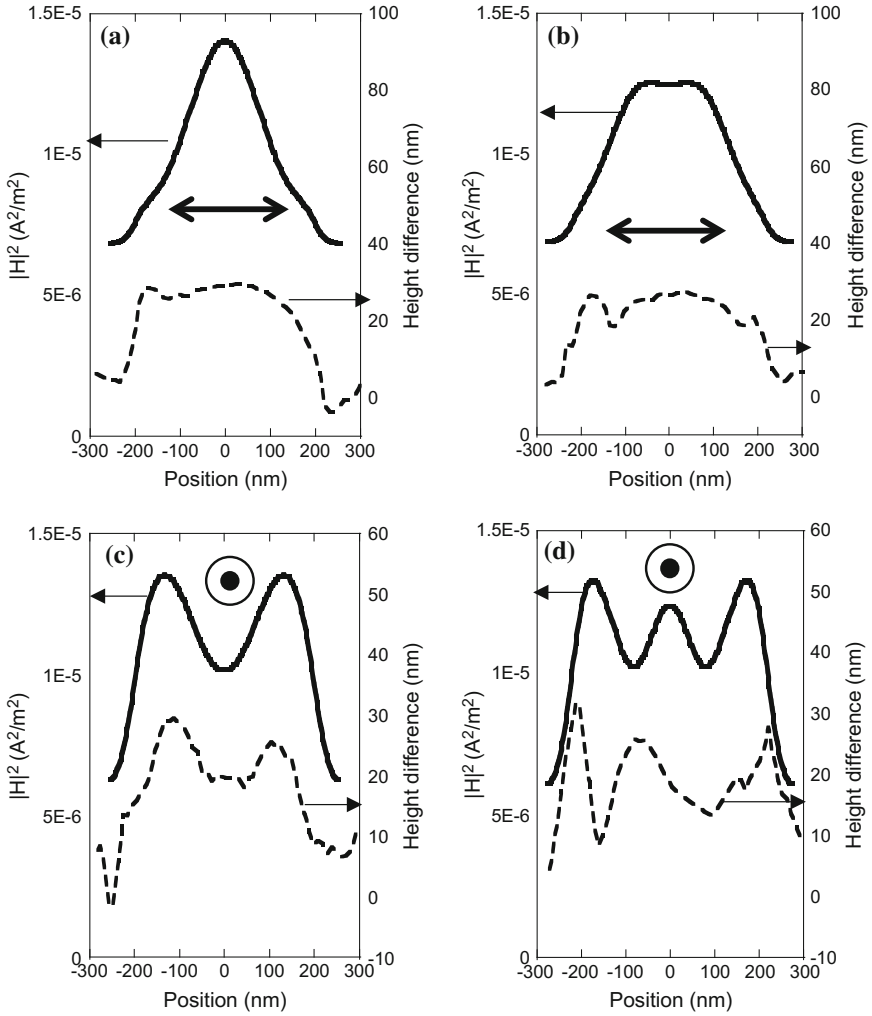

Fig. 3.27 Polarization dependence of the surface profiles. **a** and **b** x-polarization. The calculated w and the pre-etching widths, w_b, are **a** 410 and 411.17 and **b** 450 and 454.45 nm, respectively. **c** and **d** y-polarization. w and w_b with y-polarisation are **c** 410 and 414.06 and **d** 450 and 445.11 nm, respectively. w is used in FDTD calculation. *Solid curves* correspond to the calculated magnetic field intensity. *Dashed curves* correspond to the height difference obtained from Fig. 3.26

x-polarization (see dashed lines in Fig. 3.27a, b. In contrast, note that the magnetic field distributions change depends on the polarization. Therefore, the cross-sectional profiles are plotted as solid lines in Fig. 3.27. By comparing the magnetic field distributions and height difference, it is reasonable to consider the near-field etching on the nanostripes strongly depended on not the electric field but the magnetic field. As described in the above, the near-field etching originated from the radical oxygen

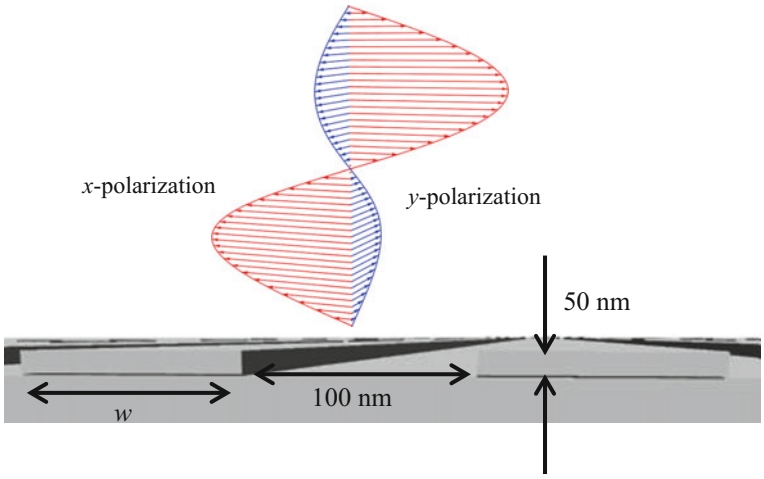

Fig. 3.28 Schematic model of FDTD calculation

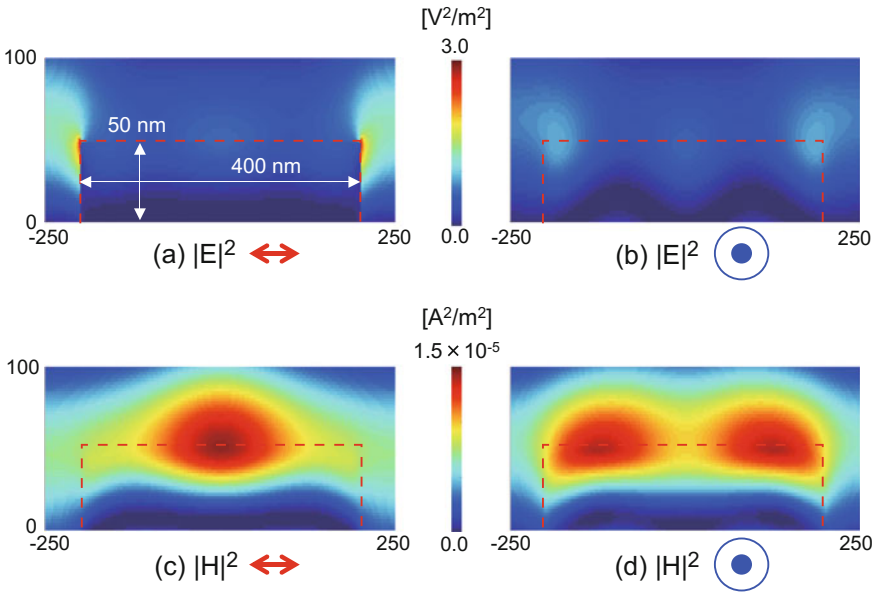

Fig. 3.29 FDTD results of the field distributions for $w = 400$ nm. **a** Electric field ($|E|^2$) distribution with a x- polarization. **b** $|E|^2$) distribution with a y-polarization. **c** Magnetic field ($|H|^2$) distribution with a x- polarization. **d** $|H|^2$ distribution with a y-polarization. *Red solid lines* corresponds to the ZrO_2 surface

species dissociated from the O_2 molecules. The optical near-field induces not only an electric dipole transition, but also an optically forbidden transition including the magnetic dipole and magnetic quadrupole transitions, along with other higher-order transitions. In other words, the optical near-field allows activation of the optically inactive intermediate states [43, 44]. Since O_2 has intermediate states with dipole forbidden [45, 46], the near-field etching might proceeded with the multi step transition via those dipole forbidden transition. Since the optical near-field inherently generate magnetic dipole moment due to the nonuniform field distributions [7], which also accelerate the dissociations.

3.4 Summary

In this chapter, the new type of the chemical reaction based on the optical near-field was reviewed. Such a near-field assisted photodissociation process can also be enhanced when the structure is fabricated using a near-field assisted fabrication process [47]. Therefore, further increases in photodissociation of molecules including CO_2, Cl_2, and O_2, are expected.

As for the application of CO_2 reduction, oxygen vacancies on ZnO have been proposed to be the catalytically active sites for methanol synthesis on pure ZnO [48–51]. In addition, hydrogen coverage of oxygen vacancies on ZnO is expected to accelerate methanol synthesis. Therefore, further increase in the CO_2 reduction rate will be expected using hydrogen annealing on the ZnO nanorods.

Through the near-field etching experiments, it was found evidence of the strong magnetic-field interaction with the material excitation. Since conventional nano-scale fabrication is based on the electric field [52, 53], the usage of the magnetic field will provide an additional degree of freedom during the fabrication of future optical and/or electrical device structures on the nano-scale.

Acknowledgments The author thanks to Mr. M. Yamaguchi (University of Tokyo) for his supports for theory of the optical near-field. The author thank Mrs. Etsuko Ota (University of Tokyo) for the AFM measurements. The author express sincere thanks to Prof. M. Ohtsu (Research Origin for Dressed Photon), Dr. T. Kawazoe (Univ. of Tokyo), Dr. W. Nomura (Kyusyu Univ.), and Mr. R. Nagumo, Mr. F. Brandenburg (Univ. of Tokyo) for their discussions and collaborations on the near-field etching. The author express sincere thanks to Dr. T. Iwasaki and Prof. M. Hatano (Tokyo Institute of Technology), Drs. S. Yamasaki, D. Takeuchi, T. Makino, H. Kato, and M. Ogura (National Institute of Advanced Industrial Science and Technology), F. Jelezko (Ulm University) for their discussions and collaborations on the diamond experiments. The author thank Drs. F. Stehlin, O. Soppera (Institut de Sciences des Materiaux de Mulhouse) for the nano-stripe sample preparation. The author express sincere thanks to Prof. G.-C. Yi (Seoul National University) for his discussions and collaborations on the ZnO nanorod growth. This work was partially supported by a MEXT Grant-in-Aid for Scientific Research (B) (No. 26286022, No. 25288012), a MEXT Grant-in-Aid for Scientific Research on Innovative Areas (No. 15H00866), a MEXT Nanotechnology Platform (No.12024046), the JSPS Core-to-Core Program (A. Advanced Research Networks).

References

1. T. Kawazoe, K. Kobayashi, J. Lim, Y. Narita, M. Ohtsu, Phys. Rev. Lett. **88**, 067404 (2002)
2. T. Yatsui, S. Sangu, T. Kawazoe, M. Ohtsu, S.J. An, J. Yoo, G.-C. Yi, Appl. Phys. Lett. **90**, 223110 (2007)
3. T. Yatsui, S. Takubo, J. Lim, W. Nomura, M. Kourogi, M. Ohtsu, Appl. Phys. Lett. **83**, 1716 (2003)
4. P.K. Jain, D. Ghosh, R. Baer, E. Rabani, A.P. Alivisatos, Proc. Natl. Acad. Sci. **109**, 8016 (2012)
5. S. Tojo, T. Fujimoto, M. Hasuo, Phys. Rev. A **71**, 012507 (2005)
6. M. Ohtsu, Nanophotonics **1**, 83 (2012)
7. M. Yamaguchi, K. Nobusada, T. Kawazoe, T. Yatsui, Appl. Phys. Lett. **106**, 191103 (2015)
8. M. Yamaguchi, K. Nobusada, T. Yatsui, Phys. Rev. A **92**, 043809 (2015)
9. A. Fujishima, K. Honda, Nature **238**, 37 (1972)
10. Z. Zou, J. Ye, K. Sayama, H. Arakawa, Nature **414**, 625 (2001)
11. X. Wang, K. Maeda, A. Thomas, K. Takanabe, G. Xin, J.M. Carlsson, K. Domen, M. Antonietti, Nat. Mater. **8**, 76 (2009)
12. T. Yatsui, T. Imoto, T. Mochizuki, K. Kitamura, T. Kawazoe, Sci. Rep. **4**, 4561 (2014)
13. W.I. Park, G.C. Yi, M.Y. Kim, S.J. Pennycook, Adv. Mater. **15**, 526 (2003)
14. K. Kitamura, T. Yatsui, M. Ohtsu, G.-C. Yi, Nanotechnology **19**, 175305 (2008)
15. A.J. Bard, M.S. Wrighton, J. Electrochem. Soc. **124**, 1706 (1977)
16. B.N. Chichkov, C. Momma, S. Nolte, F. von Alvensleben, A. Tunnermann, Appl. Phys. A **63**, 109 (1996)
17. Z. Zou, J. Ye, K. Sayama, H. Arakawa, Nature **414**, 625 (2001)
18. M.A.A. Clyne, B.A. Thrush, Proc. Roy. Soc. Lond. A **269**, 404 (1962)
19. N. Tanjeem, T. Kawazoe, T. Yatsui, Sci. Rep. **3**, 3341 (2013)
20. J. De Paula, P. Atkins, *Atkins' Physical Chemistry*, Ninth edn. (Oxford University Press, 2010)
21. http://www.hitran.org/
22. T.G. Slanger, G. Black, J. Chem. Phys. **54**, 1889 (1971)
23. T.G. Slanger, G. Black, J. Chem. Phys. **68**, 1844 (1978)
24. R.P. Wayne, J. Geophys. Res. **98**, 13119 (1993)
25. E.C.Y. Inn, J.M. Heimerl, J. Atmosp. Sci. **28**, 838 (1971)
26. Z. Chen, F. Liu, B. Jiang, X. Yang, D.H. Parker, J. Phys. Chem. Lett. **1**, 1861 (2010)
27. W.B. DeMore, M. Mosesman, J. Atmosp. Sci. **28**, 842 (1971)
28. T. Yatsui, K. Hirata, W. Nomura, Y. Tabata, M. Ohtsu, Appl. Phys. B **93**, 55 (2008)
29. R. Kullmer, D. Bauerle, Appl. Phys. A **43**, 227 (1987)
30. T. Yatsui, F. Stehlin, O. Soppera, W. Nomura, T. Kawazoe, M. Naruse, M. Ohtsu, Beilstein J. Nanotechnol. **4**, 875 (2013)
31. T. Yatsui, K. Hirata, Y. Tabata, W. Nomura, T. Kawazoe, M. Naruse, M. Ohtsu, Nanotechnology **21**, 355303 (2010)
32. D. Keilin, E.F. Hartree, Nature **165**, 543 (1950)
33. T. Yatsui, W. Nomura, M. Naruse, M. Ohtsu, J. Phys. D **45**, 475302 (2012)
34. D.W. Allan, Proc. IEEE **54**, 221 (1966)
35. T. Yatsui, W. Nomura, M. Ohtsu, Adv. Opt. Technol. **2015**, 701802 (2015)
36. H. Kato, T. Makino, M. Ogura, N. Tokuda, H. Okushi, S. Yamasaki, Appl. Phys. Express **2**, 055502 (2009). (T. Yatsui, et al. 2014)
37. R. Nagumo, F. Brandenburg, A. Ermakova, F. Jelezko, T. Yatsui, Appl. Phys. A **121**, 1335 (2015)
38. L.P. McGuinness, Y. Yan, A. Stacey, D.A. Simpson, L.T. Hall, D. Maclaurin, L.C.L. Hollenberg, Nat. Nano. **6**, 358 (2011)
39. B. Burchard, A.M. Zaitsev, W.R. Fahrner, A.A. Melnikov, A.V. Denisenko, V.S. Varichenko, Diam. Relat. Mater. **3**, 947 (1994)
40. T. Yatsui, T. Tsuboi, M. Yamaguchi, K. Nobusada, S. Tojo, F. Stehlin, D. Bloch, Light Sci. Appl. **5**, e16054 (2016)

41. H. Ridaoui, F. Wieder, A. Ponche, O. Soppera, Nanotechnology **21**, 065303 (2010)
42. F. Stehlin, F. Wieder, A. Spangenberg, J.-M. Le Meins, O. Soppera, J. Mater. Chem. C **2**, 277 (2014)
43. T. Feng, Y. Zhou, D. Liu, J. Li, Opt. Lett. **36**, 2369 (2011)
44. S.M. Hein, H. Giessen, Phys. Rev. Lett. **111**, 026803 (2013)
45. P.H. Krupenie, J. Phys. Chem. Ref. Data **1**, 423 (1972)
46. M. Mizushima, J. Phys. Soc. Jpn. **21**, 2335 (1966)
47. T. Yatsui, W. Nomura, M. Ohtsu, Nano Lett. **5**, 2548 (2005)
48. J. Kiss, A. Witt, B. Meyer, D. Marx, J. Chem. Phys. **130**, 184706 (2009)
49. J. Kiss, J. Frenzel, N.N. Nair, B. Meyer, D. Marx, J. Chem. Phys. **134**, 064710 (2011)
50. J. Kiss, J. Frenzel, B. Meyer, D. Marx, J. Chem. Phys. **139**, 044705 (2013)
51. J. Frenzel, D. Marx, J. Chem. Phys. **141**, 124710 (2014)
52. W.A. Challener, C. Peng, A.V. Itagi, D. Karns, W. Peng, Y. Peng, E.C. Gage, Nat. Photon. **3**, 220 (2009)
53. N. Fang, H. Lee, C. Sun, X. Zhang, Science **308**, 534 (2005)

Chapter 4
Nanophotonics-Based Self-optimization for Macro-optical Applications

Naoya Tate

Abstract Self-assembly is an alternative approach for implementation of nanophotonic devices and systems. In this chapter, we focus on *nanophotonic droplets* and *nanphotonics-based spatial light modulators* as typical outcomes of the nanophotonics-based self-assembly. The former realizes aligned structure of quantum dots and the corresponding high-yield optical energy conversion, and the latter realizes optimized distribution of dopants in a base material and the corresponding novel electrooptical property.

4.1 Introduction

4.1.1 Self-assembly for Nanometric-Fabrication

Recent developments in electronics and optoelectronics have fundamentally relied on the evolution of micro-fabrication technologies. In particular, in the field of optoelectronics and its related technologies, micro-scale components are part of micro-scale applications and devices such as light detectors, light emitters, waveguides, mirrors, and MOEMS (micro-optoelectro mechanical systems), as well as larger optoelectronic applications and devices such as hard disks, read/write systems for hard disks, solar cells, and flat-panel displays. Moreover, in recent years, the scaling of micro-fabrication to *around sub-50* nm dimensions has been applied practically through conventional micro-fabrication technologies [1], such as utilization of scanning probe [2], extreme ultra-violet (UV) light [3], electron-beam [4], X-ray [5], or ion-beam [6]. Currently, for further developments of electronics and optoelectronics, the architectural and material requirements in nano-scale manufacturing are higher.

N. Tate (✉)
Faculty of Information Science and Electrical Engineering, Kyushu University,
744 Motooka, Nishi-ku, Fukuoka 819-0395, Japan
e-mail: tate@ed.kyushu-u.ac.jp

M. Ohtsu and T. Yatsui (eds.), *Progress in Nanophotonics 4*,
Nano-Optics and Nanophotonics, DOI 10.1007/978-3-319-49013-7_4

Currently, a number of technologies are being developed for *less-than sub-50 nm* dimension fabrication, referred to as *nano-fabrication* in this chapter, through the extension of conventional micro-fabrication technologies. Thus, most of these approaches are based on the concept of *top-down* processing. The basic concept of top-down fabrication can be explained using an analogy of sculpting a structure from a block of stone, where a piece of a base material is gradually pruned until it reveals the desired structure. Here, because the resolution of such the top-down processing fundamentally depends on tools for the sculpting, simple downscaling of conventional concepts for establishment of nano-fabrication may not be able to fulfill the many requirements for practical use, such as realization of three-dimensional structures with nanometric precision by parallel and cost-effective processing for mass-production. In contrast, *bottom-up* processing has the potential to fulfill many of the above requirements. The analogy of bottom-up fabrication can be given as the construction of a structure by using pieces of blocks, where the ideal precision of such processing depends on the size of each block. Current technologies allow for controlling atoms or molecules, and these can be used for *blocks* for bottom-up fabrications. Thus, sufficient nano-fabrication precision can be achieved.

In particular, self-assembly [7] is an alternative approach that is based on concept of the bottom-up processing. A self-assembling process consists of individual interactions between each component in a setup. As statistical results of interactions, such components spontaneously construct higher-order structures according to a pre-defined draft. The pre-defined draft is arbitrarily designed so that desired structures, such as patterns, objects, and functional systems, are constructed from prescribed components. For example, as explicitly demonstrated using DNA origami [8], the molecular scale of self-assembly realizes arbitrary 3D structures with sub-nanometer precision through parallel processing. The important aspect of the design of a pre-defined draft is the definition of individual interactions between each component and external physical control in order to ensure appropriate guidance of the subsequent processes. In general, the components and potential energy of a normal physical system are frequently dissipated and homogenized, with the induction of such external control leading the physical system to converge to an appropriate constant state. In the case of the DNA origami and related studies, the pre-defined draft defined the control of complementary bonding between appropriately designed DNA sequences through various external controls, such as addition of heat, lights, and enzymes.

4.1.2 Nanophotonics for Self-assembly

The field of nanophotonics research has also seen rapid progress in recent years, and various elemental theories and practical technologies have been actively established [9]. Nanophotonics exploits the local interactions between light and materials via optical near fields, which are induced by the incidence of light. Several characteristic phenomena due to the induction of optical near fields can be well described by the definition of a dressed photon (DP). A DP is defined as a quasi-particle represent-

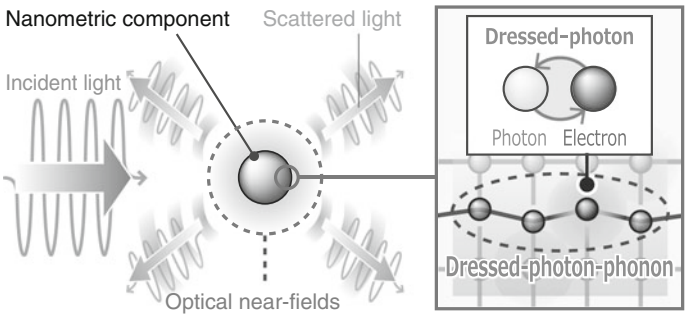

Fig. 4.1 Schematic description of optical near-fields, DP, and DPP

ing the coupled state of a photon and an electron in a nanometric space of material, as shown schematically in Fig. 4.1 [10]. Owing to the coupling, DP is allowed to excite a multi-mode coherent phonon in the material. Thus, the energy states of DPs and excited coherent phonons can be collectively identified as the so-called dressed-photon–phonon (DPP) state [11–14].

One of the fundamentally important aspects of DPP is that the energy state physically behaves as an intermediate state during the electronic excitation and relaxation process. This means that processing of multistep electronic transitions and corresponding electo-optical functions are allowed to occur. While similar phenomena, such as Raman scattering [15] and multi-photon absorption [16], utilize *virtual states* during their electronic transitions, phonon states and corresponding DPP states are surely *real states*. Therefore, when utilizing DPP states, a much higher yield of transitions is available. In fact, by utilizing a feature of DP called *phonon-assisted transition*, various experimental demonstrations such as high-yield optical emission via upper-conversion of induced optical energy [12, 17] and high-intensity emission from indirect transition type semiconductors [13, 14, 18] have been successfully reported.

Here, we describe the basics of self-assembly utilizing characteristics of DP and DPP. The conceptual sequence is schematically shown in Fig. 4.2.

As shown,

1. According to a pre-defined draft, nanometric components, which behave as sources of DP and DPP, are appropriately implemented to target material.
2. Optical near-fields and corresponding interactions are induced by the incidence of light to the material.
3. Local transformation of the physical property occurs as a result of characteristics of DP and DPP. At the same time, local-scales of electrooptical functions are obtained.

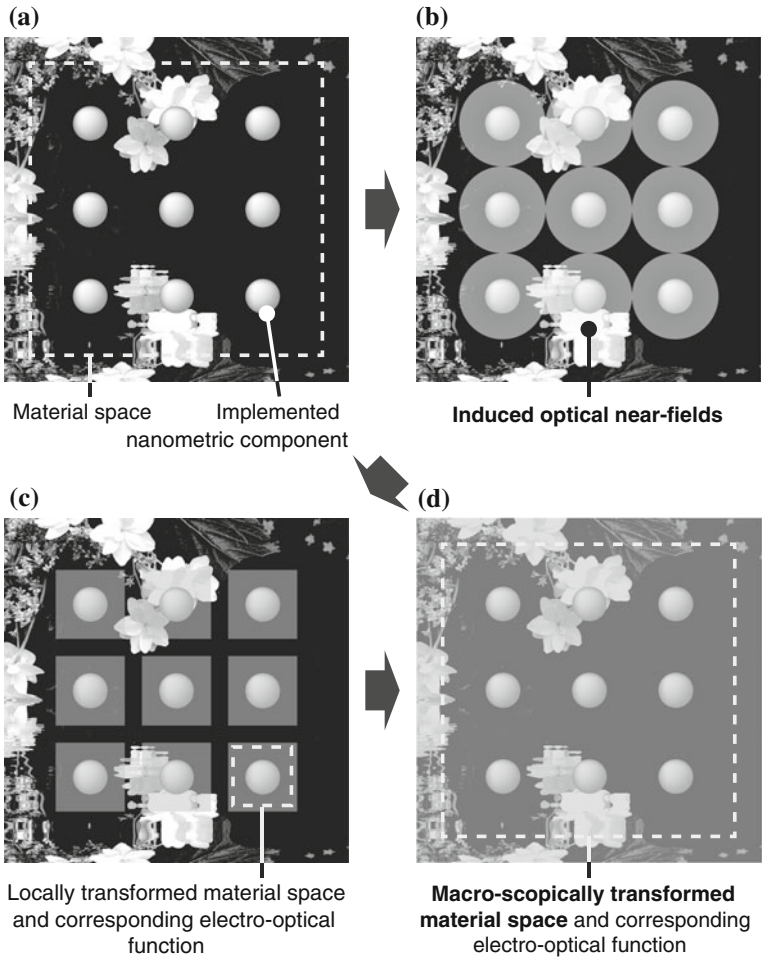

Fig. 4.2 **a**–**d** Conceptual procedure of self-assembly of electrooptical function utilizing characteristics of DP and DPP

4. After subsequent processes, transformation of physical property is extended to the macro-scale material space, and corresponding electrooptical functions are utilized for macro-scale applications.

Here, the sequence (a)–(d) is preferred to be processed by self-assembly with a few external controls. Similar to conventional self-assembly techniques briefly introduced in Sect. 4.1.1, the design of the pre-defined draft includes design of a material space with addition of nanometric components and external controls.

4.2 Nanophotonic Droplet

4.2.1 Nanometric Alignment for Optical Energy Transfer

Novel electrooptical systems for the next generation are expected to become possible by using novel photonic devices. M. Ohtsu has proposed the concept of nanophotonic devices. A nanophotonic device is defined as a novel device with a novel optical function, which is operated by the transferring of the local energy between nanometric components via induced optical near-fields [19]. In such a device, local energy transfer and its subsequent dissipation are encoded as processing of nanometric optical information. The important aspect is that such processing is possible only by utilizing optical near-field interactions between their components.

The basic mechanism of the energy transfer is typically represented by multiple QDs [20]. QDs are nanoscale semiconductor particles that tightly confine either electrons or electron holes in all three spatial dimensions. They can be prepared via several possible routes, including colloidal synthesis, plasma synthesis, or mechanical fabrication. Their electronic properties fall between those of bulk semiconductors and those of discrete molecules of comparable size, and their optoelectronic properties, such as band gap, can be tuned as a function of particle size and shape for a given composition. The assemblage of QDs exhibits a variety of interactions, such as carrier tunneling [21–23], Coulomb coupling [24, 25], and spin interaction [26], which can be applied to develop novel functional devices. Here, the optical near-field interaction is also one of the interactions mediated by localized energy fields that enables excitation energy transfer between QDs [27–29]. Many approaches have been used to clarify the excitation energy transfer via the optical near-field interaction between QDs as well as particles and microcrystals of various materials.

In these QDs, the quantized Z_3 exciton energy level is represented by quantum numbers (n_x, n_y, n_z) [30]. In general, the exciton energy levels with even quantum numbers are known as dipole-forbidden states [30, 31]. It based on long-wavelength approximation, which is due to homogeneous distribution of optical intensity through the incidence of light in each QD, and thus, optical energy transfer to such levels is not allowed. However, as schematically shown in Fig. 4.3, because induced optical near-fields exhibit a steep gradient of their distributions, the long-wavelength approximation cannot be applied, and the optical near-field interaction enables the energy transfer between these energy levels due to the spatially localized nature of the optical near field [20, 28, 29, 32].

While basic specifications of optical near-field interactions, such as amounts and stabilities, depend on the structures and conformations of nanometric components, precise assemblage of the nanometric components is a fundamental issue in the implementation of nanophotonic devices and systems.

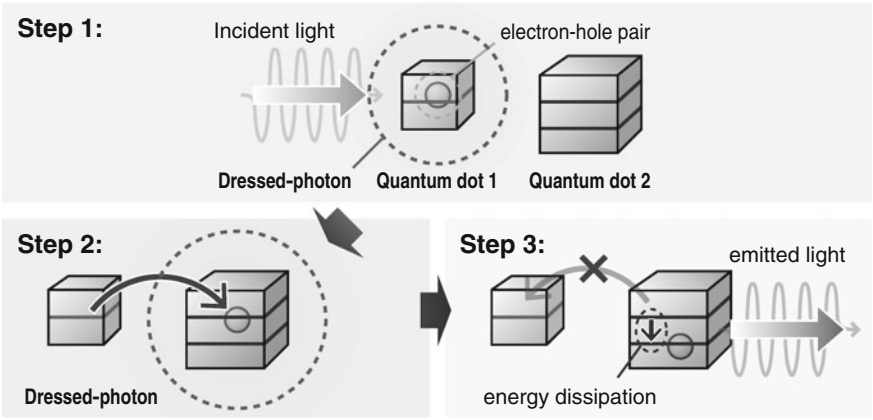

Fig. 4.3 Schematic description of energy transfer between two QDs via optical near-field interactions

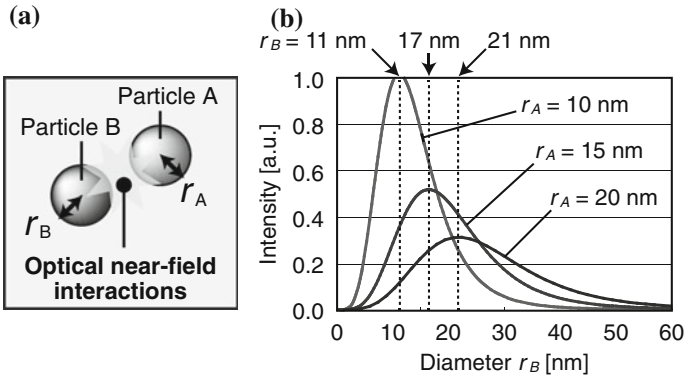

Fig. 4.4 **a** Schematic diagram of optical near-field interactions between two nanometric particles, and **b** intensity of optical near-field interactions between particles of various sizes

4.2.2 Size Resonance-Based Nanometric Coupling

To design a pre-defined draft for the self-assembled coupling of nanometric components, we focused on the *size resonance effect* of optical near-field interactions [33]. Sangu et al. have analyzed the fundamental properties of optical near-fields in an ideal two-particle model, which numerically represents general nanometric systems, such as a probe-tip and a sample in the setup of optical near-field microscopy. An important aspect is the exciton-polariton representation of interactions between the particles. As schematically shown in Fig. 4.4a, by considering two particles, particle A and particle B, with diameters r_A and r_B, respectively, the intensity of optical near-field interactions, $I(d_{AB})$, between the two is given by

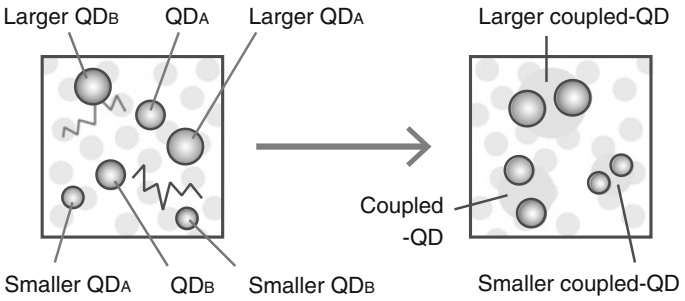

Fig. 4.5 Schematic diagram of size-selection in a mixture of various sizes of QDs

$$I(d_{\mathrm{AB}}) = A\left[r_{\mathrm{A}}^3 \frac{r_{\mathrm{B}}}{r_{\mathrm{A}}} \cosh\left(\frac{r_{\mathrm{B}}}{r_{\mathrm{A}}}\right) - \sinh\left(\frac{r_{\mathrm{B}}}{r_{\mathrm{A}}}\right) \times \left(\frac{1}{d_{\mathrm{AB}}} + \frac{r_{\mathrm{A}}}{d_{\mathrm{AB}}^2}\right) \times \exp\left(-\frac{d_{\mathrm{AB}}}{r_{\mathrm{A}}} - 1\right)\right]^2, \tag{4.1}$$

where d_{AB} is the distance between the two particles, and A is a proportionality constant. Figure 4.4b plots the normalized intensity of the optical near-field interactions in the cases where $r_{\mathrm{A}} = 10$, 15, and 20 nm. As shown, other particles with similar sizes, namely, $r_{\mathrm{B}} = 11$, 17, and 21 nm, respectively, are likely to produce more intense interactions.

As shown, similar sized particles induced a larger intensity of interactions, according to the size resonance effect, and, in this case, corresponding physical or chemical reactions due to the interactions are expected to occur. In other words, if the mixture solution contains various sizes of QDs, they can autonomously couple with suitable partners via induced interactions, as schematically described in Fig. 4.5.

At the same time, such coupled QDs are preferred combinations for induction of optical energy transfer, which is the fundamental aspect of nanophotonic devices and systems.

4.2.3 Phonon-assisted Photo-Curing Process

To physically maintain the coupled QDs in the preferred situation to induce optical near-field interactions between them, we proposed the *phonon-assisted photo-curing* method [34–37] based on nanometric local curing of the polymer material.

In general, the curing polymer is defined as a resin as a prepolymer in the viscous state that changes irreversibly into an infusible and insoluble material. Curing of the material is induced by applying appropriate external energies, such as heating or light radiation. Then, a cross-linking process between the resin molecules occurs. The cross-linking process forms rigid 3D structures, resulting in a material with a

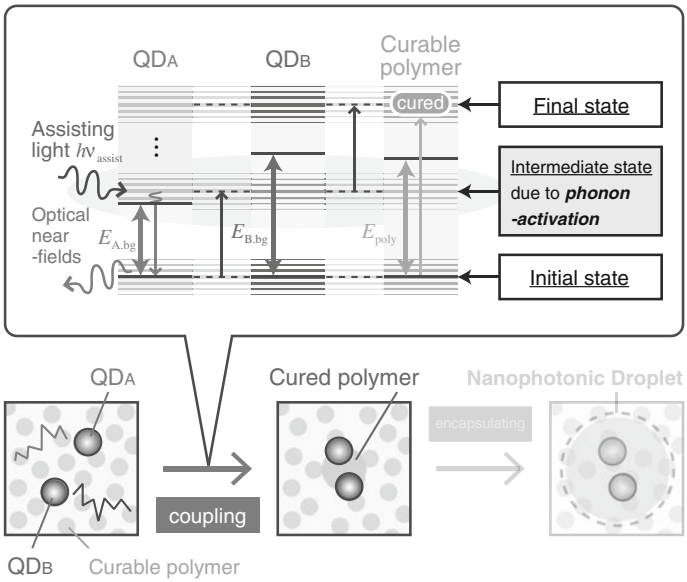

Fig. 4.6 Schematic diagram of the coupling process during the phonon-assisted photo-curing method

higher physical and chemical stability. As a result, a thermoset material cannot be melted and re-shaped after it is cured.

Here, we propose compensation of the activation energy of the curable polymer by the internal energy owing to the optical near-field interactions. In other words, the coupling process is induced only when a sufficient amount of interaction is induced such as in the case of size-resonanced QDs in Fig. 4.5. Therefore, the curing of the polymer material occurs only when the size-resonanced QDs are coupled with each other. Our method is divided into two steps, *coupling process* and *encapsulating process*, which are described in Figs. 4.6 and 4.7, respectively. In our method, we prepare a mixture solution containing two types of QDs, QD_A and QD_B, and a curable polymer. Mixture of the materials is irradiated with an assisting light having photon energy $h\nu_{\text{assist}}$. Here, $h\nu_{\text{assist}}$ must be lower than the activation energy of the curable polymer, represented as $E_{\text{poly.act.}}$; otherwise, all polymer materials are necessarily cured irrespective of whether the size-resonanced QDs are coupled. While the bandgap energies of QD_A and QD_B are represented as $E_{\text{A.bg.}}$ and $E_{\text{B.bg.}}$, respectively, when the energies satisfy the condition

$$E_{\text{A.bg.}} < h\nu_{\text{assist}} < E_{\text{poly.act.}} < E_{\text{B.bg.}}, \tag{4.2}$$

which corresponds to sufficiently compensate the external energy $h\nu_{\text{assist}}$, and the following process is subsequently induced:

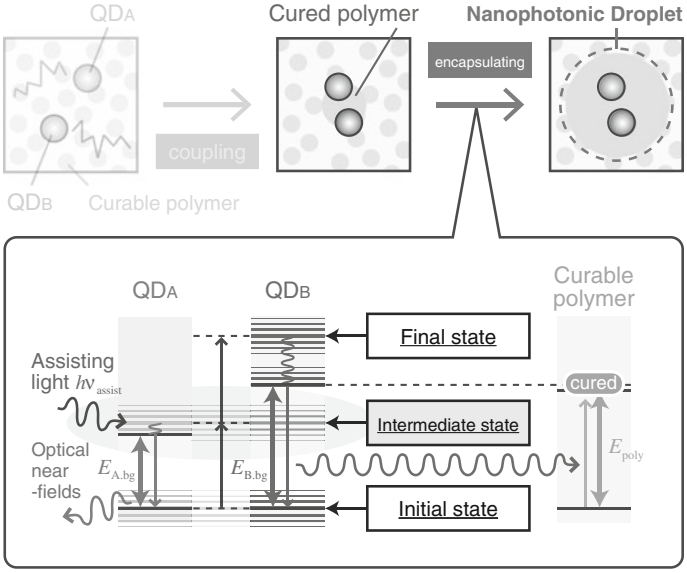

Fig. 4.7 Schematic diagram of the encapsulating process during the phonon-assisted photo-curing method

If the volume densities of QDs in the mixture are not sufficiently high and the QDs rarely encounter each other, only QD_A spontaneously emits visible light by absorbing the assisting light. In this case, no subsequent physical or chemical reactions occur. In contrast, if the density is sufficiently high that the QDs can frequently encounter each other, multistep energy excitation of the curable polymer occurs owing to optical near-field interactions between neighboring QD_A and QD_B, and the curable polymer is locally cured, as schematically shown in Fig. 4.6. This means that the encountered QDs are promptly coupled with each other by the locally cured polymers. As described in the previous section, such coupling processes are preferred to be induced between similar sizes of QDs due to the size-resonance effect. In addition, since the spatial distribution of the optical near-fields generated on the surface of the QDs is expressed by a Yukawa function [32], the separation between the two QDs is theoretically defined by the Yukawa function. Thus, homogeneous alignment of QDs with similar separations between similar sizes of QDs is expected to be realized.

Moreover, as schematically shown in Fig. 4.7, further irradiation with the assisting light induces multistep excitation of QD_B due to optical near-field interactions with the neighboring QD_A. Subsequently, QD_B spontaneously emits light with a higher photon energy than the assisting light, and the curable polymer in the surroundings is gradually cured by the absorption of the emitted light. As a result, the cured polymer encapsulates the coupled QDs, which are referred to as *nanophotonic*

droplets (simply described as *droplets* hereafter), ensuring sufficient stability of the QD combinations and the corresponding optical near-field interactions.

4.2.4 Experimental Demonstrations

To experimentally verify the proposed method, as well as the mechanism of wavelength conversion using the formed droplets, we used commercially available CdSe-QDs (Sigma-Aldrich, Lumidots) and CdS-QDs (NN-Labs, Nanocrystals) in toluene solutions as QD_A and QD_B, shown in Figs. 4.6 and 4.7, respectively, which emit visible light with wavelengths of 640 and 460 nm. The QD solutions were dispersed in a UV-curable polymer (TESK, A1867). To form the droplets, the mixture was irradiated with assisting light emitted from a 200 mW laser diode with a wavelength of 532 nm for 30 min. The total amount of the mixture was limited to 1.0 mL to maintain spatially uniform illumination of the assisting light in our experimental setup. As shown in Fig. 4.8, these experimental conditions fulfilled the previously described energy conditions for inducing the sequential process of the phonon-assisted photocuring method, as described in (4.2), where both the assisting light and emitted light from QDs are rarely absorbed by the polymer. Further, in this case, the upper conversion of the optical energy from visible light to UV light is expected. After irradiation with the assisting light, the mixture was separated into cured and un-cured solutions by centrifugation at 10,000 rpm for 5 min. Here, the extracted material, which was assumed to contain a large number of droplets, was dispersed in a toluene solution and uniformly spin-coated on a substrate.

Figure 4.9a shows a microscopic fluorescence image of droplets under UV light irradiation. As can be seen, a large number of locally cured polymer particles, referred to as nanophotonic droplets, are successfully mass-produced as expected. Moreover, as shown in the zoomed image and aggregated data in Fig. 4.9b, similar sizes of

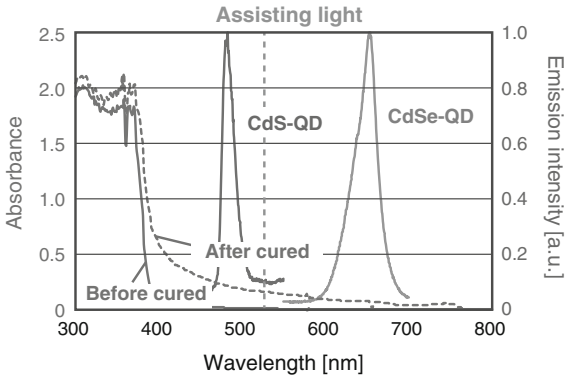

Fig. 4.8 Absorbance and emission spectra of UV-curable polymer and QDs

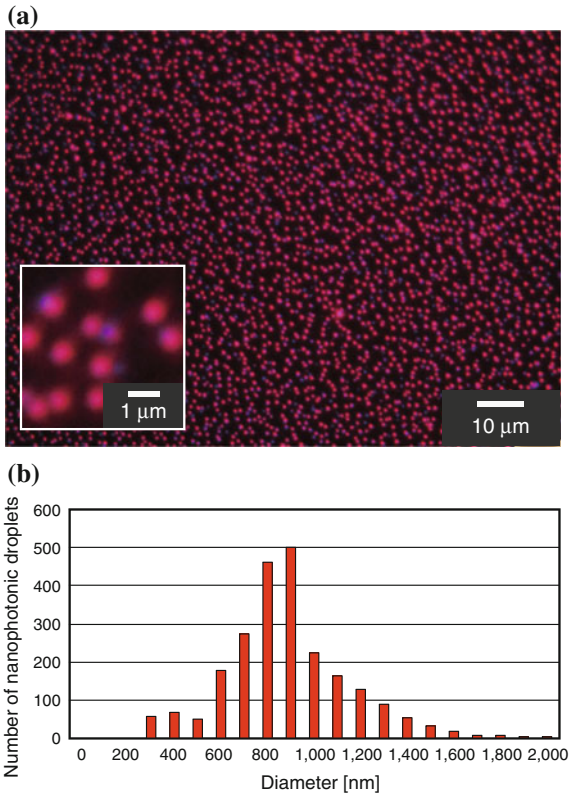

Fig. 4.9 **a** Microscope fluorescence image of densely formed droplets under UV light irradiation and zoomed image of droplets (*inset*). **b** Aggregated data of size distribution of mass-produced droplets

spherical structures with similar emissions are seen, where the diameters of the droplets are homogeneously lower than 1 μm.

Owing to the basics of the phonon-assisted photo-curing method, as schematically shown in Figs. 4.6 and 4.7, photo-curable polymers as well as thermo-curable polymers can be used as the base material of the droplets. For the demonstration, we used polydimethylsiloxane (PDMS) solution (Dow Corning Toray, Sylgard 184). PDMS is one of the most widely used silicon-based organic polymers, although it is generally an inert, non-toxic, and non-flammable material. In particular, owing to the transparency of PDMS to visible lights, emission from QDs in each droplets can be losslessly obtained at the outside of each droplet. Here, commercially available CdSe-QDs (Sigma-Aldrich, Lumidots) and CdS-QDs (NN-Labs, Nanocrystals), which emit visible light with wavelengths of 560 nm and 420 nm, respectively, in toluene solutions are mixed with the PDMS solution. To form the droplets, the mixture was irradiated with assisting light emitted from a 200 mW laser diode with a wavelength of 457 nm for 30 min. Other experimental conditions and procedures are similar to the previous demonstration using photo-curable polymers. As a result, the results obtained, shown in Fig. 4.10, were quite similar to those in Fig. 4.9.

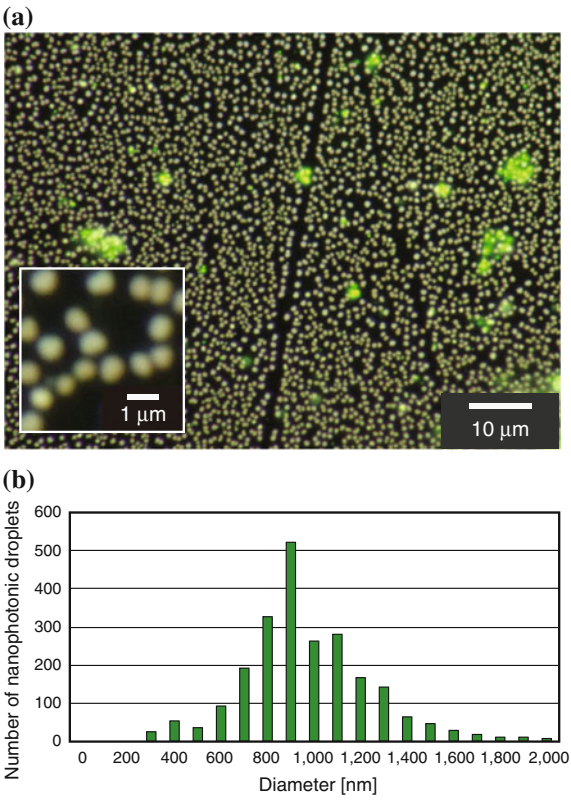

Fig. 4.10 **a** Microscope fluorescence image of densely formed droplets under UV light irradiation and zoomed image of droplets (*inset*). **b** Aggregated data of size distribution of mass-produced droplets

Here, the similarity between Figs. 4.9 and 4.10 indicates that such local curing of a curable polymer surely does *not* depend on the absorbance of the assisting lights, which induces conventional macroscopic photo-curing. In other words, the compensated energy due to optical near-field interactions and the corresponding excitation of phonons similarly contribute to the local curing of both types of polymers.

Because of the similarities in the sizes and emissions of droplets shown in Figs. 4.9 and 4.10, the number and the distribution of QDs in each droplet are assumed to be quite similar to each other. Moreover, as a result of the basic processes shown in Figs. 4.6 and 4.7, each droplet is expected to contain physically coupled QDs, which consist of CdSe-QDs as emitters and CdS-QDs as absorbers. Through such combination of the QDs, the optical energy absorbed by the CdS-QDs is preferentially transferred to the CdSe-QD before being emitting from it. Therefore, the emission from the CdSe-QD is expected to be enhanced. Related research that experimentally demonstrated the optical energy transfer between QDs and the corresponding emission enhancement has been previously reported by assuming a similar setup using aligned QDs [38].

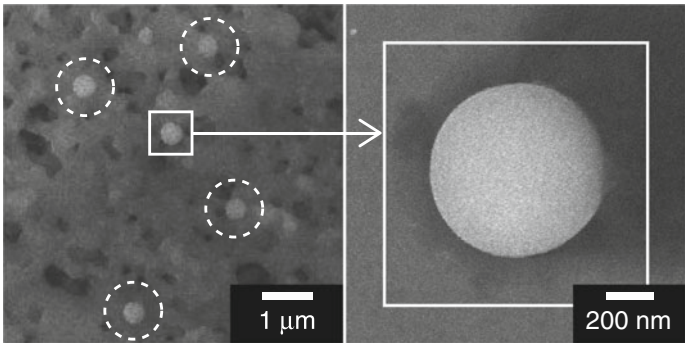

Fig. 4.11 SEM images of nanophotonic droplets

To verify these expectations, we focused on specification of an individual droplet. Here, we used commercially available CdSe-QDs (Ocean Optics, Evidot) and ZnO-QDs prepared by sol–gel synthesis using photo-induced desorption [39]. They emit visible lights with photon energies of 2.03 eV and 3.40 eV, respectively. The QD solutions were then dispersed in a UV-curable polymer (NORLAND, NOA 65) and irradiated with assisting light emitted from a 120 mW laser diode with a photon energy of 2.71 eV for 30 min. Other conditions and procedures for this experiment are similar to those in the previous demonstrations. Figure 4.11 shows an image of the droplets observed using scanning electron microscopy (SEM).

In this result, their diameter of droplets were less than 1 μm, as in the case of the results of the previous demonstrations. These droplets exhibit quite spherical structures. This is because of the basics of the encapsulating process, which is schematically shown in Fig. 4.7, where the upper converted optical energy is emitted from the ZnO-QD to various directions and absorbed by the surrounding polymers. The sizes of the droplets subsequently increases, and thus, spherical structures are successfully obtained as nanophotonic droplets. The sizes of the droplets are uniquely defined by the photon energies of the upper-converted lights and the absorbance of the polymer materials, and not by the intensity and irradiation time of the assisting light. Therefore, all droplets homogeneously reveal similar sizes.

Next, a droplet is cut by a focused ion beam (FIB), and the cross-sectional surface of the droplet is observed by using transmission electron microscopy (TEM), as shown in Fig. 4.12a.

Characteristic matter refers to the fact that the QDs contained in the droplets are aligned as homogeneous distributions with similar distances between each QD. As shown by the 1D profile of pixel values of the SEM image in Fig. 4.12b, the distances are unified as 4–5 nm, and this is equal to the size of the QDs. This confirms the contribution of optical near-field interactions during the coupling process, because the spatial distribution of optical near-fields and corresponding interactions are generally described by the Yukawa function [19], and their scales are defined to be similar to the size of the source of optical near-fields, which is the size of QDs in this case. As

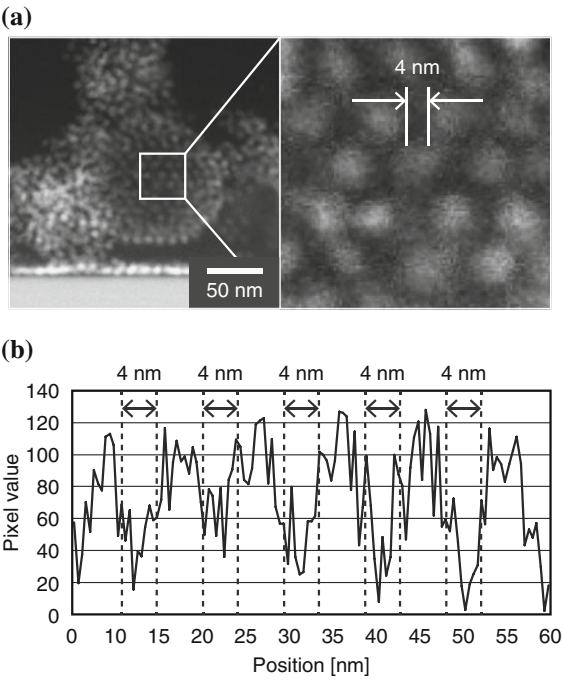

Fig. 4.12 **a** TEM images of cross-sectional surface of a nanophotonic droplet, and **b** a 1D profile of alignment of QDs in the droplet

the basis of our proposal, all droplets contain similar alignments of QDs, and hence, the optical energy transfer and corresponding emissions are similar among the QDs. In other words, this explains why all droplets reveal similar fluorescence properties, as shown in Figs. 4.9 and 4.10.

To compare multiple emission spectra of individual droplets, we constructed a 2D map of the emission spectra of samples obtained with a micro-spectrophotometer (NFGP-740, JASCO, Japan). The samples were irradiated by a laser diode with a photon energy of 3.06 eV. The spatial resolution of the experimental setup was expected to be less than 200 nm. Figure 4.13a shows a 2D emission image of the aggregated droplets A, B, C, and D. The inset represents a bright-field image under white-light illumination. The individual emission spectra of the droplets are respectively plotted in Fig. 4.13b.

As shown, the heights and widths of the emission spectra are quite similar to each other. Because they can be simply fitted by a single Lorentzian fitted curve, as represented by the black solid line in Fig. 4.13b, which is generally applied to approximate the emission spectrum of a single illuminant, it is considered that each droplet contains single CdSe-QDs of similar sizes and coupled ZnO-QDs. This result demonstrates the uniformity of the optical properties of mass-produced droplets as expected.

We also measured the collectively observed emission spectrum of multiple CdSe-QDs, as shown in Fig. 4.13b. The sample was prepared by mixing a solution of CdSe-

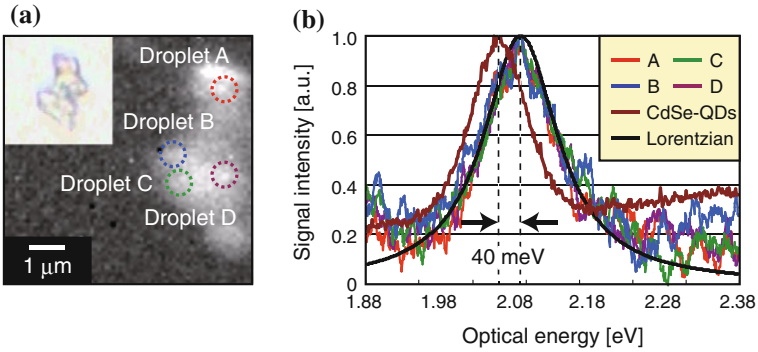

Fig. 4.13 **a** Obtained emission image of aggregated nanophotonic droplets. **b** Emission spectra of multiple nanophotonic droplets, collectively observed emission spectrum of CdSe-QDs, and a Lorentzian fitted curve

QDs and a UV-curable polymer, and was directly spin-coated on a substrate without any irradiation with assisting light. As shown, there was a 40 meV difference between the peak optical energy in the spectra of the individual nanophotonic droplets and the collective CdSe-QDs. Such difference is due to the re-absorption of emission within the collective CdSe-QDs as well as the size-selectivity during the coupling process between CdSe-QDs and ZnO-QDs. This result indicates that ZnO-QDs preferably coupled with smaller CdSe-QDs in the mixture and exhibited such uniformity in their emission spectra.

4.2.5 Dynamics of the Coupling Process

Because our phonon-assisted curing method is fundamentally induced by the optical near-field interactions between two heterogeneous QDs, QDs with similar sizes are assumed to be preferably coupled with each other owing to this size resonance effect, as schematically shown in Fig. 4.5. Because actual QDs necessarily exhibit a small size distribution, where commercially available QDs reveal less than ±5–10 nm of the size distribution, and their size distribution causes inhomogeneous emission properties, such size- and number-selectivity of the QDs during the coupling process is expected to result in uniform emission spectra and emission intensity of mass-produced nanophotonic droplets, as we experimentally verified in the previous section. To discuss the dynamics of the coupling process, here we focus on the change in the emission spectra during the coupling process.

As schematically shown in Fig. 4.5, because each QD preferably pairs with another QD of a similar size due to the size-resonance effect [33], in the case of using CdSe-QDs and CdS-QDs, emission from coupled CdS-QDs decreases as a result of the energy transfer to its partner of the coupling, i.e., to CdSe-QD with a resonant size,

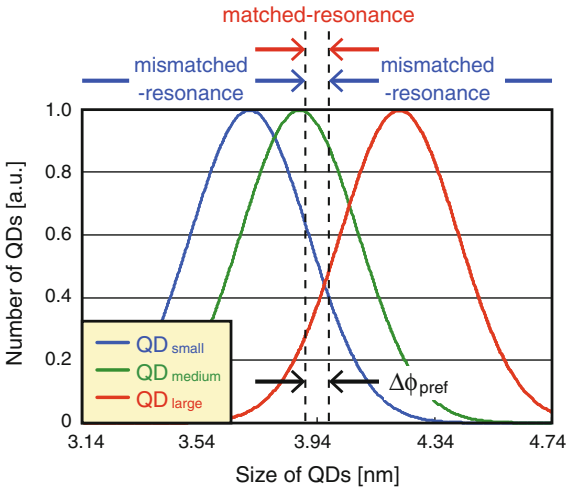

Fig. 4.14 Numerically assumed size distributions of QDs considered in the stochastic model

while CdSe-QD emits light with a larger optical energy. As a result, the peak photon energy of the total emission spectrum from CdSe- and CdS-QD shifts. Thus, the monitored emission spectra of the samples reveal the dynamics of the coupling process.

To numerically model the coupling process for comparison with experimental results, we defined a coupling rate and constructed a stochastic model. The coupling rate depends on two factors, the frequency of the encounter and the coupling. Thus, our model consists of two stochastic procedures, which respectively correspond to these factors. For the sake of simplicity, a 1D coordinate space is considered in our modeling. As shown by the experiments previously described, the coupling rate depends on the size-resonance. This is numerically modeled by considering the size distribution of QDs. Figure 4.14 shows the assumed size distributions of the three types of QDs, namely QD_{small}, QD_{medium}, and QD_{large}, where smaller QD emits larger photon energy of lights owing to the mechanism of emissions from QDs. Here, we define the allowance size for the coupling, $\Delta\phi_{pref}$, which was experimentally estimated to be $3.90 < \Delta\phi_{pref} < 3.98$.

As the first step of the numerical trial in our model, the size of the QD is randomly selected. Then, the following sequence is executed only when the selected size is within the distribution of $\Delta\phi_{pref}$. Otherwise, the trial is terminated and another trial is launched. The frequency of the encounter experimentally depends on the temperature of the sample during the coupling process. Here, two 1D coordinates are assumed for its estimation. Each coordinate representing the position of QD randomly fluctuates within an appropriate range until the coordinates of the two QDs crosses, or until a sufficient number of numerical steps is processed. Here, the range of the coordinate fluctuation corresponds to the temperature of the mixture, while a higher temperature induces larger fluctuations of components.

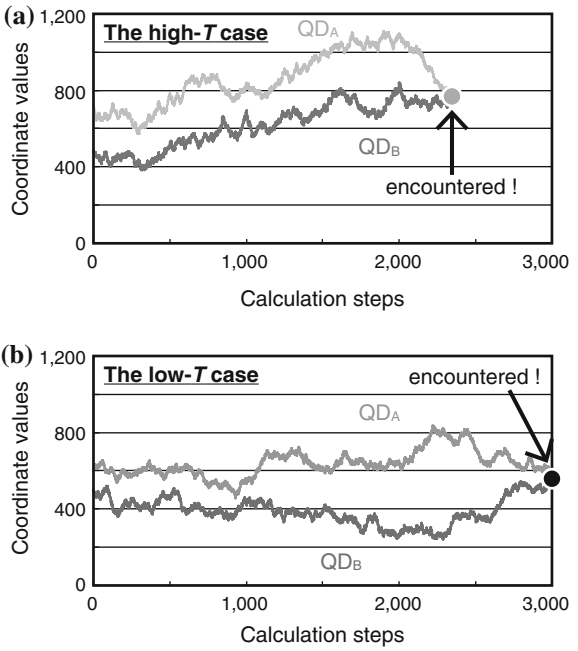

Fig. 4.15 Comparison of random fluctuations of 1D coordinates between **a** the high-T and **b** the low-T cases in the stochastic model

For example, Fig. 4.15 show the calculated temporal evolutions of the coordinate for higher and lower temperatures, respectively, where the amplitude of the former was 1.2 times larger than the latter on average. As shown, the high-T case shows that the QDs encounter faster than in the low-T case. After the two QDs successfully encounter, another trial is started selecting QDs of other sizes. After a sufficient number of iterations, the coupling rate of the QDs is calculated as the ratio of the total number of successful encounters to the number of trials. Based on the above modeling, the dependency of the size-resonance and the temperature on the coupling rate was numerically verified.

Figure 4.16a shows the amounts of shift in photon energy during the coupling between CdS_{415} QDs, and $CdSe_{546}$, $CdSe_{557}$, and $CdSe_{578}$ QDs. In this figure, because the average size of the $CdSe_{557}$ QDs is tuned to the size-resonance to the CdS_{415} QDs, they showed the steepest gradient of the blue shift in the photon energy. In contrast, the average sizes of $CdSe_{546}$ and $CdSe_{578}$ are slightly off-resonant to CdS_{415} QDs, resulting in red shift, which is exhibited at an early phase in the coupling process, from 0 to 30 min. The magnitude of the red shift depends on the degree of off-resonance. Further, as shown, all curves reveal monotonous increases in the coupling rate. In particular, in Fig. 4.16b, the increase with the steepest gradient was found with QD_{medium}, rather than QD_{small} and QD_{large}, which agrees with the experimental results shown in Fig. 4.16a.

Next, to verify the dependence of the velocity-fluctuation on the temperature during the coupling process, more experiments were performed to measure the temporal

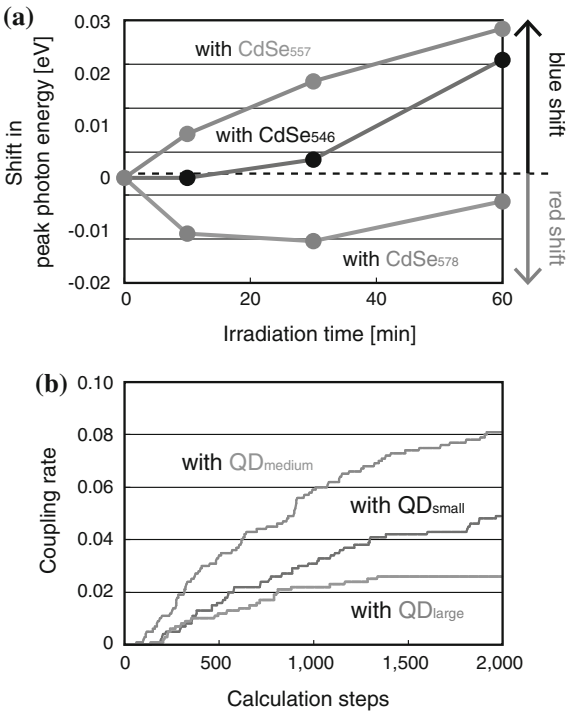

Fig. 4.16 **a** Temporal evolution of shift in peak photon energy emitted from the mixed solution of CdSe QDs, CdS QDs, and UV-curable polymer during illumination by the assisting light by a using CdSe QDs with various size distributions. **b** Numerical verification of dependency of the coupling rate on the size difference

evolution of the emission spectra using a hot-water bath. The temperature, T, was fixed to 350 and 290 K, that is, the temperature in the former experiment was 1.2 times that in the latter. Size-resonant $CdSe_{557}$ QDs and CdS_{415} QDs were used for this experiment. Figure 4.17a shows the observed time variation of the peak photon energy of the emission during irradiation with the assisting light. Similarly to the cases shown in Fig. 4.16a, a lower gradient was observed at an early phase of the variation when T = 350 K. Moreover, after this early phase, a steeper gradient was observed, and a larger shift was obtained than when T = 290 K. In contrast, the numerically obtained results are shown in Fig. 4.17b. As shown, the coupling rate for the high-T case was higher than that for the low-T case, which agrees with the experimental results shown in Fig. 4.17a.

In our stochastic model, only the frequency of successful coupling between QDs is considered, and subsequent shifts in the peak photon energy of their emission spectra are ignored for the sake of simplicity. This may be one explanation for some of the differences between the experimental and numerical results, especially the red shift in the early phase of the coupling process. Nevertheless, even with such approximations in our models, the time-evolving behaviors were in sufficient agreement. These results strongly indicate that the autonomy of the process and the homogeneity of the products, as shown by fluorescence images in Figs. 4.9 and 4.10,

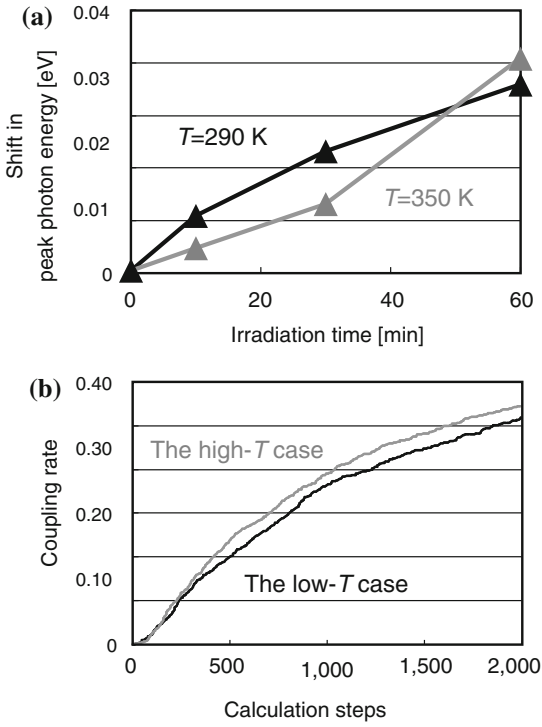

Fig. 4.17 **a** Temporal evolution of shift in peak photon energy emitted from the mixed solution of CdSe-QDs, CdS-QDs, and UV-curable polymer during illumination by assisting light using CdSe-QDs with mixed solutions at different temperatures to induce various levels of velocity fluctuations. **b** Numerical verification of dependency of the coupling rate on the temperature based on the stochastic model

depend on the size-resonance effect between components and the temperature of the mixture during the coupling process, as was expected.

4.2.6 High-Yield Optical Energy Conversion

The most important aspect in the concept of droplets is that such the precise alignment of QD as shown in Fig. 4.11 induces lossless energy transfer between each QDs and leads to corresponding high-yield optical energy conversion [37].

To quantitatively verify the yield of the energy conversion, two sample polymer materials, w/-droplets and w/o-droplets, which include droplets with aligned QDs and randomly dispersed QDs, respectively, are prepared. For preparation of the w/-droplets sample, mass-produced droplets were extracted and embedded in another pure PDMS solution. Then, the solution was cured for 2 h by heating it at 150 °C after degasing to remove air bubbles in the mixture. The numbers of droplets in the w/-droplets and w/o-droplets samples were set to be equivalent. Figure 4.18a shows the appearances of both samples under room light. As shown, it is quite difficult to discern a difference between the two, because their compositions are similar. However, as shown in Fig. 4.18b, their appearances under UV light seem quite different in terms

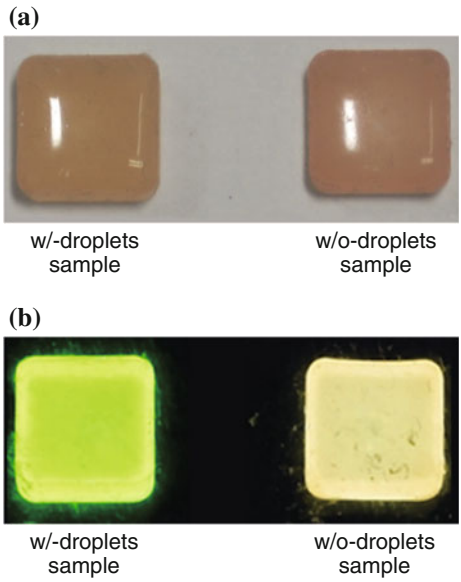

Fig. 4.18 Appearance of w/-droplets sample (*left*) and w/o-droplets sample (*right*) under **a** room light and **b** UV light

of their color tones: the w/-droplets sample showed a more monochromatic green appearance when compared to the w/o-droplets sample. This observation supports the mechanism of the emission processes in both samples, where the w/-droplets sample is expected to show enhanced light emission from the CdSe-QDs, whereas the w/o-droplets sample is expected to show individual emissions from both CdSe-QDs and the CdS-QDs.

For more quantitative evaluation of their optical properties, we measured the emission spectra by irradiation of $\lambda = 325$ nm of lights to both samples, which are shown in Fig. 4.19. Peaks at 420 and 560 nm in the spectra correspond to emission from the CdS-QDs and CdSe-QDs, respectively. As shown, the w/-droplets sample showed a 3.7-times higher intensity of emission from the CdSe-QDs, whereas the intensity of emission from the CdS-QDs decreased, which is evidence of the successful existence of droplets in the w/-droplets sample. Moreover, a sideband-like spectral feature from 500 nm to 650 nm was also decreased due to the existence of droplets. This spectral feature can be attributed to emission from the defect levels of the CdS-QDs.

As can be confirmed from the existence of emission spectra from the CdS-QDs in the w/-droplets sample in Fig. 4.19, not all QDs in the w/-droplets sample are coupled with CdSe-QDs, and the sample also includes isolated QDs. To directly discuss the improvement in the energy effectiveness due to the existence of droplets and to compensate for the effect of the emission from isolated QDs in the w/-droplets sample, we defined a metric called the differential optical amount,

$$D = (I_{\mathrm{w/}} - I_{\mathrm{w/o}})/h\nu, \tag{4.3}$$

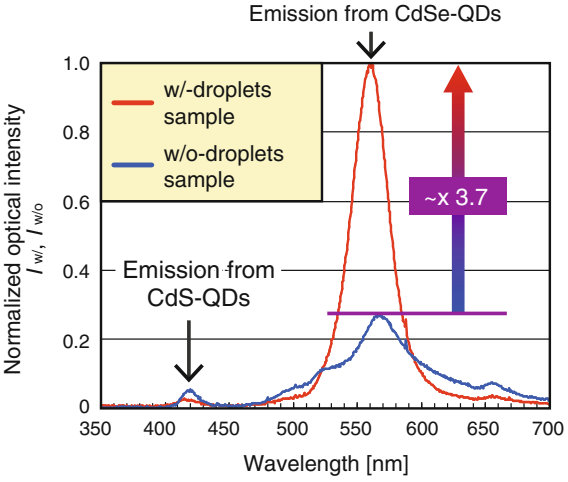

Fig. 4.19 Comparison of emission spectra with 325 nm light irradiation, measured with w/-droplets sample (*red line*) and w/o-droplets sample (*blue line*), respectively

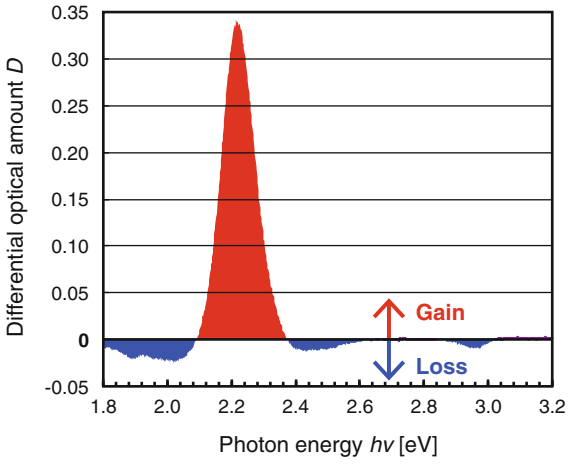

Fig. 4.20 Description of differential optical amount, D, calculated from the results in Fig. 4.19

where $I_{w/}$ and $I_{w/o}$ represent the normalized optical intensities in Fig. 4.19, and $h\nu$ represents the photon energy of light at each wavelength. The calculated D is explained in Fig. 4.20.

The regions filled with red and blue correspond to the gain and loss caused by the existence of the droplets, respectively. As shown, the total gain due to the existence of the droplets was 4.2-times larger than that of the loss. This result can be attributed to the effective use of the incident optical energy by the induced energy transfer from the CdS-QDs to the CdSe-QDs. Thus, while individual QDs necessarily reveal quenching of optical energy during their emission process, in the case of coupled QDs, the optical energy transfer occurs preferentially before the quenching process. Therefore, the incident optical energy is utilized for wavelength conversion in droplets much more effectively than in the case of randomly dispersed QDs.

4.2.7 Further Discussions

Solar photovoltaics [40] is one of the most attractive applications of optical energy conversion, and many types of photovoltaic systems have been developed. Among these, silicone (Si)-based solar cells [41] are the most familiarized type because they exhibit high efficiency, cost effectiveness, and industry relevance. Moreover, they exhibit additional properties such as flexibility and transparency. However, the sensitivities of Si-based as well as other types of solar cells are limited as a result of the specifications of photo-detectors. In fact, in the case of Si-based photo-detectors, there is insufficient reaction to the incidence of deep UV lights (deeper than 250 nm) and far IR lights (farther than 1.1 μm).

We are now discussing the application of the high-yield optical energy conversion by using droplets to compensate for such the sensitivity limitations by converting deep UV lights and far IR lights to the sensitive wavelengths of lights. Figure 4.21 describes this concept. In general, the photon energy of solar lights include 20 % of UV light and 5 % of IR light. If such lights are converted to visible light by *nanophotonic sheet*, which is a transparent sheet containing droplets, for photovoltaics by solar cells, the light-use efficiency is expected to improve by more than 5 %.

For a fundamental demonstration of our idea, transparent polymer samples with QDs are prepared. Similar to the previous demonstration, we prepared two samples, w/-droplets and w/o-droplets. To ensure sufficient transparency to solar lights, the amounts of QDs are confined, such that the competition of existence of droplets is expected to characteristically occur. In this case, 10^{14}–10^{15} of CdSe- and CdS-QDs are approximately mixed in 1.1 mL of PDMS solutions. Here, Fig. 4.22a, b show the appearances of the samples under room light and UV lights, respectively.

As shown, while both samples reveal sufficient transparencies and they are difficult to be differentiated under the room light, they reveals clear differences in their fluorescences under the UV lights. In other words, the w/-droplets sample reveals a much stronger fluorescence than the other sample. Figure 4.22c shows the difference between the emission spectra of the two samples obtained by using an Xe lamp. As can be seen, the w/-droplets sample reveals a higher optical conversion from the UV lights to the visible lights owing to the existence of droplets in the sample.

We now prepare thinned samples with thicknesses less than 500 μm as nanophotonic sheets to improve the incidence of the converted lights to the photo-detector, and demonstrate the improvement in the light-use efficiency. An important aspect of our idea is that the specifications of the nanophotonic sheets can be easily customized by using different types of QDs. Various types of solar cells reveal different sensitivities; however, such flexibility is expected to be universally applied to any types of solar cells.

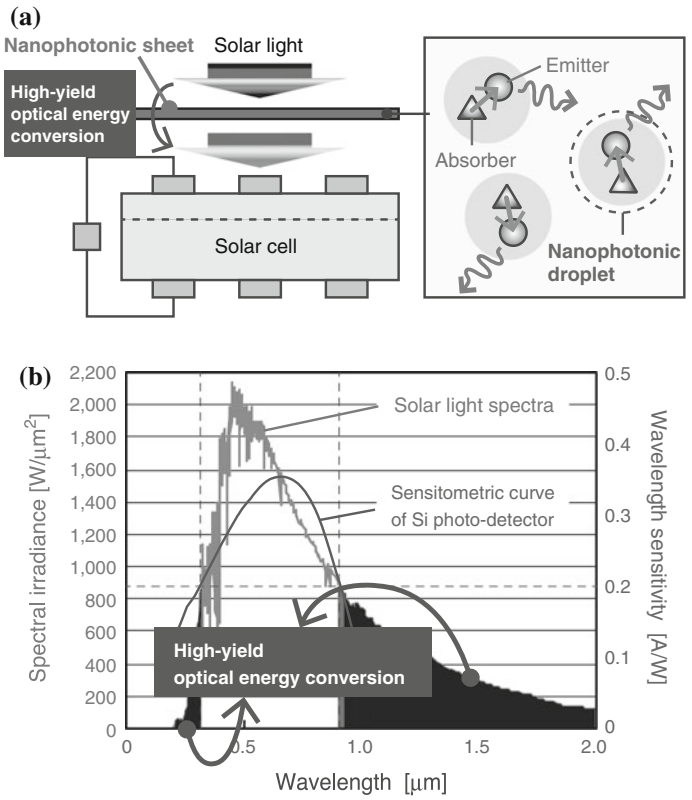

Fig. 4.21 **a** Schematic diagram of utilization of nanophotonic sheet for improvement of light-use efficiency of solar cells. **b** Concept of upper- and lower-optical energy conversion for the improvement

4.3 Optical Annealing-Based Electrooptical Device

4.3.1 General Fabrication of Oxide Semiconductor

Oxide semiconductors are widely used direct-transition materials having a large bandgap. Owing to their natural abundance, innocuousness, and transparency to visible light, they are expected to be widely employed for fabricating various electrical and optical devices [42–51]. Although such oxide semiconductors are highly promising from the viewpoint of social needs, it is technically difficult to implement electro- or magneto-induced optical functions using the standard doping methods used with other types of semiconductors. This is because acceptors from the dopants are generally compensated with donors from the numerous oxygen vacancies and interstitial metals in the crystal.

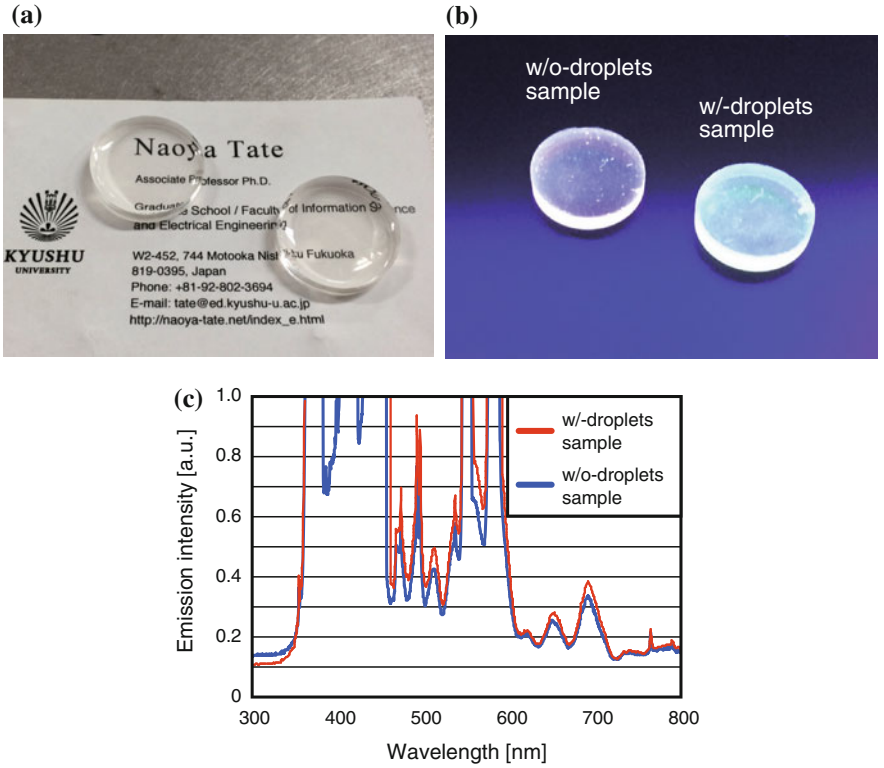

Fig. 4.22 Appearance of w/-droplets sample (*left*) and w/o-droplets sample (*right*) under **a** room light and **b** UV light. **c** Emission spectra of the two samples

Zinc oxide (ZnO) is one of the most widely used direct-transition-type semiconductors because to its wide band gap, high electron mobility, and high transparency to visible light [52]. Although ZnO exhibits such useful properties, it is technically difficult to implement electrically induced optical functions. One of the major reasons for thus is the difficulty in fabricating the devices. To realize an electrooptical device by using ZnO crystal, it is generally necessary to add p-type dopants to the n-type crystal, so as to fabricate a p–n junction that exhibits various electrooptical properties, such as a rectifying property and the photovoltaic effect [42–46]. However, in the case of the ZnO crystal, the sequential generation of donor dopants occurs in the crystal in association with the introduction of acceptor dopants, and they compensate each other [52]. It is therefore technically difficult to fabricate a p–n junction with sufficient quality to be used as a practical electrooptical device.

4.3.2 Phonon-Assisted Optical Annealing

According to recent research by the authors' group [13, 14, 18, 53–57], novel electrooptical characteristics using various indirect- and direct-transition semiconductors have been successfully demonstrated by employing our original annealing method, which exploits the characteristic behavior of DPs [58]. A technique known as *phonon-assisted annealing* has been used to autonomously form a dopant distribution that works as an appropriate p–n homojunction layer to effectively induce DPs by light irradiation. The basics of the DP-phonon-assisted annealing method are explained below.

First, while Joule heat is generated by the application of a forward bias current to the device, the dopants try to randomly diffuse in the material to converge to a homogeneous distribution. However, at the same time, DPs tend to be generated by irradiation of light in the vicinity of the exciton polaritons. Here, the generation of DPs is due to the formation of localized electrons and holes at regions of a specific distribution of the dopants. In the case where the photon energy of the irradiated light is lower than the bandgap energy of the material, as in our method, the photon energy is not absorbed in the material and can reach the distribution of dopants, where it generates DPs. The generated DPs, which behave as localized energy fields [10, 19, 28, 59, 60], can excite multimode coherent phonons in the material, and a coupled state of the DPs and phonons can be excited; in other words, a multi-step electron transition occurs via energy levels corresponding to the coupled state. Consequently, part of the energy due to Joule heat is converted to the photon energy of stimulated emission via the DPs, which is associated with the multi-step transition. Subsequently, Joule heat is lost and diffusion of the dopants stops. Now, the distribution of dopants works as an appropriate structure for the effective generation of DPs. In contrast, other dopants where DPs are hardly generated in their vicinities continue to diffuse in the material until they form the required specific distribution, and subsequent stimulated emission occurs. Finally, a high DP generation efficiency is exhibited in all regions, and the temperature drops in all regions of the device. In particular, by using an n-type bulk ZnO crystal, a p–n homojunction-structured LED that emits light at room temperature has been successfully realized by utilizing phonon-assisted optical annealing [14].

4.3.3 Device Fabrication

To fabricate the prototype device, we used commercially available n-type ZnO single crystal with a thickness of 500 μm, which is prepared by the hydrothermal growth method [61]. The crystal axis orientation was (0001), and the initial electrical resistivity of the crystal was 50–150 Ω ·cm. The basic process for fabricating a junction ZnO device is schematically shown in Fig. 4.23.

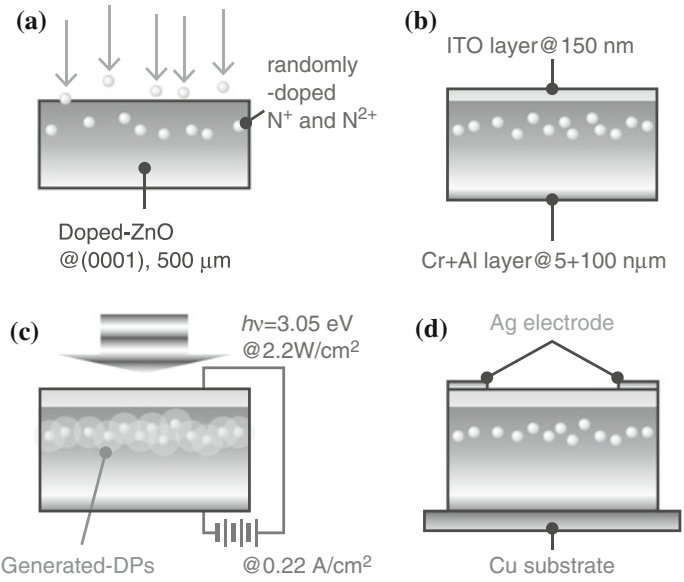

Fig. 4.23 Basic process for fabricating a ZnO device. **a** Implantation of N^+ and N^{2+} ions into n-type ZnO single crystal. **b** Depositing electrode layers at the front side and back side of the crystal. **c** Application of forward bias current and irradiation of light for the phonon-assisted annealing. **d** Deposition of Ag electrode on the crystal and bonding of crystal to Cu substrate for heat dissipation

N^+ and N^{2+} ions were implanted into the crystal in six steps at energies of 20, 50, 100, 200, 400, and 600 keV for producing a broad distribution of dopants. The ion dose densities were set to 4.20×10^{13}, 9.00×10^{13}, 2.25×10^{14}, 2.75×10^{14}, 4.50×10^{14}, and 4.50×10^{14} cm^{-2}, respectively (Fig. 4.23a). By using multi-step implantation with these parameters, the implanted dopants were distributed in a broad region in the crystal to form a p-type layer. Then, using radio-frequency sputtering, a 150 nm-thick indium tin oxide (ITO) layer was deposited on the front side of the sample, and a 5-nm-thick Cr layer and a 100-nm-thick Al layer were deposited on the back side of the sample to serve as electrode layers (Fig. 4.23b). After deposition, phonon-assisted annealing was performed (Fig. 4.23c). During Joule heating by application of a forward bias current, the device was irradiated with laser light having a photon energy $h\nu$ = 3.05 eV, which is lower than the bandgap energy of the ZnO crystal (3.40 eV). The forward bias current density was set to 0.22 A/cm^2, which was as high as possible without causing thermal destruction of the device, and the power of the irradiated light was set to 2.2 W/cm^2, which was as high as possible without causing the crystal temperature to become too high. According to

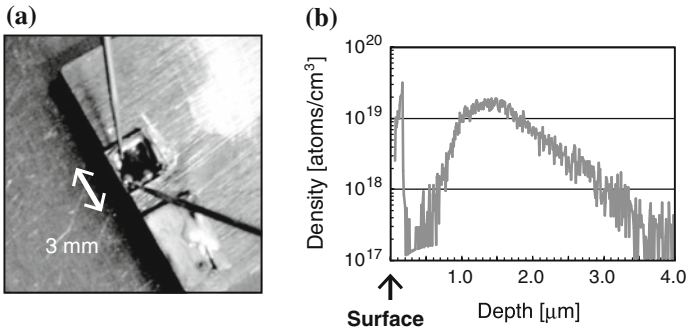

Fig. 4.24 **a** Photograph of the fabricated ZnO device. **b** The dopant density versus implantation depth in the device

the previous work by the authors' group [14], the surface temperature increased to nearly 100 °C under similar experimental conditions, and then dropped to a constant temperature of 70 °C. As we described in the Basics section, this drop in temperature corresponds to the generation of DPs, bringing about stimulated emission, and indicates successful completion of the annealing process for fabricating an appropriate distribution of dopants in order to efficiently generate DPs in the material. Then, Ag electrodes were deposited for applying an in-plane current to the device, in a direction perpendicular to the direction during the annealing process. Finally, the crystal was bonded on a Cu substrate for heat dissipation while working as a polarization rotator (Fig. 4.23d). The Cr and Al layers were utilized as reflecting surfaces for the incident light applied to the device. Figure 4.24a shows a photograph of the fabricated ZnO device. The dopant implantation depth was confirmed by secondary ion mass spectrometry (SIMS) to be about 2 μm, as shown in Fig. 4.24b. In a related study, the detailed dopant distribution formed by the phonon-assisted annealing has been previously confirmed in the case of Si by using a three-dimensional atom probe (3DAP) method [55].

4.3.4 Demonstration as Polarization Rotator

Firstly, we demonstrate the device specifications as a polarization rotator. The experimental setup used for demonstrating polarization rotation is shown in Fig. 4.25.

The setup was constructed to observe modulated light among the incident linearly polarized light. As shown in the inset of Fig. 4.25, a current flowed in the in-plane direction of the device via surface electrodes formed of an ITO layer, and the in-plane current induces sufficiently large magnetic fields at the surface of the device. The applied voltage was sinusoidally modulated by a function generator. Linearly polarized light having a photon energy $h\nu$ = 3.05 eV, to which the device is transparent, was radiated in the vertical direction onto the device and was output in the

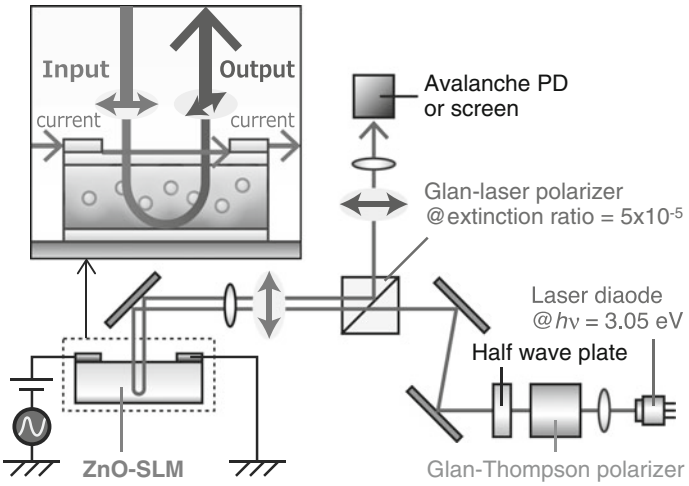

Fig. 4.25 Schematic diagram of setup used for observing polarization rotation based on cross-Nicol method

opposite direction by reflection at the back side of the device. During propagation in the device, the incident light was expected to be affected by the applied current via interactions between the material and DPs. As a result, the ZnO material behaves as quarter-wave plate (QWP) to the incident light, as briefly discussed at the end of this section. Because QWP converts linearly polarized light to circularly polarized light, the reflected light in Fig. 4.25 reveals linear polarization with some polarization rotation by back-and-forth during propagation in the ZnO material. As a result, corresponding polarization rotation was observed as a variation in the optical intensity of the reflected light by using a Glan-laser polarizer.

Figure 4.26a shows the modulated output projected on a phosphor screen, which was set at the output port. To clearly represent the spatial dependency of the modulation, the input light was radiated onto the device using an off-focus setup. Therefore, one cycle of varying brightness, between the bright and dark parts in each area, corresponds to a modulation of π radians. As shown, the spatial modulation of the polarization was found to depend on the applied current.

To quantitatively evaluate the polarization rotation shown in Fig. 4.26a, input light was focused onto the device, and the intensity of the output light was observed by using an avalanche photodiode (PD). Figure 4.26b shows an example of the output light intensity observed with 100 mHz sinusoidal modulation of an 18 V applied voltage. As shown, spatial modulation of the output signal amplitude was clearly observed. Importantly, Fig. 4.26b shows that, while the applied voltage was increased to 18 V during a half cycle of applied voltage, the polarization of the input light was rotated by more than 6π radians.

To explain the large amount of polarization rotation achieved by our device, the relationship between the applied current I_{IN} and the polarization rotation θ_{rot} is

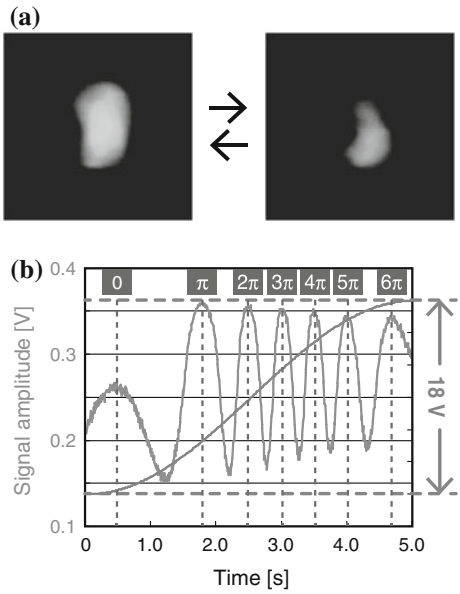

Fig. 4.26 **a** Modulated output images, which were projected on a phosphor screen. **b** Experimentally observed relationships between the output light intensity (*red line*) and the voltage applied to the device (*blue line*), where the maximum voltages were 18 V

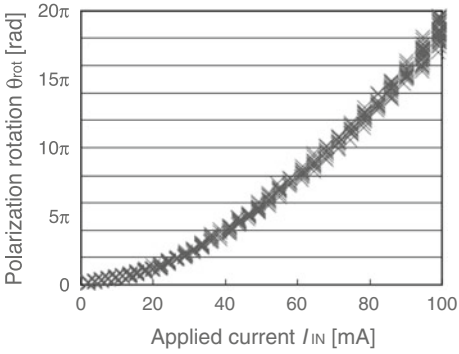

Fig. 4.27 Relationship between applied current I_{IN} and polarization rotation θ_{rot}

plotted by using the measured I-V relationship of the device. As shown in Fig. 4.27, the device achieved a polarization rotation of more than 20π radians by applying 100 mA of current. In terms of the amounts of Faraday rotation, it reveals an intermediate value between dielectric semiconductors and magnetic metals.

The important point of our approach is that such a giant polarization rotation does not require any external equipment for applying a strong magnetic field, unlike the conventional magnetooptical effect. Also, a long propagation distance of the incident light is not required; the effective propagation distance for the modulation was less than 5 μm, because of the back-and-forth propagation in the device, as indicated by the SIMS results shown in Fig. 4.24b. The basic mechanism of such a large polarization rotation is discussed below.

Simple and direct propagation of light in the material under a current-induced magnetic field is hardly expected to reveal such an effect, and therefore, the involvement of DPs must be considered. Namely, incident light induces DPs in the surroundings of the dopants, and at the same time, current-induced magnetic fields strongly affect the phase of the DPs via the distribution of dopants. In such a situation, the incident optical energy and magnetic fields are allowed to efficiently interact with each other via the DP states, where the DP states are efficiently energetically coupled with the phonon states of the material. After the interaction, reconversion of optical energy from the DPs to propagating light occurs, and other interactions are induced in surroundings of other dopants. While the expected amount of modulation in a single process is not large enough, after a number of iterations of this process, a large amount of modulation is finally realized. We expect that the theoretical relationship between the phase of the DPs and magnetic fields will be clarified in future experiments.

4.3.5 Demonstration as Optical Switching

Results of the previous demonstrations that revealed giant polarization rotation were demonstrated by using a reflective-type device [62]. To improve the practicality of our idea, we newly developed a transmissive-type device. Similar to fabrication of the previous device, a commercially available ZnO single crystal, which was prepared by the hydrothermal growth method, was used, and nitrogen ions were doped into the crystal by using multi-step implantation. The implantation is done by sequentially applying N^+ and N^{2+} with acceleration energies in six steps from 20 to 600 keV. As a result, the thickness of the doped layer in the ZnO crystal became 2–3μm with a dopant density of 10^{18}–10^{19} atoms/cm^3, and the depth from the surface of the device was less than 1 μm. As the surface side and underside electrodes, 150-nm-thick ITO films were deposited by radio frequency (RF) sputtering, and Au terminals were fabricated at each side by deposition and etching processes. Then, the doped-ZnO was set on a glass epoxy substrate, and an aperture was formed to allow transmission of the incident light.

The surface side and underside electrodes were connected so as to perform optical annealing. During 16 h of annealing, a forward bias current with a current density less than 0.1 A/cm^2 was applied between the surface side and underside electrodes, which was the highest current that could be applied without causing any thermal destruction of the Au terminals. The photon energy of the annealing light was set at 3.05 eV, which is much lower than the bandgap energy of ZnO (3.40 eV), and the power density of the annealing light focused on the device was 1 W/cm^2.

After the annealing process, similar to the previous demonstration, the electrode connection was changed to apply the in-plane current for driving the device, as shown in Fig. 4.28a. Here, the same light source as that used for the annealing light was used as the input light source. Photographs of the device are shown in Fig. 4.28b. As can be seen, four independent units were prepared on a single device to verify

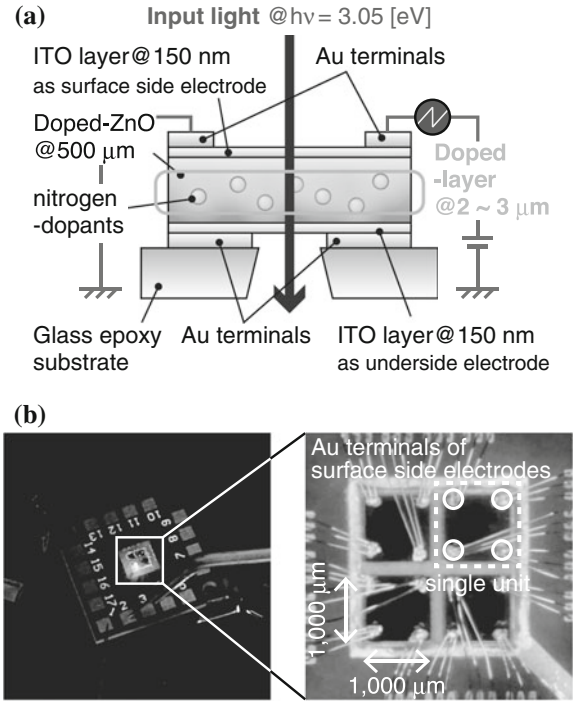

Fig. 4.28 **a** Schematic diagram of transmissive-type ZnO-SLM and **b** photograph of the device consisting of 2×2 units

the crosstalk between each unit. Each unit has four Au terminals, and the in-plane current was applied by connecting two arbitrary terminals of the four terminals.

Polarization rotation based on the magnetooptical effect is one aspect of the circular-polarization selection rule toward optical transitions in a material with high magnetization. In other words, a difference in the refractive index between left- and right-handed circularly polarized light corresponds to rotation of linearly polarized light. Although giant polarization rotation has been previously demonstrated by our group [62], here we focus on modulation of the refractive index and a corresponding beam shift of plane-wave light by using a ZnO-SLM. The basics of the demonstration can be described as follows.

As schematically shown in Fig. 4.29, because a spatial distribution of the in-plane current density and a corresponding magnetic field distribution can be caused by using two terminals on the surface side electrodes of the SLM, a corresponding spatial distribution of the refractive index of ZnO is obtained. In such a case, incident plane-wave light is refracted by the SLM. If different pairs of terminals are used, refraction in different directions is induced.

Figures 4.30 show the results of some demonstrations of the refraction of plane-wave light, where the output light was captured by a CCD camera when voltages of 0 (left) and 18 V (right) were applied to the SLM. In the experiment, only one of the four units was driven, and only the corresponding light, namely, the upper-right light

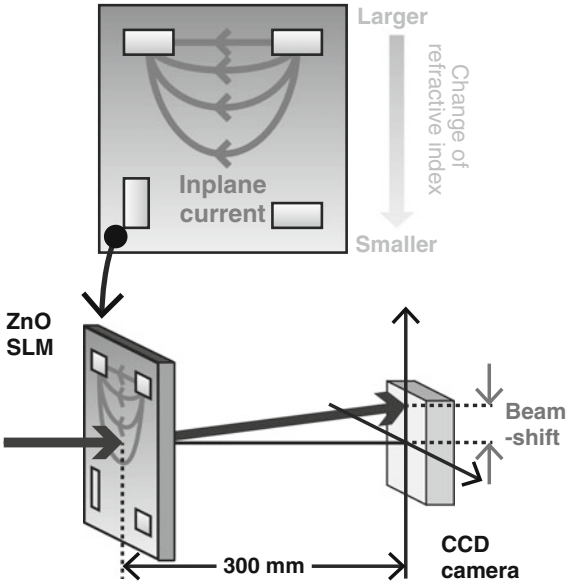

Fig. 4.29 Schematic diagram of spatial distribution of the refractive index due to spatial distribution of the in-plane current density (*upper*), and corresponding beam shift of the incident plane-wave light (*lower*)

in Fig. 4.30, was modulated. As shown in Fig. 4.30a, b, only the upper-right light was shifted in the vertical and horizontal directions, respectively.

Thus, the refraction direction corresponds to the position of the terminals used for injection of the in-plane current. As a result, we verified that the spatial distributions of the in-plane current density and the corresponding magnetic fields induced a spatial distribution of the refractive index in the ZnO. During the demonstration shown in Fig. 4.30a, the change in the refractive index, which is approximately calculated from the amount of shift of the incident light, depends on the voltage applied to the SLM, as shown in Fig. 4.31.

As shown, a change in refractive index of up to 0.40, which is 5 % of the change rate relative to the default refractive index of ZnO crystal (2.00) at room temperature, was obtained by applying a voltage of 20 V. This change is extremely large as compared to that in well-known magnetooptical materials, such as yttrium iron garnet (YIG) [?].

Moreover, the various directions and amounts of refraction obtained by using various pairs of terminals are shown in Fig. 4.32. Figure 4.32a shows a case where an annealed unit is used, and Fig. 4.32b–d shows cases where non-annealed units are used. The squares and number in each square represent the positions and serial numbers identifying the terminals of the surface side electrode, respectively, and the underlined numbers represent the used pairs of terminals.

As shown, the amounts of shift and the shift directions with the non-annealed units were more non-uniform, whereas more uniform refraction was obtained with the annealed unit. The results indicate that phonon-assisted optical annealing realizes

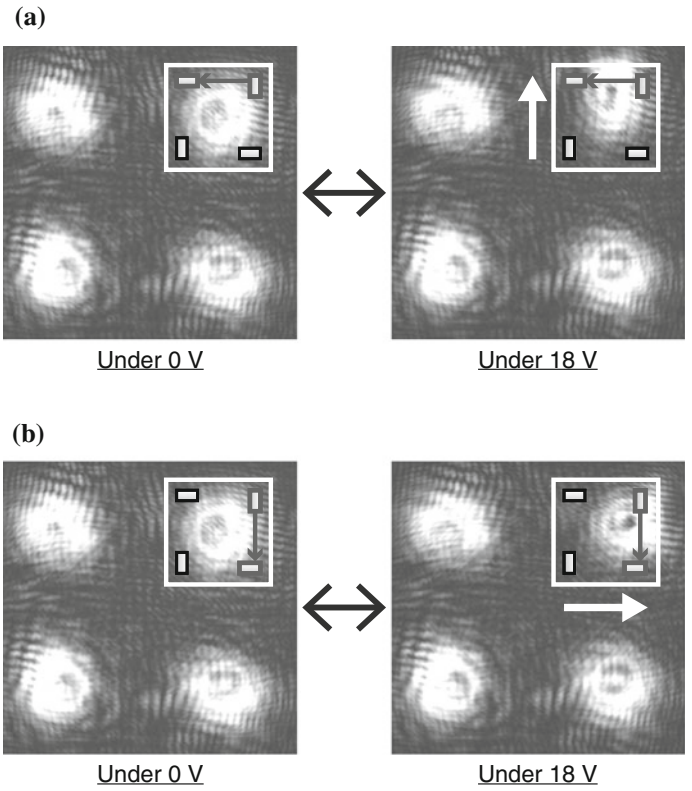

Fig. 4.30 Experimental results of refraction of plane-wave light in **a** vertical direction and **b** horizontal direction

Fig. 4.31 Change in refractive index

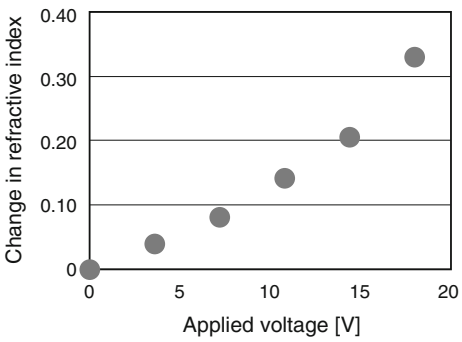

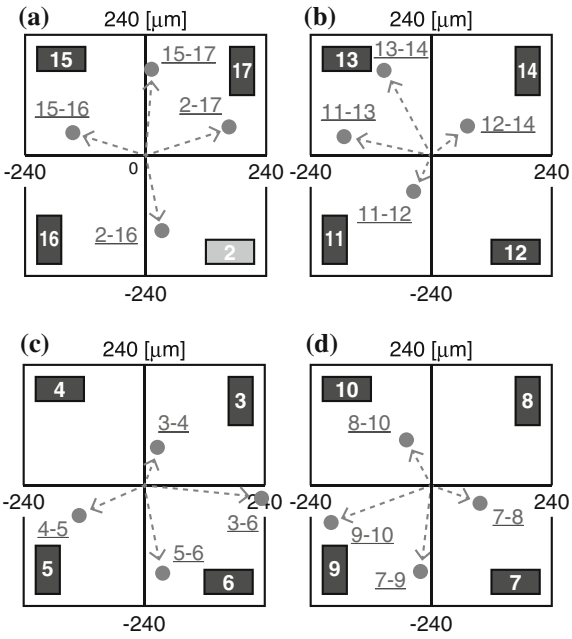

Fig. 4.32 Directions and amounts of refraction by using various pairs of terminals with **a** annealed unit and **b**, **c**, **d** non-annealed units. Terminal 2 is used during the optical annealing process

homogeneously distributed dopants by the self-organizing matter, so that the spatial distribution of the refractive index is homogeneously modulated by using any pairs of terminals.

4.4 Summary

Concept of nanoscale interactions via energy dissipation and fluctuation have been actively studied in various research fields. In the case of optics and photonics, optical near-field interaction between light and materials is similar to this concept. The important aspect in this is the appropriate external control of the dissipation and the fluctuation to realize optimal nanometric structures and reveal the corresponding high-yield optical functions, as we discussed in this chapter. Such aspects are expected to be observed in not only nanophotonic droplets and oxide semiconductor devices but also various nanophotonic setups. In future research, discovery of such setups and installation of our concept of nanophotonics-based self-assembly are strongly desired to ensure further development of practical nanophotonic applications [63].

References

1. S. Franssila, *Introduction to Microfabrication*, 2nd edn. (John Wiley & Sons, 2010)
2. C.A. Mirkin, S.H. Hong, L. Demers, Chem. Phys. Chem. **2**, 37 (2001)
3. J.P.H. Benschop, A.J.J. Van Dijsseldonk, W.M. Kaiser, D.C. Ockwell, Solid State Technol. **42**, 43 (1999)
4. J.G. Chase, B.W. Smith, J. Intell. Mater. Syst. Struct. **12**, 807 (2001)
5. F. Cerrina, J. Phys. D (Appl. Phys.) **33**, R103 (2000)
6. J. Melngailis, I.L. Mondelli, R. Berry III, R. Mohondro, J. Vacuum Sci. Technol. B (Microelectron. Nanometer Struct.) **16**, 927 (1988)
7. G.M. Whitesides, B. Grzybowski, Science **295**, 2418 (2002)
8. P.W.K. Rothemund, Nature **440**, 297 (2006)
9. M. Ohtsu, K. Kobayashi, T. Kawazoe, T. Yatsui, M. Naruse, *Principles of Nanophotonics* (Taylor and Francis, 2008)
10. M. Ohtsu, *Dressed Photons* (Springer-Verlag, 2013)
11. S. Yukutake, T. Kawazoe, T. Yatsui, W. Nomura, K. Kitamura, M. Ohtsu, Appl. Phys. B **99**, 415 (2010)
12. H. Fujiwara, T. Kawazoe, M. Ohtsu, Appl. Phys. B **98**, 283 (2010)
13. T. Kawazoe, M.A. Mueed, M. Ohtsu, Appl. Phys. B **104**, 747 (2011)
14. K. Kitamura, T. Kawazoe, M. Ohtsu, Appl. Phys. B **107**, 293 (2012)
15. E. Smith, G. Dent, *Modern Raman Spectroscopy: A Practical Approach* (John Wiley & Sons, 2005)
16. K.D. Belfield, S.J. Caracci, F. Kajzar, C.M. Lawson, A.T. Yeates, *Multiphoton Absorption and Nonlinear Transmission Processes: Materials, Theory, and Applications* (Society of Photo Optical, 2003)
17. T. Kawazoe, H. Fujiwara, K. Kobayashi, M. Ohtsu, J. Sel. Top. Quantum Electron. **15**, 1380 (2009)
18. N. Wada, T. Kawazoe, M. Ohtsu, Appl. Phys. B **108**, 25 (2012)
19. M. Ohtsu, K. Kobayashi, *Optical Near Fields* (Springer, 2003)
20. K. Kobayashi, S. Sangu, T. Kawazoe, A. Shojiguchi, K. Kitahara, M. Ohtsu, J. Microsc. **210**, 247 (2003)
21. D. Goldhaber-Gordon, J. Göres, M.A. Kastner, H. Shtrikman, D. Mahalu, U. Meirav, Phys. Rev. Lett. **81**, 5225 (1998)
22. F. Simmel, R.H. Blick, J.P. Kotthaus, W. Wegscheider, M. Bichler, Phys. Rev. Lett. **83**, 804 (1999)
23. F.R. Waugh, M.J. Berry, D.J. Mar, R.M. Westervelt, K.L. Campman, A.C. Gossard, Phys. Rev. Lett. **75**, 705 (1995)
24. L.W. Molenkamp, K. Flensberg, M. Kemerink, Phys. Rev. Lett. **75**, 4282 (1995)
25. M. Taut, Phys. Rev. B **62**, 8126 (2000)
26. G. Burkard, G. Seelig, D. Loss, Phys. Rev. B **62**, 2581 (2000)
27. M. Ohtsu, K. Kobayashi, T. Kawazoe, S. Sangu, T. Yatsui, IEEE J. Sel. Topics Quantum Electron. **8**, 839 (2002)
28. K. Kobayashi, S. Sangu, H. Ito, M. Ohtsu, Phys. Rev. A **63**, 013806 (2001)
29. T. Kawazoe, K. Kobayashi, J. Lim, Y. Narita, M. Ohtsu, Phys. Rev. Lett. **88**, 067404 (2002)
30. N. Sakakura, Y. Masumoto, Phys. Rev. B **56**, 4051 (1997)
31. Z.K. Tang, A. Yanase, T. Yasui, Y. Segawa, K. Cho, Phys. Rev. Lett. **71**, 1431 (1993)
32. K. Kobayashi, S. Sangu, T. Kawazoe, M. Ohtsu, J. Lumin. **112**, 117 (2005)
33. S. Sangu, K. Kobayashi, M. Ohtsu, J. Microsc. **202**, 279 (2000)
34. N. Tate, Y. Liu, T. Kawazoe, T. Yatsui, M. Naruse, M. Ohtsu, Appl. Phys. B **110**, 39 (2013)
35. N. Tate, Y. Liu, T. Kawazoe, T. Yatsui, M. Naruse, M. Ohtsu, Appl. Phys. B **110**, 293 (2013)
36. N. Tate, M. Naruse, Y. Liu, T. Kawazoe, T. Yatsui, M. Ohtsu, Appl. Phys. B **112**, 587 (2013)
37. N. Tate, W. Nomura, T. Kawazoe, M. Ohtsu, Opt. Exp. **22**, 10262 (2014)
38. T. Kawazoe, K. Kobayashi, M. Ohtsu, Appl. Phys. Lett. **86**, 103102–1 (2005)

39. Y. Liu, T. Morishima, T. Yatsui, T. Kawazoe, M. Ohtsu, Nanotechnology **22**, 1 (2011)
40. P. Würfel, *Physics of Solar Cells: From Basic Principles to Advanced Concepts* (Wiley-VCH, 2009)
41. A. Goetzberger, J. Knobloch, B. Voss, *Crystalline Silicon Solar Cells: Technology and Systems Applications* (Wiley, 1998)
42. N. Yamazoe, Sens. Actuators B **5**(1–4), 7 (1991)
43. K.D. Schierbaum, R. Kowalkowski, U. Weimar, W. Göpel, Sens. Actuators B **7**(1–3), 709 (1992)
44. G. Kiss, Z. Pintér, I.V. Perczel, Z. Sassi, F. Réti, Thin Solid Films, **391**(2), 216 (2001)
45. K. Nomura, H. Ohta, A. Takagi, T. Kamiya, M. Hirano, H. Hosono, Nature **432**(7016), 488 (2004)
46. J.S. Park, W.-J. Maeng, H.-S. Kim, J.-S. Park, Thin Solid Films **520**(6), 1679 (2012)
47. E. Fortunato, P. Barquinha, R. Martins, Adv. Mater. **24**(22), 2945 (2012)
48. R. Singh, K. Rajkanan, D.E. Brodie, J.H. Morgan, IEEE Trans. Electron Devices **27**(4), 656 (1980)
49. K. Tennakone, G.R.R.A. Kumara, I.R.M. Kottegoda, V.P.S. Perera, P.S.R.S. Weerasundara, J. Photochem. Photobiol. A **117**(28), 137 (1998)
50. H. Arakawa, K. Sayama, Res. Chem. Intermed. **26**(2), 145 (2000)
51. Y.-S. Choi, J.-W. Kang, D.-K. Hwang, S.-J. Park, IEEE Trans. Electron Devices **57**(1), 26 (2010)
52. Ü. Özgür, Y.I. Alivov, C. Liu, A. Teke, M.A. Reshchikov, S. Doğan, V. Avrutin, S.-J. Cho, H. Morkoç, J. Appl. Phys. **98**, 041301 (2005)
53. H. Tanaka, T. Kawazoe, M. Ohtsu, Appl. Phys. B **108**(1), 51 (2012)
54. M.A. Tran, T. Kawazoe, M. Ohtsu, Appl. Phys. A **115**(1), 105 (2014)
55. N. Wada, M.A. Tran, T. Kawazoe, M. Ohtsu, Appl. Phys. A **115**(1), 113 (2014)
56. M. Yamaguchi, T. Kawazoe, M. Ohtsu, Appl. Phys. A **115**(1), 119 (2014)
57. T. Kawazoe, M. Ohtsu, Appl. Phys. A **115**(1), 127 (2014)
58. T. Kawazoe, K. Kobayashi, S. Takubo, M. Ohtsu, J. Chem. Phys. **122**(2), 024715 (2005)
59. Y. Tanaka, K. Kobayashi, Phys. E **40**(2), 297 (2007)
60. Y. Tanaka, K. Kobayashi, J. Microsc. **229**, 228 (2008)
61. T. Sekiguchi, S. Miyashita, K. Obara, T. Shishido, N. Sakagami, J. Cryst. Growth **214–215**(2), 72 (2000)
62. N. Tate, T. Kawazoe, W. Nomura, M. Ohtsu, Sci. Rep. **5** (2015). doi:10.1038/srep12762
63. W. Frank, A. Seeger, Appl. Phys. A **3**, 66 (1988)

Chapter 5
Ultraflexible Organic Electronics and Photonics

Tsuyoshi Sekitani

Abstract Ultraflexible, lightweight, and thin electronic sensors have been developed for realizing next-generation noninvasive bioinstrumentation systems that enable large-area and multipoint sensing using organic electronics and related systems including Si-LSI technology. The systems are thinner than human skin and can cover a wide surface area with complex shapes. In this chapter, here I will introduce fabrication methods and performance characteristics of ultrathin ($\sim$1 μm), ultraflexible organic light-emitting diodes (LEDs), organic solar cells (optical sensors, photodetector), and organic transistors. In addition, I will discuss the future prospects of ultraflexible biointerface electronics, which can be realized by integrating these devices.

5.1 Introduction

New electronic devices (electronics) that are lightweight, thin, and durable when bent or stretched are being developed using thin polymeric substrates. Flexible/stretchable electronics have various advantages; they can be applied to numerous locations; large-area electronics can be rolled up for transport, and they are break-resistant if dropped. Inorganic semiconductors such as silicon that have been the primary materials for conventional electronics and Si wafers used as substrates are hard and not bendable. In contrast, organic electronics, taking advantage of the flexibility intrinsic to organic materials, compensate for conventional transistors consisting mainly of Si and have been attracting attention as the electronics that can open a new era. In particular, we have entered the era of the Internet of Things (IoT), and various types of electronic sensor with a high cost efficiency (low cost for a large area) are demanded to collect information in the real world. Also in this sense, organic electronics fabricated by printing technology have been attracting attention.

T. Sekitani (✉)
The Institute of Scientific and Industrial Research, Osaka University,
8-1, Mihogaoka, Ibaraki, Osaka 567-0047, Japan
e-mail: sekitani@sanken.osaka-u.ac.jp

M. Ohtsu and T. Yatsui (eds.), *Progress in Nanophotonics 4*,
Nano-Optics and Nanophotonics, DOI 10.1007/978-3-319-49013-7_5

In this chapter, the latest developments in organic electronics and photonics using organic functional materials such as organic semiconductors are introduced. Our research group has succeeded in developing (1) ultrathin organic solar cells and ultrathin organic light-emitting diodes (LEDs), which are light (3 g/m^2), thin (2 μm), and flexible organic photoelectric conversion devices that function even if crumpled, and (2) ultrathin organic transistor circuits, as electronic switches, for the first time in the world. In this chapter, progress in the development of ultrathin flexible electronics, technological challenges, and their future prospect such as the contribution of such devices to the next generation of tools in the fields of medicine, health, and welfare are introduced.

5.2 Background and Purpose of Research

Along with the major social challenge, especially declining birth rate and aging population, interest in medical services and health has been increasing in the general population. In addition, with the spread of Internet technologies, information is more globalized and the lifestyle of people has become more diversified because they can easily access the worldwide web (WEB) anytime. In response to this situation, the electronics used in daily life have become increasingly diversified. Not only performance indices such as high-density integration, significant power savings, miniaturization, and high-speed operation, have been realized by rapidly advanced silicon-based technology, but also new performance indices such as lightness, durability, and user friendliness have been sought. In addition, wearable electronics have been attracting attention. Actuator-type devices, such as robotic orthoses and power suits, as well as implantable medical devices, such as pace makers and electrodes for deep brain stimulation to treat epilepsy, are now included among wearable electronics. Recently, however, the term wearable electronics has been used as a general term for any device used to detect biosignals and perform operations. Google Glass and Intel Mimo are typical examples of such devices. The range of applications of these devices is extremely wide because they target public health, that is, the health of all human beings. Expectations have been growing for wearable electronics that can collect human biosignals within a social setting of the declining birth rate and aging population. They are also of interest in the context of the 2020 Olympic Games to be held in Tokyo.

Our research group has been developing unobtrusive, flexible, lightweight, and thin electronic sensors. The goal of our study is to realize next-generation noninvasive bioinstrumentation systems that enable large-area and multipoint sensing using organic electronics and related systems including Si-LSI technology. The systems are thinner than human skin and can cover a wide surface area with complex shapes. In this chapter, here I will introduce fabrication methods and performance characteristics of ultrathin (∼1 μm), ultraflexible organic light-emitting diodes (LEDs), organic solar cells (optical sensors, photodetector), and organic transistors that are part of the former two devices [1–3]. In addition, I will discuss the future prospects

of unobtrusive biointerface electronics, which can be realized by integrating these devices.

Similarly to the interest in input devices such as sensors, the importance of output elements such as displays has been increasing. Along with the development of liquid crystal and plasma technologies, displays have been made thinner while they have been increased in size. Recently, a process technology to fabricate transistors at low temperatures has been established and fabrication of high-performance integrated circuits on plastic films has become possible. Thus, flexible electronics with mechanical flexibility have been attracting attention. In particular, new applications such as bendable and roll-up flexible displays, sensors, actuators, and solar cells, which were not realized using conventional silicon-based technology, are close to practical use.

Among flexible electronics, flexible displays are particularly in demand. For example, displays consisting of hard materials such as glass are easily broken and not portable even if they are lightweight and thin. To realize lightweight, thin, eye-friendly, and large-area displays, mechanical flexibility is required from the viewpoint of portability and reliability.

A display consists of a display unit and a driving unit. To realize flexible displays, both display units and driving units must be flexible. There are essentially two driving methods: a passive-matrix driving method that does not use transistors, and an active-matrix driving method that does. The structure of the driving units in the passive-matrix driving method is simpler and their fabrication is easier. However, the driving units in the active-matrix driving method are advantageous in terms of high definition, low power consumption, and small number of electrical wirings, and they are considered to be indispensable for large displays.

When displays are fabricated using plastic substrates, lightweight, thin, and highly impact-resistant displays are realized. For example, flexible displays are portable like plastic sheets, and users can use them as a tool to obtain information anywhere. As a case in point, the size of home TVs has been increasing. If the size increases further, it will be difficult to pass them through front doors or put them in an elevator. Flexible displays, even if they are large-area displays, can be rolled up, transported, and installed anywhere without difficulty. Motivated by these advantages, research on flexible displays toward their practical application has been actively carried out mainly by manufacturers.

With this as a background, the development of state-of-the-art flexible sensors and displays is presented in this review.

5.3 Ultrathin Organic LEDs

Organic LEDs were developed by Tang in Kodak (currently at the University of Rochester) [4]. Initially, a drive voltage of >10 V was required, and the brightness was relatively low ($\sim$1000 cd/m^2). Although the initial organic LEDs were far from ready for practical use, however, they demonstrated the excellent feasibility of the

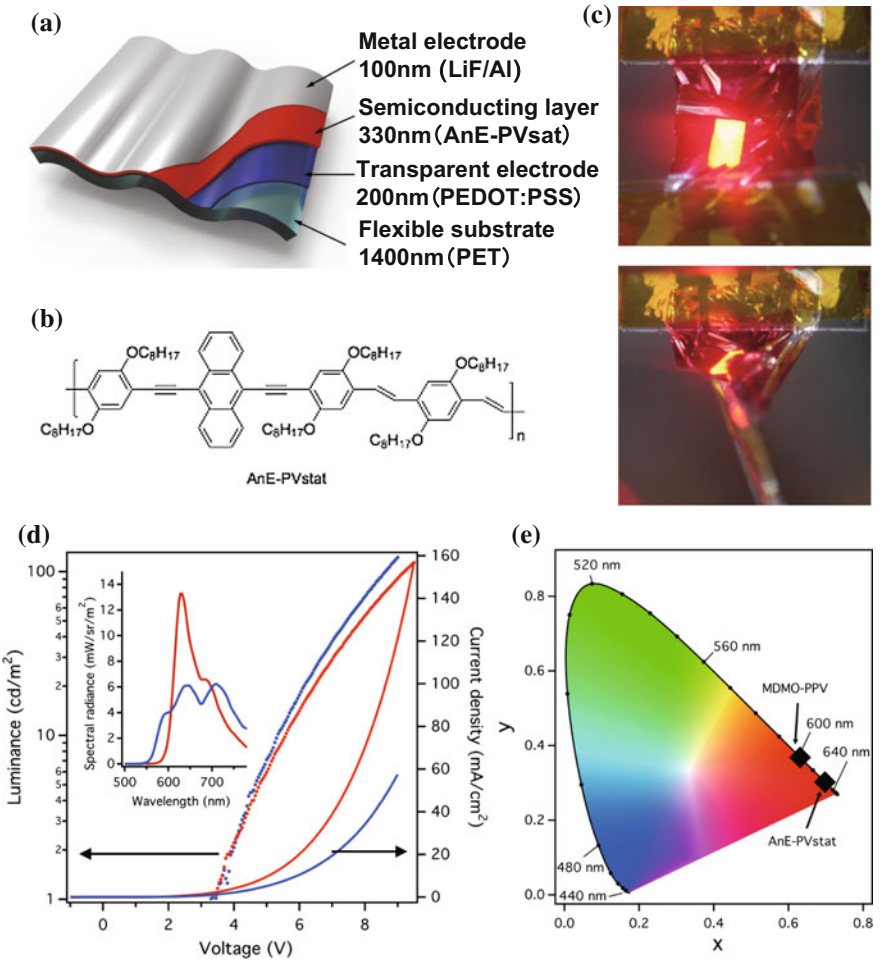

Fig. 5.1 Lightest (3 g/m^2) and thinnest (2 μm) flexible organic LED yet known. **a** Schematic of ultrathin organic LED showing composite layers and the thickness of each layer. **b** Molecular structure of polymer used for the active layer. **c** Photographs of a crumpled LED that maintains a luminance of 100 cd/m^2. **d** Relationships among applied voltage (*V*), luminance (*L*), and current density (*I*), i.e., *V*-*L*-*I* characteristic, for an LED with AnE-PVstat (*red*) and orange-emitting poly[2-methoxy-5(3,7-dimethyloctyloxy)]-1,4-phenylene-vinylene (MDMO-PPV) (*blue*) used as the active layer (*inset* relationship between emission wavelength and spectral radiance). **e** Chromaticity diagram of ultrathin organic LED. Adapted from [1]. Copyright 2013, Nature Publishing Group

organic LEDs. Along with the significant development of materials and structures, organic LED displays and organic LED illumination devices have been practically applied and are used in our daily lives. organic LEDs are advantageous in terms of power consumption, color reproducibility, and response speed. They are expected to be used not only for illumination devices and displays but also in medicine. As a

consequence, more lightweight and thinner organic LEDs have been demanded. Our research group has established an original fabrication technology that involves laminating organic semiconductor materials and electrode materials on commercially available 1.2 μm-thick ultrathin polymer films (polyethylene terephthalate (PET), polyethylene naphthalate (PEN)) at low temperatures and energy, and we have succeeded in fabricating the world's lightest and thinnest flexible organic LEDs [1]. Figure 5.1a shows a schematic of the ultrathin organic LED and its composite layers. The key to the development of the organic LED is the low-temperature process (Tprocess $<$ 150 °C) for fabricating organic LEDs, which are fabricated on 1 μm-thick polymer films with a relatively rough surface (root mean square (rms) roughness, 1 nm) without damaging the substrates. Concretely, a conductive polymer that can be formed into the substrates at low temperatures below $\leq$120 °C with low loss is used for the electrode (anode) instead of an indium-tin oxide (ITO) transparent electrode that requires high-energy processing. Red light emission (wavelength, 640 nm) was realized using anthracene-containing poly(p-phenylene-ethynylene)-alt-poly(p-phenylene-vinylene) (AnE-PVstat) (Fig. 5.1b) for the active layer. The organic LED is ultrathin; thus, it can accommodate strain and can operate electrically even when it is crumpled. The minimum bending radius of the organic LED was 10 μm and the luminance was 100 cd/m^2 when driven at 9 V (Fig. 5.1c). This luminance is equivalent to that necessary for indoor use. Although the luminance is not enough for the practical applications, we demonstrated the feasibility of ultraflexible organic LED manufactured on 1 mm-thick plastic substrates with very low-temperature process that can be applicable to various types of substrates including rubbers, papers, and bio-degradable materials. When the ultrathin organic LED film is pasted onto a flexible stretchable rubber, an LED array that can accommodate stretching of up to 100 % or more is successfully obtained and is expected to be applied to media such as displays and used as new light sources for medical purposes. The improvement of luminance and luminous efficiency is a future goal; it will be accomplished by improving the heat radiation mechanism during light emission and by using thin, high-heat-resistance substrates.

5.4 Ultrathin Organic Solar Cells (Optical Sensors or Photodetector)

With increasing interest in renewable energy, the importance of solar cells as a renewable clean energy source that can compensate for the insufficiency of power generated by conventional methods has been increasing. In addition, an ambient energy-harvesting technology for obtaining energy from the environment is particularly important considering a future in which various types of electronics, such as sensors, will be installed not only in living organisms but also everywhere around us. Large-area solar cells must be realized at low cost because electric power generation using solar cells is basically proportional to their area. Along with an increase in the

area of solar cells, both light weight and improved impact resistance (flexibility) are required. However, the solar cells currently available on the market are fabricated on glass substrates using silicon, resulting in a low impact resistance. Furthermore, when the glass substrate is thinned, the solar cells may break during fabrication or use, hampering the realization of lightweight solar cells. In contrast, solar cells made from organic semiconductors can be easily fabricated on polymer films by a liquid process such as printing and coating. Research on these solar cells has been vigorously carried out with the expected realization of large-area, low-cost, and lightweight solar cells. However, it was difficult to fabricate organic solar cells with a high power conversion efficiency equivalent to that of glass substrates on flexible thin polymer films by a liquid process; this issue must be resolved.

We succeeded in realizing the thinnest and lightest flexible organic solar cells yet achieved [2]. Figure 5.2a and b show a schematic of the composite layers and a photograph of the ultrathin organic solar cell, respectively. The ultrathin organic solar cells were fabricated on 1.2 μm thick polyethylene-naphthalate (PEN) or 1.4 μm thick polyethylene-telephthalate (PET) films. Even when bent to a bending radius of 35 μm, they were not mechanically broken and maintained a power conversion efficiency of 4.2 % (Fig. 5.2c and d). In fact, an ultrathin organic solar cell could be wound around a human hair (radius, approximately 10 m). The key technology in the development was the low-temperature film growth process, in which p-type semiconductor ink [poly(3-hexylthiophene-2,5-diyl) (P3HT)] and n-type semiconductor ink [[6,6]-phenyl-C61-butyric acid methyl ester (PCBM)] were mixed in an organic solvent and deposited onto a 1.4 m-thick PET film. Poly(3,4-ethylenedioxythiophene): poly(styrenesulfonate) (PEDOT:PSS), a conductive polymer that can be treated by a liquid process, was used as the transparent electrode. By placing the ultrathin solar cells on a prestretched rubber substrate, the solar cells could be stretched or compressed up to 300 %. Thus, organic solar cells with a power conversion efficiency of 4.2 % and steady output, even when bent to a bending radius of 35 μm or stretched or compressed up to 300 %, were successfully fabricated on polymer films. The electric power generation per gram of an ultrathin organic solar cell was equivalent to 10 W. The organic solar cells were lighter, thinner, and more flexible than any other commercial solar cells that generate this level of power (Fig. 5.2e). These solar cells can also be used as ultrathin organic optical sensors by applying reverse bias voltages (negative and positive voltages to p-type and n-type semiconductors, respectively), thereby realizing a new application as unobtrusive medical optical sensors.

5.5 Ultrathin Organic Thin Film Transistors (TFTs)

Organic TFTs used as flexible electronic switches are easily fabricated on polymer films by a liquid process such as printing. Therefore, research on organic TFTs has been active with the expected realization of large-area, low-cost, lightweight, and flexible organic TFTs. However, organic transistor integrated circuits with a high electric performance equivalent to that of circuits on glass substrates may not be

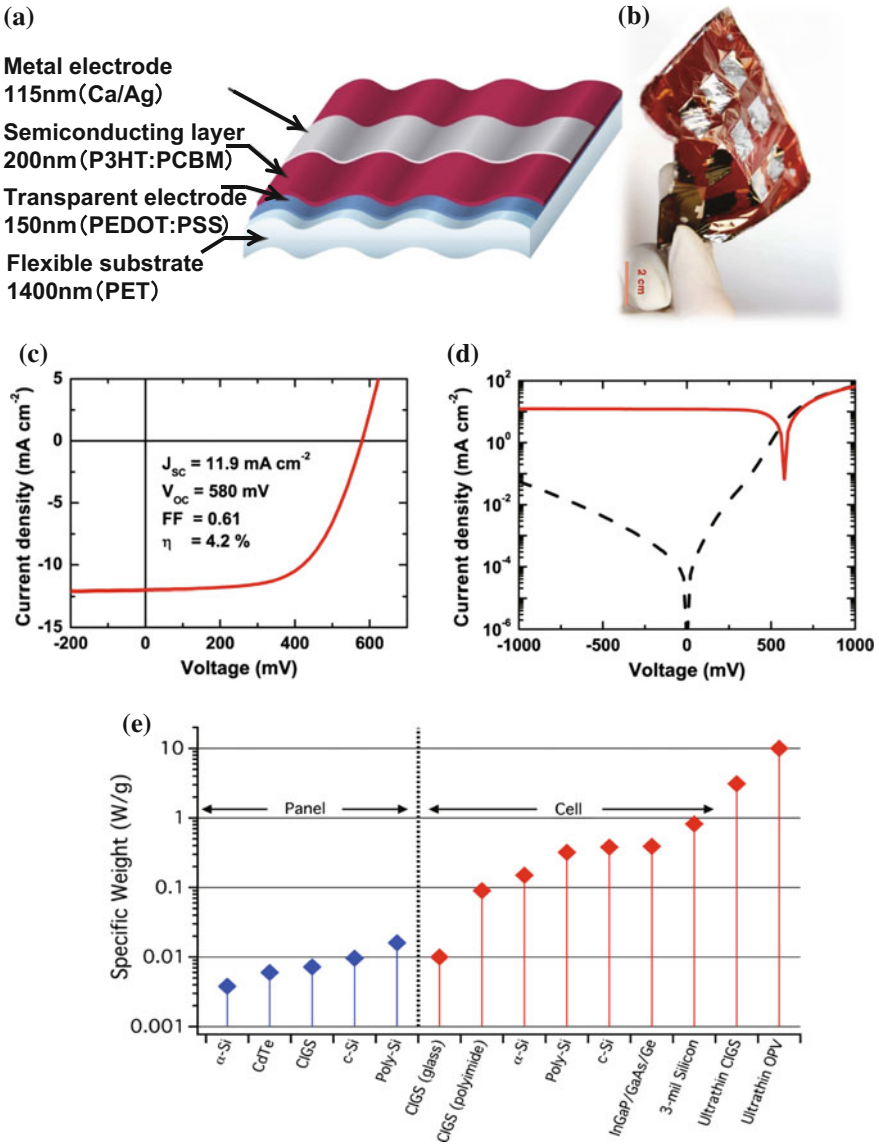

Fig. 5.2 Organic solar cell (optical sensor) fabricated on thin film. **a** Schematic showing composite layers and thickness of each layer. **b** Photograph. **c** Current-voltage (I-V) characteristic. **d** Dark current (*dashed line*) and photovoltaic current (*red solid line*). **e** Amounts of electric power per gram (W/g) generated by different solar cells with various semiconductor materials. The *bar* at the *rightmost* labeled "Ultrathin OPV" shows the results for our organic solar cell. Adapted from [2]. Copyright 2012, Nature Publishing Group

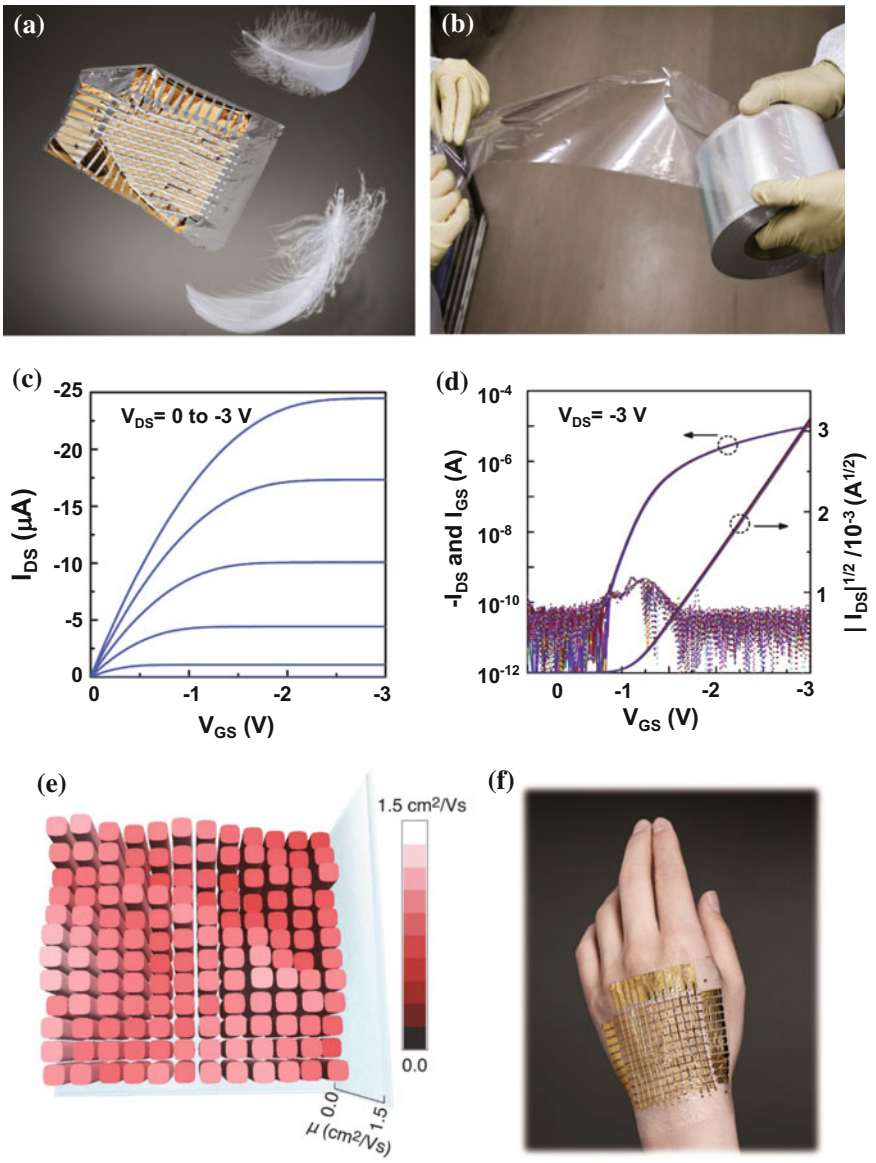

Fig. 5.3 Ultralightweight (lighter than a feather) and ultrathin organic transistor integrated circuit. Photographs of **a** an ultrathin organic transistor integrated circuit and **b** a 1 μm-thick PEN film used as a substrate. **c** Output and **d** transmission characteristics of TFTs. **e** Mobility mapping of 144 transistors fabricated on a substrate film; high-uniformity mobility is realized. **f** Photograph of an ultrathin transistor integrated circuit attached to the back of a human hand. The circuit can follow the complex shape of the hand surface. Adapted from [3]. Copyright 2013, Nature Publishing Group

fabricated on flexible ultrathin polymer films, particularly those with thicknesses of $\leq$10 μm; this issue must also be resolved. Our group has successfully developed ultrathin organic thin-film transistors and the circuits with 2 V operation (Fig. 5.3). A substrate we used was 1 μm-thick polymeric flexible films, so that it could be mechanically bend down to 5 μm in bending radius without any changes in electrical and mechanical performances.

Next, the development of various flexible transistors fabricated on plastic substrates is discussed.

Semiconductor materials, such as polysilicon, metal oxides, carbon nanotubes, amorphous silicon, and organic semiconductors, are used for transistors fabricated on plastic substrates in accordance with their characteristics. Table 5.1 is a summary of the electrical characteristics (mobility and operation (drive) voltage) and mechanical characteristics (critical bending radius) of flexible transistors fabricated on plastic films. These typical flexible semiconductors are used as the material for channel layers of transistors and various applications utilizing the characteristics of each material have been proposed. The details are explained below.

Polysilicon transistors are used as semiconductor materials with a high mobility. However, a process temperature of $\geq$500 °C is required, and it is difficult to directly fabricate the polysilicon transistors on plastic films. To address this problem, a method to fabricate high-performance polysilicon transistors on plastic films by transferring is used [5, 6]. For example, Kodaira et al. of Seiko Epson Corp. succeeded in fabricating a high-performance polysilicon transistor on a plastic film by the following method: a TFT backplane was first fabricated on a glass substrate and then transferred to a plastic film by employing the surface-free technology by laser annealing/ablation (SUFTLA) process [5]. Rogers et al. of the University of Illinois fabricated foldable multiplexed sensors by transferring dense silicon nanomembrane transistor circuits onto flexible substrates by the original transferring method using a polydimethylsiloxane (PDMS) stamp (Soft lithography). Utilizing the mechanical characteristics of the transistor, they monitored biopotentials by attaching the sensors to living tissues [6].

Hosono et al. of Tokyo Institute of Technology developed a technology to fabricate transparent metal oxide transistors (In-Ga-Zn-O) on plastic films by a low-temperature process and led the way to the development of high-performance flexible transistors with Hall effect mobilities exceeding 10 cm^2/Vs. Along with advancements in process technology, the electrical reliability of the flexible transistors is extremely high today. Metal oxide transistors have been applied practically as the driving elements of next-generation displays that will replace amorphous silicon transistors (mobility $<$ 1 cm^2/Vs), as well as in various fields including flexible displays [7, 8].

Carbon nanotubes are promising nanomaterials with excellent electrical and mechanical characteristics. There are many reports on transistors using carbon nanotubes as the semiconductor layer both in Japan and overseas [9–11]. Among them, Rogers et al. reported the results of folding experiments [6]. Such transistors have been reported to exhibit an excellent electrical characteristic (mobility exceeding 10 cm^2/Vs) and a mechanical characteristic (minimum bending radius of $\sim$10 mm) [7].

Table 5.1 Representative electrical and mechanical characteristics of various transistors fabricated on plastic films. Polysilicon TFTs/metal oxide TFTs/amorphous silicon TFTs/organic TFTs/vertical organic TFTs/mobility/operation (drive) voltage/critical bending radius

	Polysilicon TFTs [5]	Metal-oxide TFTs [7, 8]	CNT TFTs [9–11]	Amorphous silicon TFTs [12–14]	Organic TFTs [15, 16]	Organic TFTs [17]	Verticaltype organic TFTs [18]
Mobility (cm^2/Vs)	>10	7	>10	0.5	0.5	0.1	0.5
Operation voltage (V)	4	10	5	15	40	2.5	2
Critical bending radius (mm)	10	30	10	0.5	0.5	2.5	0.1

The technology to separate metal and semiconductor carbon nanotubes has been a challenge and rapidly advancing; however, the ON/OFF ratio that is sufficient for the minute channel length used in displays has not yet been obtained, requiring further research to improve reliability.

Although the mobility of organic transistors and amorphous silicon transistors fabricated on plastic films is only $\sim$1 cm^2/Vs, their minimum bending radius is 0.5 mm, which is an excellent mechanical characteristic [12–17]. Watanabe and Kudo of Chiba University succeeded in fabricating high-performance vertical structure transistors using the thin film interface as the channel layer, instead of the conventional organic transistor lateral structure, and reported that the variation in the electrical characteristics was negligible with respect to bending strain [18].

In reviewing previous pioneering work in terms of electrical and mechanical characteristics of transistors, the electrical characteristics of transistors obtained using inorganic semiconductors as the channel layer have been shown to be extremely high; however, the minimum bending radius was only $\sim$10 mm. In contrast, for organic transistors using flexible organic semiconductors as the channel layer, the minimum bending radius reached 0.5 mm but the mobility was $\leq$ 1 cm^2/Vs (Table 5.1). To improve the mechanical characteristics, the Young's modulus and thickness of the substrate film and the transistor sealing layer were made equal and the channel layer was placed at the neutral strain position (Fig. 5.4). By adopting this structure, a minimum bending radius of $\leq$1 mm was achieved. In addition, ultraflexible amorphous silicon transistors were reported to operate even after being folded $\geq$ 100,000 times [14]. This means that the transistors do not easily break even when crumpled like paper, folded, dropped, or stomped on, demonstrating the new possibilities of organic electronics.

The insulating characteristics of flexible gate insulating films, such as polymer insulating films, are not high compared with those of silicon oxide films. Therefore, obtaining thin flexible gate insulating films while maintaining the conventional yield is difficult. As a result, the thickness of gate insulating films of organic transistors fabricated on flexible substrates is 200–300 nm and a drive voltage of $\geq$10 V is required.

Klauk et al. of the Max Planck Institute for Solid State Research succeeded in driving organic transistors at 2 V using a self-assembled monolayer (SAM) gate insulating film one-molecule in length [19]. By applying this technology, in 2010 our research group succeeded in fabricating ultrathin organic transistor sheets driven at 2 V and organic complementary metal oxide semiconductor (CMOS) integrated circuits, whose electrical characteristics do not change even when crumpled [20] (Fig. 5.4). In more concrete terms, organic transistors with a high mobility were realized and even driven at 2 V by our original process (polyimide self-planarization layer technology) to smooth the surface of very thin plastic films (12.5 μm) at the atomic level. After the planarization process, the surface becomes atomically smooth, whose RMS value is less than 0.2 nm. In addition, by adopting the neutral strain structure of organic polymers that did not damage organic semiconductors, integrated circuits that could operate without any characteristic change, even when folded to a radius of curvature of 0.1 mm, were fabricated. Using the technology, the

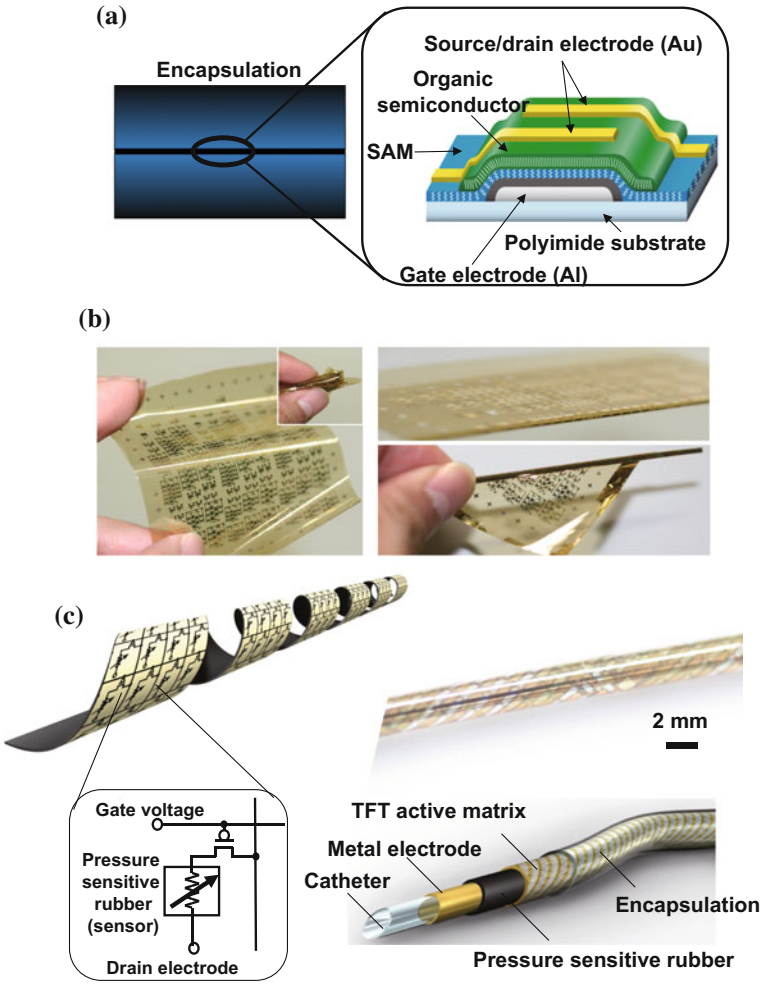

Fig. 5.4 **a** Schematic of cross section of flexible organic transistor. Ultraflexibility is realized by placing the transistor at the neutral strain position. **b** Photographs of flexible organic transistor circuit and circuit wrapped around a cylinder. No change in characteristics was observed even when the circuit was bent to a radius of 0.05 mm. **c** Medical catheter wrapped with a sheet of ultraflexible organic transistor circuits and a pressure sensor array. Adapted from [10]. Copyright 2010, Nature Publishing Group

transistor active matrix and pressure sensitive conductive rubber were integrated and wrapped spirally around a 1 mm-diameter medical catheter to realize a catheter with electronic circuits on its surface. The catheter can be used to measure the pressure distribution inside blood vessels [20] (Fig. 5.4).

We further developed the lightest (3 g/m^2, which is much lighter than a feather) and thinnest (2.4 μm) organic TFT active matrix known, and also fabricated its integrated circuit (Fig. 5.3a) [3]. All the components constituting the system weredirectly deposited one-by-one onto a 1.2 μm-thick PEN film (Fig. 5.3b). The minimum bending radius was 5 μm, and the TFTs did not break even when crumpled like paper or dropped from heights exceeding 1 m. The mobility was 3 cm^2/Vs at a drain-to-source voltage (VDS) of 3 V, demonstrating highly uniform electrical characteristics (Fig. 5.3c–e). The key to developing these organic TFTs was the fabrication of a 19 nm-thick ultrathin insulating film on a polymer film with a surface roughness of ~1 μm uniformly and with good adhesion. We established an original room-temperature process based on anodic oxidation to form highly homogenous aluminum oxide films with good adhesion to the substrate. In the conventional plasma oxidation method, the ultrathin polymer films under the aluminum oxide film were damaged by the plasma, leading to the generation of pinholes. By the anodic oxidation method adopted in our study, the conventional problems were solved without any high-energy processes, such as plasma processing.

The organic transistor integrated circuits were found to be extremely durable despite their world's-smallest thickness. More specifically, the thinnest films could withstand bending to a minimum radius of curvature of 5 μm and did not break when crumpled like paper and dropped from heights exceeding 1 m. In addition, no significant deterioration in electrical characteristics was observed after immersion in a physiological saline solution (with the same components as those of body fluid and sweat) for at least two weeks. Furthermore, stretchable integrated circuits with no deterioration in electrical or mechanical characteristics when they were compressed or stretched up to 233 % were realized. This type of flexible sensing system can be attached to curved surfaces to measure changes in pressure and temperature.

5.6 Development of Flexible Displays

Electrophoretic elements, organic LEDs, liquid crystal elements, and eletrochromic elements are known as the display elements in flexible displays. Flexible displays can be realized by controlling these elements using thin film transistor driving circuits fabricated on plastic films. Thus far, many flexible displays and electronic paper with excellent properties in terms of definition and luminance have been reported [21–56]. For example, a research group at Ricoh Co., Ltd., reported a 200 ppi all-printed organic TFT backplane for high-definition displays [33]. Dai Nippon Printing Co., Ltd., realized color flexible organic LED displays [34], and Toppan Printing Co., Ltd., realized large-area high-definition flexible electrophoretic displays [34, 38]. Next, state-of-the-art research and development on flexible displays is discussed on the basis of the kind of flexible display element.

Electrophoretic display elements are rewritable elements that work by controlling the position of colored floating particles by applying an electric field. Research on electrophoretic elements as the display units of flexible displays has been vigorously carried out. In particular, microcapsule electrophoretic elements have been practically used in digital signage represented by E-ink electronic paper [38]. In 2007, LG. Philips LCD in collaboration with US E-ink Corporation developed a 4,096-color, 14.1 in. flexible electronic paper [39].

Sakurai et al. of Bridgestone Corp. reported quick-response liquid powder displays (QR-LPD), namely, electrophoretic-based electronic paper displays (EPD) driven by a passive matrix using their original liquid powders as a charged toner [40]. In 2011, Yokoo et al. of Bridgestone Corp. reported the deployment of a thin and flexible smart card with an EPD using the QR-LPD technology [41]. With this technology, no power is consumed while images are stored, resulting in extremely low power consumption. They combined a flexible EPD with a wireless energy and data transfer system and demonstrated that an extremely thin, lightweight, and flexible smart card could be realized. In 2011, Akamatsu et al. of Sony Corp. reported a 13.3 in. active matrix flexible color electrophoretic display driven by low-temperature-processable amorphous silicon TFTs [42].

Organic LED displays have been commercially manufactured as high-definition, large-area flat panel displays because they are light-emitting displays, have a wide angle of view, and consume extremely low power. In 2001, Dai Nippon Printing Co., Ltd., in cooperation with Kido et al. of Yamagata University, reported color flexible organic LED displays and demonstrated the usefulness of applying organic LEDs to flexible displays for the first time in the world [34]. In 2006, a research group led by Kudo of Chiba University in cooperation with Pioneer Corp. succeeded in improving the performance of organic light emitting transistors by adding the LED's light emitting function to organic transistors. When organic light emitting transistors are used, the number of components in a product can be reduced, compared with the case of using conventional organic LEDs. Using this technology, they succeeded in fabricating a 16 $\times$ 16 dot active matrix panel on glass and film substrates [43]. In 2007, LG. Philips LCD developed a 4 in., full-color, flexible active matrix organic LED display using amorphous silicon transistor technology for the first time [44]. They have quarter video graphics array (QVGA) resolution, i.e., 320 $\times$ 240 pixels. In 2010, a research group led by Tokito of Japan Broadcasting Corporation (currently at Yamagata University) and Fujikake (currently at Tohoku University) reported active matrix full-color organic LED displays driven by organic TFTs with a resolution of 80 ppi [45]. In 2011, Nakata et al. of Japan Broadcasting Corporation fabricated transparent metal oxide semiconductor InGaZnO4 (IGZO) with polymer gate insulators on plastic films at a process temperature of $\leq$130 °C and developed 5 in. QVGA organic LED displays [46]. Also in 2011, Hatano et al. of Semiconductor Energy Laboratory Co., Ltd., (currently at Tokyo Tech.) reported a 3.4 in., full-color, active matrix organic LED display using IGZO and their original transfer technology [47]. Using transfer technology, high-performance devices can be easily fabricated on large-area films at a low cost. In 2012, Sharp Corporation succeeded in improving the reliability of displays while reducing light irradiation bias temperature (BT)

stresses and maintaining high mobility by using the C-axis aligned crystal structure of IGZO. Using this crystal structure, they succeeded in developing a 3.4 in., flexible organic electroluminescence (EL) display (326 dpi) compatible with a resolution of 540 × 960 pixels [48].

Electrochromic technology has been attracting attention as an opportunity to apply electrochemical characteristics to optics in products such as windows of advanced airplanes. As new flexible display elements using the electrochromic technology, Yashiro et al. of Ricoh Co., Ltd., reported full-color electrochromic displays (ECDs) based on the subtractive color mixing model in 2011. This improves the brightness and color reproducibility of displays. They succeeded in demonstrating a 3.5 in., active matrix full-color reflective ECD (resolution, 113.6 ppi; gray levLED, 64; duty, 50 %) [49].

Liquid crystal technology is the most critical technology for display elements to support the current display industry. In 2002, a research group of Toshiba Corporation developed a large-area (8.4 in.) and high-definition active matrix flexible liquid crystal display with super video graphics array (SVGA) resolution that can also be used in laptops [50]. The thickness of the glass substrate on which polysilicon transistors are formed at a low process temperature was reduced. The glass substrate was then pasted on a flexible substrate. A research group of Samsung Electronics Co., Ltd., announced that it will use flexible displays for smartphones in 2015. Liquid crystal technology is still an important technology also for flexible displays.

A research group led by Takeya of Osaka University (currently at the University of Tokyo) and Takimiya of Hiroshima University (currently at RIKEN) developed a flexible active matrix liquid crystal display with the highest-performance organic transistor drive circuits yet known. An organic semiconductor (alkylated dinaphtho-thienothiophene) was coated on the substrate and crystalized. By adopting this method, the mobility of their organic transistors (10 $cm^2/V{\cdot}s$) was one or more orders of magnitude higher than that of the conventional organic transistors used to drive displays, thereby attracting attention as a flexible display technology that realized high-speed operation and high resolution [51].

Focusing on the mechanical flexibility of displays, Nomoto et al. of Sony Corporation succeeded in fabricating a 2.5 in. active matrix LED full-color display driven by organic transistors (pixels, 160 × RGB × 120) in 2009 [52]. In 2010, a 4.1 in. 121 ppi organic TFT-driven full color organic LED display was fabricated on very thin films (thickness, 80 μm), which could be wrapped around a pencil; this achievement surprised many people. They had full-wide quarter video graphic array (FWQVGA) resolution. As the transistor active matrix drive circuit, an organic semiconductor material (a peri-xanthenoxanthene (PXX) derivative) was used. Use of flexible gate-driver circuits enabled video replaying even when the circuits were wrapped repeatedly around a cylinder with a 4 mm radius [37, 53]. Yoneya et al. of Sony Corporation reported the development of a 13.3 in. ultraextended graphic array (UXGA) flexible electrophoretic display using a soluble organic semiconductor (PXX derivative) with a mobility of 0.5 $cm^2/V{\cdot}s$. The display was reported to function without any characteristic change when bent to a radius of 5 mm [54].

In recent years, major developments have been made in flexible glass. Thin glass with a smooth surface and an extremely small coefficient of thermal expansion has been attracting attention as a promising material for substrates of flexible displays [55, 56]. Lo et al. of Industrial Technology Research Institute (ITRI) in Taiwan fabricated high-performance organic transistors on flexible glass and realized electrophoretic flexible displays [57].

5.7 Future Prospects

Device technologies (e.g., TFTs, LEDs, and photodiodes) for unobtrusive ultrathin and lightweight electronics have been developed. Thus, these electronics are expected to be increasingly applied in various fields including health care, medicine, and welfare. Along with the development of thinner and lighter sensing systems, sensors that cannot be perceived when worn can be used to obtain bioinformation unobtrusively. It is expected that bioinformation will be obtained over 24 h in a stress-free manner while the wearer leads a normal life. In addition, bioinformation (e.g., body temperature and heart rate) can be obtained anytime–for example, during exercise–by using highly impact-resistant sensors. When the systems are combined with the lightest solar cells, optical sensors, and organic LEDs, which are being developed concurrently, their application is expected to open new fields such as health care sensors for monitoring health conditions in a free-standing manner that are semipermanently powered by electricity derived from indoor and outdoor light.

Particularly high expectations are directed also to stretchable displays. Recently, the new technological field of stretchable electronics, which can be stretched and freely deformed into different shapes to a greater extent than flexible electronics, has attracted considerable attention [58–65]. For example, in the human living environment, in particular, surfaces that come into contact with humans (e.g., clothes, chairs, and beds) are mostly freely curved rather than flat planar or square, and stretchability is necessary for materials to cover them.

A key challenge in realizing stretchable electronics is to realize electrodes with both excellent electrical and mechanical characteristics. Highly conductive materials, such as metals and conductive polymers, are generally hard and not stretchable. In contrast, highly stretchable flexible materials such as rubber have poor electrical characteristics. Thus far, the development of stretchable electronics has been actively carried out worldwide by transferring highly conductive materials such as metals and graphene onto rubber sheets for use in stretchable interconnections, and by fabricating metal-evaporated films into a mesh structure to make them stretchable [54–61].

Rogers and Kim et al. realized electronic devices with integrated circuits, such as high-speed transistors, diodes, artificial eyes, and oscillators, on rubber sheets by soft lithography, where inorganic-material-based devices prefabricated on a hard silicon substrate by lithography were transferred onto stretchable substrates [59]. Wavy metal thin films were used for the interconnections, realizing a stretch ability of

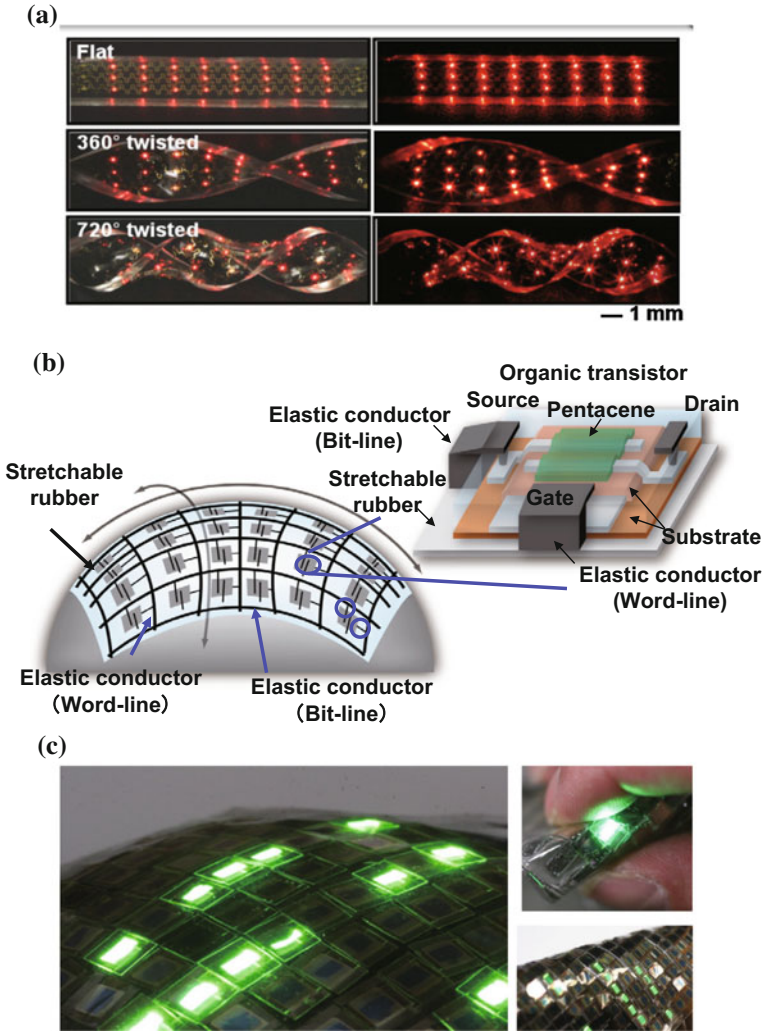

Fig. 5.5 **a** Stretchable inorganic LED array developed by Rogers et al. (Adapted from [65]. Copyright 2011, Nature Publishing Group.) Application as a medical light source is expected. **b** A rubber-like, stretchable transistor active matrix (stretchability, 70–80 %) realized by integrating organic transistors with elastic conductors. **c** Stretchable organic LED display (stretchability, 30–50 %). Adapted from [63]. Copyright 2009, Nature Publishing Group

~100 %. Using this technology, medical devices are being developed: for example, a waterproof inorganic LED has been transferred onto the surface of a catheter (Fig. 5.5) [65].

We have successfully developed elastic conductors that can be stretched like rubber, and we have fabricated stretchable large-area electronics using these new materials as electrodes (Fig. 5.5). Nanotube gels were uniformly dispersed in rub-

ber materials, realizing new elastic conductors with stretchability and conductivity exceeding 140 % and 100 S/cm, respectively [62–64]. We also succeeded in fabricating an organic transistor active matrix that can maintain its electrical characteristics, even when stretched by 70–80 %, by integrating the elastic conductors and organic transistor pixels on rubber sheets. Furthermore, stretchable active matrix organic LED displays were realized by integrating the elastic conductors with organic LED elements (Fig. 5.5) [62–64]. Conventionally, rubber and gels have not been applied to electrical integrated circuits because of their poor electrical characteristics. With the marked improvement of conductivity of elastic conductors that we achieved, it became possible to use conductors in interconnections for the first time. Although the resolution of the stretchable displays developed by us was not high, these displays can be folded and stretched by 30–50 % [62–64]. In the future, the degree of freedom in the design of electronic appliances will be markedly increased; for example, egg-shaped mobile phones may be realized. In addition, globe-shaped and human-body-shaped displays may be realized to provide users with various data in an easy-to-understand manner, such as meteorological information and the results of medical diagnoses. The wide angle of view by light emitted from organic LEDs and their low power consumption play important roles in stretchable active matrix organic LED displays. Therefore, these displays are considered to be the most promising type of stretchable displays, and their new applications are expected to greatly expand in the future.

References

1. M.S. White, M. Kaltenbrunner, E.D. Głowacki, K. Gutnichenko, G. Kettlgruber, I. Graz, S. Aazou, C. Ulbricht, D.A.M. Egbe, M.C. Miron, Z. Major, M.C. Scharber, T. Sekitani, T. Someya, S. Bauer, N. Sariciftci, Nat. Photon. **7**, 811 (2013)
2. M. Kaltenbrunner, M.S. White, E.D. Głowacki, T. Sekitani, T. Someya, N.S. Sariciftci, S. Bauer, Nat. Commun. **3**, 770 (2012)
3. M. Kaltenbrunner, T. Sekitani, J. Reeder, T. Yokota, K. Kuribara, T. Tokuhara, M. Drack, R. Schwodiauer, I. Graz, S. Bauer-Gogonea, S.I. Bauer, T. Someya. Nature **499**, 458 (2013)
4. C.W. Tang, S.A. VanSlyke, Appl. Phys. Lett. **51**, 913 (1987)
5. T. Kodaira, S. Hirabayashi, Y. Komatsu, M. Miyasaka, H. Kawai, S. Nebashi, S. Inoue, T. Shimoda, J. Soc. Inf. Displays **16**, 107 (2008)
6. J. Viventi, D.-H. Kim, L. Vigeland, E.S. Frechette, J.A. Blanco, Y.-S. Kim, A.E. Avrin, V.R. Tiruvadi, S.-W. Hwang, A.C. Vanleer, D.F. Wulsin, K. Davis, C.E. Gelber, L. Palmer, J. Van der Spiegel, J. Wu, J. Xiao, Y. Huang, D. Contreras, J.A. Rogers, B. Litt, Nat. Neurosci. **14**, 1599 (2011)
7. K. Nomura, H. Ohta, A. Takagi, T. Kamiya, M. Hirano, H. Hosono, Nature **432**, 488 (2004)
8. T. Kamiya, K. Nomura, H. Hosono, Adv. Mater. **11**, 044305 (2010)
9. T. Takenobu, N. Miura, S.-Y. Lu, H. Okimoto, T. Asano, M. Shiraishi, Y. Iwasa, Appl. Phys. Express **2**, 025005 (2009)
10. F. Nihey, H. Hongo, M. Yudasaka, S. Iijima, Jpn. J. Appl. Phys. **41**, L1049 (2002)
11. S.-H. Hur, O.O. Park, J.A. Rogers, Appl. Phys. Lett. **86**, 243502 (2005)
12. H. Gleskova, S. Wagner, Z. Suo, Appl. Phys. Lett. **75**, 3011 (1999)
13. H. Gleskova, S. Wagner, W. Soboyejo, Z. Suo, J. Appl. Phys. **92**, 6224 (2002)
14. L. Han, K. Song, P. Mandlik, S. Wagner, Appl. Phys. Lett. **96**, 042111 (2010)

15. T. Sekitani, Y. Kato, S. Iba, H. Shinaoka, T. Someya, T. Sakurai, S. Takagi, Appl. Phys. Lett. **86**, 073511 (2005)
16. T. Sekitani, S. Iba, Y. Kato, Y. Noguchi, T. Someya, T. Sakurai, Appl. Phys. Lett. **87**, 173502 (2005)
17. A. Jedaa, M. Halik, Appl. Phys. Lett. **95**, 103309 (2009)
18. Y. Watanabe, K. Kudo, Appl. Phys. Lett. **87**, 223505 (2005)
19. H. Klauk, U. Zschieschang, J. Pflaum, M. Halik, Nature **445**, 745 (2007)
20. T. Sekitani, U. Zschieschang, H. Klauk, T. Someya, Nat. Mater. **9**, 1015 (2010)
21. M. Noda, N. Kobayashi, M. Katsuhara, A. Yumoto, S. Ushikura, R. Yasuda, N. Hirai, G. Yukawa, I. Yagi, K. Nomoto, T. Urabe, J. Soc. Inf. Display (SID) **47**, 3 (2010)
22. S.R. Forrest, Nat. Mater. **428**, 911 (2004)
23. J.A. Rogers, Z. Bao, K. Baldwin, A. Dodabalapur, B. Crone, V.R. Raju, V. Kuck, H. Katz, K. Amundson, J. Ewing, P. Drzaic, Proc. Natl. Acad. Sci. USA **98**, 4835 (2001)
24. G.H. Gelinck, H. Edzer, A. Huitema, E. van Veenendaal, E. Cantatore, L. Schrijnemakers, J.B.P.H. van der Putten, T.C.T. Geuns, M. Beenhakkers, J.B. Giesbers, B-H. Huisman, E.J. Meijer, E.M. Benito, F.J. Touwslager, A.W. Marsman, B.J.E. van Rens, D.M. de Leeuw. Nat. Mater. **3**, 106 (2004)
25. B. Comiskey, J.D. Albert, H. Yoshizawa, J. Jacobson, Nature **394**, 253 (1998)
26. R. Sakurai, R. Hattori, M. Asakawa, T. Nakashima, I. Tanuma, A. Yokoo, N. Nihei, Y. Masuda. J. Soc. Inf. Display **16**, 155 (2008)
27. M. Suzuki, H. Fukagawa, Y. Nakajima, T. Tsuzuki, T. Takei, T. Yamamoto, S. Tokito, J. Soc. Inf. Display **17**, 1037 (2009)
28. S.M. Venugopal, D.R. Allee, J. Display Technol. **3**, 57 (2007)
29. H.E.A. Huitema, G.H. Gelinck, P.J.G. van Lieshout, E. van Veenendaal, F.J. Touwslager, J. Soc. Inf. Display **14**, 729 (2006)
30. S.E. Burns, K. Reynolds, W. Reeves, M. Banach, T. Brown, K. Chalmers, N. Cousins, M. Etchells, C. Hayton, K. Jacobs, A. Menon, S. Siddique, P. Too, C. Ramsdale, J. Watts, P. Cain, T. Von Werne, J. Mills, C. Curling, H. Sirringhaus, K. Amundson, M.D. McCreary, J. Soc. Inf. Display **13**, 583 (2005)
31. http://flexdisplay.asu.edu/
32. S.C. Jeng, K.H. Chang, J.M. Ding, L.P. Hsin, C.Y. Lin, Y.R. Lin, K.H. Liu, C.C. Lu, Y.A. Sha, H.L. Wang, C.C. Liao, J. Soc. Inf. Display **13**, 475 (2005)
33. K. Suzuki, K. Yutani, M. Nakashima, A. Onodera, S. Mizukami, M. Kato, T. Tano, H. Tomono, M. Yanagisawa, K. Kameyama, in Proceedings of IDW'09, vol, 1581 (2009)
34. http://www.dnp.co.jp/news/1188958_2482.html
35. http://www.toppan.co.jp/news/newsrelease1006.html
36. I. Yagi, N. Hirai, Y. Miyamoto, M. Noda, A. Imaoka, N. Yoneya, K. Nomoto, J. Kasahara, A. Yumoto, T. Urabe, J. Soc. Inf. Display **16**, 15 (2008)
37. M. Katsuhara, I. Yagi, A. Yumoto, M. Noda, N. Hirai, R. Yasuda, T. Moriwaki, S. Ushikura, A. Imaoka, T. Urabe, K. Nomoto, J. Soc. Inf. Display **18**, 399 (2010)
38. http://www.toppan.co.jp/products_service/denshi_paper/index.html
39. Technical digest. The Society for Information Display (SID) (2006)
40. R. Sakurai, S. Ohno, S. Kita, Y. Masuda, R. Hattori, Technical digest. The Society for Information Display (SID), vol. 68(2) (2006)
41. A. Yokoo, T. Kubota, Y. Saida, R. Sakurai, S. Ohno, Y. Masuda, R. Hattori, Technical digest. The Society for Information Display (SID), vol. 5(4) (2011)
42. K. Akamatsu, A. Nishiike, K. Masuda, Y. Kato, T. Maruyama, M. Suzuki, R. Yasuda, A. Yumoto, T. Kamei, T. Urabe, Technical digest. The Society for Information Display (SID), vol. 16(3) (2011)
43. http://pioneer.jp/press/2006/1114-1.html
44. http://news.mynavi.jp/news/2007/05/17/023/index.html
45. http://www.nhk.or.jp/strl/vision1/r5-3-1.htm
46. M. Nakata, H. Sato, Y. Nakajima, Y. Fujisaki, T. Takei, T. Shimizu, M. Suzuki, H. Fukagawa, G. Motomura, T. Yamamoto, H. Fujikake, Technical digest. The Society for Information Display (SID), vol. 16(4) (2011)

47. K. Hatano, A. Chida, T. Okano, N. Sugisawa, T. Nagata, T. Inoue, S. Seo, K. Suzuki, M. Aizawa, S. Yoshitomi, M. Hayakawa, H. Miyake, J. Koyama, S. Yamazaki, Y. Monma, S. Obana, S. Eguchi, H. Adachi, M. Katayama, K. Okazaki, M. Sakakura, Technical digest. The Society for Information Display (SID), vol. 36(4) (2011)
48. http://www.sharp.co.jp/corporate/news/120601-a.html
49. T. Yashiro, S. Hirano, Y. Naijoh, Y. Okada, K. Tsuji, M. Abe, A. Murakami, H. Takahashi, K. Fujimura, H. Kondoh, Technical digest. The Society for Information Display (SID), vol. 5(3) (2011)
50. http://www.toshiba.co.jp/tech/review/1999/02/f07/index_j.htm
51. http://www.nedo.go.jp/news/press/AA5_100087.html
52. http://www.sony.co.jp/SonyInfo/technology/technology/theme/organictransistor_01.html
53. http://www.sony.co.jp/SonyInfo/News/Press/201005/10-070/
54. N. Yoneya, H. Ono, Y. Ishii, K. Himori, N. Hirai, H. Abe, A. Yumoto, N. Kobayashi, K. Nomoto, T. Urabe, Technical digest. The Society for Information Display (SID), vol. 22(4) (2011)
55. http://www.corning.com/displaytechnologies/jp/products/flexible.aspx
56. http://www.agc.com/company/04.html
57. P. Y. Lo, J-M. Ding, J-P. Hu, Y-J. Chan, S. Garner, M. He, J. Lin, X. Li, M. Sorensen, J. Li, P. Cimo, C. Kuo, Technical digest. The Society for Information Display (SID), vol. 29(2) (2011)
58. T. Someya, Y. Kato, T. Sekitani, S. Iba, Y. Noguchi, Y. Murase, H. Kawaguchi, T. Sakurai, Proc. Natl. Acad. Sci. USA **102**, 12321 (2005)
59. D.H. Kim, J. Xiao, J. Song, Y. Huang, J.A. Rogers, Adv. Mater. **22**, 2108 (2010)
60. R.H. Kim, D.-H. Kim, J. Xiao, B.H. Kim, S.-I. Park, B. Panilaitis, R. Ghaffari, J. Yao, M. Li, Z. Liu, V. Malyarchuk, D.G. Kim, A.-P. Le, R.G. Nuzzo, D.L. Kaplan, F.G. Omenetto, Y. Huang, Z. Kang, J.A. Rogers, Nat. Mater. **9**, 929 (2010)
61. M. Kaltenbrunner, G. Kettlgruber, C. Siket, R. Schwodiauer, S. Bauer, Adv. Mater. **22**, 2065 (2010)
62. T. Sekitani, T. Someya, Adv. Mater. **22**, 2228 (2010)
63. T. Sekitani, Y. Noguchi, K. Hata, T. Fukushima, T. Aida, T. Someya, Science **321**, 1468 (2008)
64. T. Sekitani, H. Nakajima, H. Maeda, T. Fukushima, T. Aida, K. Hata, T. Someya, Nat. Mater. **8**, 494 (2009)
65. D.H. Kim, N. Lu, R. Ghaffari, Y.-S. Kim, S.P. Lee, L. Xu, J. Wu, R.-H. Kim, J. Song, Z. Liu, J. Viventi, B. de Graff, B. Elolampi, M. Mansour, M.J. Slepian, S. Hwang, J.D. Moss, S-M. Won, Y. Huang, B. Litt, J.A. Rogers. Nat. Mater. **10**, 316 (2011)

Index

M. Ohtsu and T. Yatsui (eds.), *Progress in Nanophotonics 4*,
Nano-Optics and Nanophotonics, DOI 10.1007/978-3-319-49013-7